Summer 8-2017

Anodic Nanocatalysts for Formic Acid Fuel Cells: An Electrochemical Study

Tamanna F. Shanta McFarland
University of Southern Mississippi

ANODIC NANOCATALYSTS FOR FORMIC ACID FUEL CELLS:

AN ELECTROCHEMICAL STUDY

by

Tamanna F. Shanta

A Dissertation
Submitted to the Graduate School,
the College of Science and Technology,
and the Department of Chemistry and Biochemistry
at The University of Southern Mississippi
in Partial Fulfillment of the Requirements
for the Degree of Doctor of Philosophy

August 2017

ANODIC NANOCATALYSTS FOR FORMIC ACID FUEL CELLS:

AN ELECTROCHEMICAL STUDY

by Tamanna F. Shanta

August 2017

Approved by:

_____

Dr. Wujian Miao, Committee Chair
Associate Professor, Chemistry and Biochemistry

_____

Dr. J. Paige Buchanan, Committee Member
Research Physical Scientist, U.S. Army Corps of Engineers

_____

Dr. Song Guo, Committee Member
Assistant Professor, Chemistry and Biochemistry

_____

Dr. Douglas S. Masterson, Committee Member
Associate Professor, Chemistry and Biochemistry

_____

Dr. Karl J. Wallace, Committee Member
Associate Professor, Chemistry and Biochemistry

_____

Dr. Sabine Heinhorst
Chair, Department of Chemistry and Biochemistry

_____

Dr. Karen S. Coats
Dean of the Graduate School

Published by the Graduate School

THE UNIVERSITY OF SOUTHERN MISSISSIPPI®

ABSTRACT

ANODIC NANOCATALYSTS FOR FORMIC ACID FUEL CELLS:

AN ELECTROCHEMICAL STUDY

by Tamanna F. Shanta

August 2017

Direct formic acid fuel cells (DFAFCs) have been reported as a prominent source of alternative green energy and solution to imminent energy crisis for the last two decades. The challenge to commercialize DFAFCs is primarily the utilization of cost effective, high performance and durable anodic catalyst for formic acid oxidation (FAO). Consequently, this dissertation addresses the extensive electrochemical study of a number of nanomaterials towards the potential use as electrocatalysts for FAO. Morphology and elemental analyses of the prepared nanomaterials were obtained using electron microscopy techniques.

After a general introduction and overall review of this dissertation (Chapter I), studies of the influence of chloride ions as contaminant on 20 wt% Pd/C were presented in Chapter II. The correlation between FAO peak current at glassy carbon electrode (GCE) coated with 20 wt% Pd/C (commercial), and the amount of chloride ions either added or leached from the frit of Ag/AgCl (3.0 M KCl) reference electrode were established. This study provides a guideline on how to choose a suitable reference electrode in fuel cell research.

Chapter III reports the comparative study of three different carbon-based support materials and the catalytic activities towards FAO using Pd-based mono and ternary composite nanocatalysts with commercial 20 wt% Pd/C (activated carbon). The

nanocatalysts were synthesized using Pd^{2+}, Ni^{2+} and Co^{2+} precursors on Vulcan XC-72, Ketjen Black EC600, and graphite nanoparticles support materials. Vulcan XC-72 supported catalysts showed the highest FAO activities, whereas Ketjen Black support showed the best performance in terms of long-term durability. All PdNiCo-ternary composites displayed superior catalytic efficiencies towards FAO.

In Chapter IV, polyhedral oligomeric silsesquioxane (POSS) molecules were utilized as template to prepare Bi nanorods and Pd nanoparticles. Specifically, Bi nanorods were studied to evaluate the so-called third-body effect mechanism of FAO.

Finally, in Chapter V, nine transition metal complexes, prepared using POSS ligand and procured, were blended individually with 20 wt% Pd/C and explored towards FAO activity and durability. These hybrid catalysts were then investigated and ranked in terms of catalytic activity and stability for FAO using electrochemical techniques. Potential composite nanomaterials were also evaluated and proposed for further study.

ACKNOWLEDGMENTS

I would like to express my earnest gratitude to my research advisor, Dr. Wujian Miao for allowing me to pursue my research interests throughout the graduate school tenure. I learned to be an independent researcher, grew personally and professionally over the last five years under his guidance. I want to acknowledge all past and present members of Miao research group especially, Dr. Yiliyasi Wusimanjiang who helped me to learn the electrochemical techniques during my first year.

My sincere appreciations to my committee members, Dr. Douglas S. Masterson, Dr. Karl J. Wallace, Dr. Song Guo and Dr. J. Paige Buchanan for always being encouraging, for all the constructive discussions and suggestions that helped me progress over the years.

I would like to acknowledge the partial financial support from the National Science Foundation (NSF Career award CHE-0955878), and The University of Southern Mississippi (USM).

I want to thank Mrs. Jessica Douglas, electron microscopy facility technician and the School of Polymers and High Performance Materials for the SEM, EDX, and TEM measurements to help me characterize the synthesized nanomaterials.

I would also want to show my utmost gratitude to the chair of the department, Dr. Sabine Heinhorst and Mrs. Tina Masterson, my teaching coordinator, for their mentorships, and continuous supports whenever I doubted myself.

I would not be writing this dissertation without the moral and financial supports from the Department of Chemistry and Biochemistry, USM. I want to acknowledge every

faculty, staff, and fellow graduate students of this department for the constant inspirations.

I want to recognize the opportunity I had, as the President of Graduate Student Senate, to meet and work with Dr. Karen S. Coats, Dean of the Graduate School and every member in her office, that made this journey at Southern Miss meaningful.

DEDICATION

I would like to dedicate this dissertation to my students from all over the world.

Finally, my humble indebtedness to my parents, friends, and Frederick Marshall McFarland.

TABLE OF CONTENTS

LIST OF TABLES

LIST OF ILLUSTRATIONS

LIST OF SCHEMES

LIST OF ABBREVIATIONS

FAO	Formic Acid Oxidation
PEMFCs	Polymer Electrolyte Membrane Fuel Cells
DFAFCs	Direct Formic Acid Fuel Cells
GCE	Glassy Carbon Electrode
CV	Cyclic Voltammetry, Cyclic Voltammogram
CA	Chronoamperometry
COSV	Carbon Monoxide Stripping Voltammetry
ECSA	Electrochemical Active Surface Area
RHE	Reversible Hydrogen Electrode
C	Activated Carbon
GNP	Graphite Nanoparticles
VXC	Vulcan XC-72
KBE	Ketjen Black EC600
NRs	Nanorods
NPs	Nanoparticles
POSS	Polyhedral Oligomeric Silsesquioxane
M-*acac*	Metal-Acetylacetonate
SEM	Scanning Electron Microscopy
EDX	Energy-dispersive X-ray Spectroscopy
TEM	Transmission Electron Microscopy

CHAPTER I - BACKGROUND AND TECHNIQUES

1.1 Fuel Cell

1.1.1 Fundamentals of Fuel Cells

A fuel cell is an electrochemical device in which a spontaneous redox reaction takes place in an electrochemical reactor that consumes a fuel (e.g., H_2, CH_3OH, C_2H_5OH, HCOOH, or other organic fuels) and an oxidant (oxygen/air) to generate electricity with efficiencies of up to 60%.[1] Unlike a battery, a fuel cell will continue to produce electricity if the fuel is supplied. Typically, in a chemical reaction between fuel and oxygen molecules, the fuel molecules are oxidized to provide electrons. At the subatomic scale, to harness electrons, the fuel and oxygen reactants are spatially separated by an electrolyte to complete the bonding reconfiguration. Thus, the electrons released from the fuel is forced to flow through an external circuit to constitute an electric current before they can recombine with the oxygen to complete the reaction.[1] Figure 1.1 shows a typical cross-sectional view of a fuel cell, where a number of steps are involved:

1. Fuel and oxidant transport: continuous supply with specific electrical, thermal, mechanical and corrosion requirements must be met.
2. Electrochemical reaction: fuel gets oxidized at the anode and oxidant (air/oxygen) is reduced at the anode.
3. Ion transfer: ions formed at the anode transfer through the electrolyte and react with the ions formed at the cathode.
4. Electron conduction: electrons produced at the anode flow through the outer circuit towards the cathode.

5. Product removal: products are removed continuously whereas exhaust fuel and excess oxidant are typically recycled.

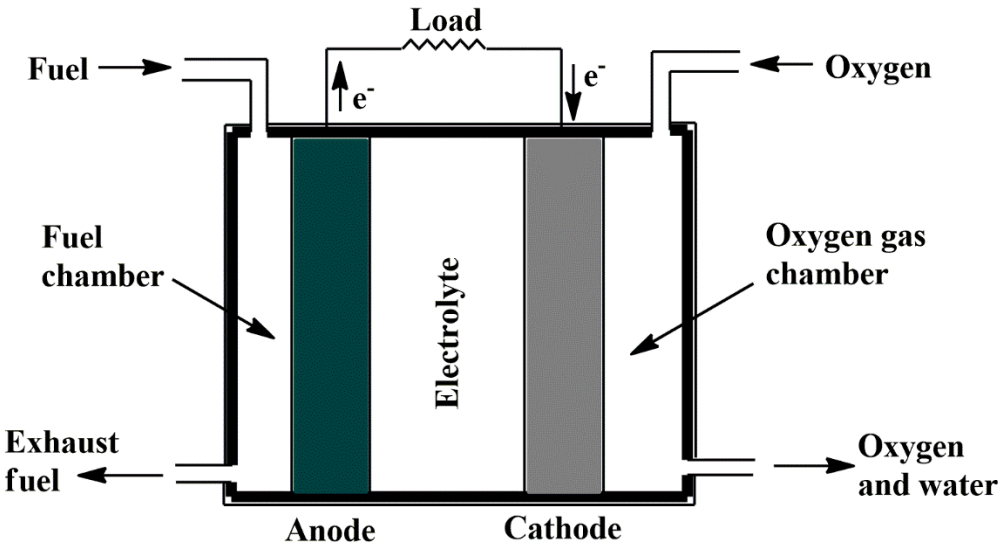

Figure 1.1 Typical cross-sectional view of a fuel cell.

The first H_2-O_2 fuel cell was invented by Sir William R. Grove in 1839 but mostly developed in the 20th and 21st centuries.[1] NASA's Gemini and Apollo space crafts both used H_2-O_2 fuel cell where the crews used water produced by the fuel cell for drinking and the heat to convert liquid hydrogen and oxygen to gaseous form. This application stimulated the New Generation of Vehicles program sponsored by the US government.[2,3] Compared with other power supplies, fuel cells possess several advantages, which include:

1. high energy efficiency than batteries and combustion engines,
2. substantially eco-friendly as NO_x, SO_x, and particulate emissions are almost zero,
3. sustainability as long as fuel is supplied,

4. portability and noiseless.

Fuel cells can be well-designed and mechanically suitable for small, portable electronics such as cell phone, laptop computers, remote sensors, as well as for automobiles and power plants, i.e., from 1-W to megawatt range. As world's consumption of energy increases exponentially due to population and economic growth, fuel cells could play an important role in mitigating the imminent energy crisis as they are promising source of green, sustainable, and highly efficient power supply.

Despite the abovementioned advantages, some issues remain to solve for fuel cells. Seeking highly efficient and cost effective catalyst materials, increasing fuel availability, optimizing temperature control, and extending the durability under start-stop cycling are some of the challenges of fuel cell studies.

1.1.2 Fuel Cell Types

Fuel cells are mainly classified based on the type of electrolytes used which controls the operating temperature, the type of fuel and the catalysts. The major types of fuel cells with their applications and challenges are listed in Table 1.1. In polymer electrolyte membrane fuel cells (PEMFCs), the organic fuel can be either oxidized at the electrode directly ("direct" fuel cell) or converted to H_2 gas first by a reformer ("indirect" fuel cell). Thus, direct fuel cells are generally portable with relatively simple cell configurations and short start-up time. Recently, PEMFCs have become the most feasible with direct liquid fuel-oxidant due to reduced volume and portability. Furthermore, fuel type and the choice of catalysts are critical for the overall uninterrupted power supply.

Table 1.1

Typical fuel cells and their features.

Fuel Cell	Operating Temperature	Applications	Challenges
Polymer Electrolyte Membrane (PEMFC)	<120 °C	Backup and portable power supply, distributed generation, transportation	Costly catalysts, sensitive to impurities
Alkaline (AFC)	<100 °C	Military, space, backup power, transportation	Sensitive to CO_2 and air, electrolyte management and conductivity
Phosphoric Acid (PAFC)	150-200 °C	Distributed generation	Expensive catalysts, long start-up time, sulfur sensitivity
Molten Carbonate (MCFC)	600-700 °C	Electric utility, distributed generation	Corrosion and breakdown of cell components, long start-up time, low power density
Solid Oxide (SOFC)	500-1000 °C	Auxiliary power, electric utility, distributed generation	High-temperature corrosion, long start-up time, limited number of shutdowns, breakdown of cell components

Note: Collected and modified from ref.[1,3]

1.2 Direct Formic Acid Fuel Cell (DFAFC)

When formic acid is used as fuel in direct fuel cells, the device is termed direct formic acid fuel cell (DFAFC). Among the traditional choices of polymer electrolyte membrane (PEM) based fuel cells (PEMFC), PEM-based DFAFC possesses several distinct advantages as compared with H_2-PEMFC and direct methanol fuel cell (DMFC).[4-7] First, formic acid is a non-toxic, non-flammable and non-explosive liquid resulting in easier handling and storage. Second, formic acid exhibits six times lower fuel crossover flux through Nafion® (sulfonated tetrafluoroethylene) than methanol and negligible cathode poisoning allowing the use of thinner membrane and higher concentrations of fuel (5 – 12 M), thus compensating the lower energy density of formic

acid (2104 Wh L^{-1}).[4] Third, formic acid is a good electrolyte leading to a lower contact resistance. Finally, DFAFC has faster oxidation kinetics than DMFC and a higher theoretical thermodynamic cell potential (1.48 V) than those of hydrogen (1.23 V) and direct methanol fuel cells (1.21 V).[5] Not surprisingly, formic acid has come forward as a promising fuel since the first report in 1996 by Weber *et al*.[8] Moreover, an ongoing effort on investigating formic acid as renewable and carbon neutral biofuel has been reported.[9]

1.2.1 Working Principle of DFAFC

Figure 1.2 shows a schematic diagram of a simple DFAFC setup, where formic acid is fed to the cell and catalytically oxidized to carbon dioxide and protons at the anode by losing two electrons, whereas oxidant (air/oxygen) is simultaneously reduced by gaining two electrons to water at the cathode in the presence of protons diffused from the anode via the PEM membrane. The electrons resulting from the formic acid oxidation (Equation 1.1) at the anode flow through the electrical circuit to the cathode, providing electrical power to the load.

The theoretical open circuit voltage (OCV) at 25 °C for the cell is determined using the following equations, where RHE refers to the reversible hydrogen electrode:[4,5,7]

At the anode: $HCOOH \rightarrow CO_2 + 2H^+ + 2e^-$ $E° = -0.25$ V vs. RHE (1.1)

At the cathode: $\frac{1}{2}O_2 + 2H^+ + 2e^- \rightarrow H_2O$ $E° = +1.23$ V vs. RHE (1.2)

Overall: $HCOOH + \frac{1}{2}O_2 \rightarrow CO_2 + H_2O$ $\Delta E° = +1.48$ V (1.3)

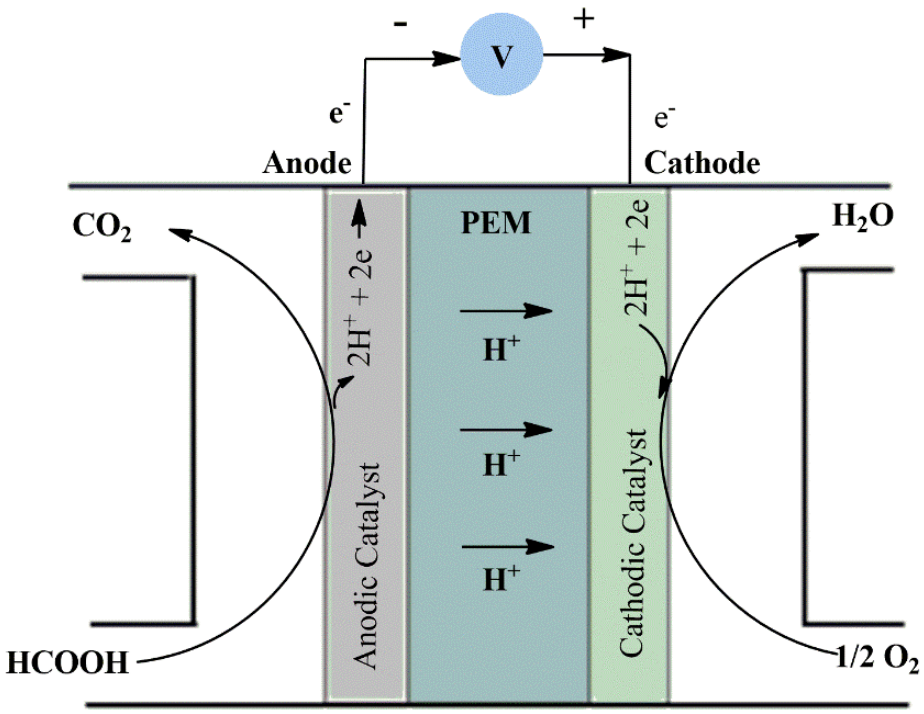

Figure 1.2 Schematic of working principle of DFAFC.

1.3 Formic Acid Oxidation (FAO)

1.3.1 Reaction Pathways

It is established already that the electrocatalytic oxidation of HCOOH to CO_2 (Equation 1.1) proceeds via a "dual pathway" mechanism characterized by the following equations,[4,5,7]

$HCOOH \rightarrow HCOOH^{*} \rightarrow CO_2 + 2H^{+} + 2e^{-}$ (dehydrogenation step) (1.1a)

$HCOOH \rightarrow CO_{ad} + H_2O \rightarrow CO_2 + 2H^{+} + 2e^{-}$ (dehydration step) (1.1b)

where direct oxidation of reactive weakly-adsorbed intermediates, $HCOOH^{*}$ to CO_2 through dehydrogenation (Equation 1.1a) occurs in parallel with the indirect dehydration pathway involving strongly-adsorbed carbon monoxide (CO_{ad}) (Equation 1.1b). One of the foremost problems is the hazardous CO_{ad} intermediate produced during the indirect

oxidation which is known to poison catalysts, especially Pt based catalysts thus requires a higher overpotential resulting in decrease in cell efficiency.

Among the catalytic enhancement mechanisms, the bifunctional and third-body mechanisms are utilized to facilitate FAO as shown in Figure 1.3. Typically, after forming the CO_{ad}, additional OH_{ad} is required to diffuse and combine to complete the dehydration pathway (Equations 1.1b, i – 1.1b, iii). If sufficient OH_{ad} is not available, the catalyst surface is blocked by CO_{ad}.

$$HCOOH + M(1)^0 \rightarrow M(1)\text{-}CO_{ad} + H_2O \quad (1.1b, i)$$

$$M(2)^0 + H_2O \rightarrow M(2)\text{-}OH_{ad} + H^+ + e^- \quad (1.1b, ii)$$

$$M(1)\text{-}CO_{ad} + M(2)\text{-}OH_{ad} \rightarrow M(1)^0 + M(2)^0 + CO_2 + H^+ + e^- \quad (1.1b, iii)$$

The addition of secondary or tertiary metal atoms to the catalyst atoms (Pt or Pd) facilitates the bifunctional mechanism that involves crucial OH_{ad} production step (Equation 1.1b, ii). Bifunctional mechanism also manifests by lowering the CO_{ad} and reducing overpotential (Figure 1.3A). Alternatively, alloying or using secondary inactive metal atoms could provide steric hindrance enhancing the preferential CH-down orientation (Figure 1.3 B), which is termed as third-body effect. These mechanisms also depend on catalyst surface coverage, roughness, and electronic effect of the alloying component.[10-12]

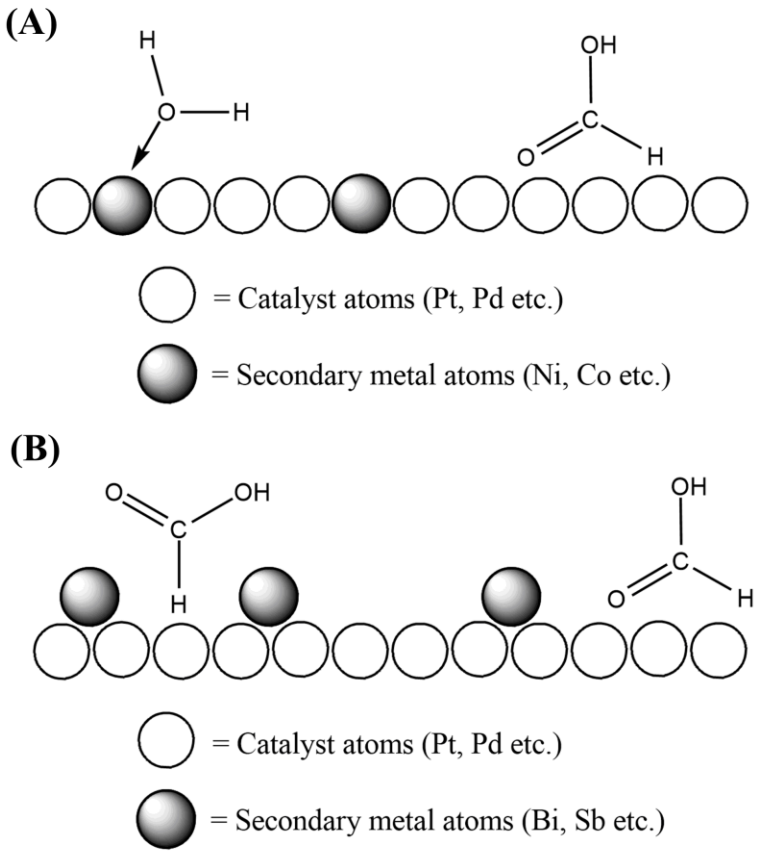

Figure 1.3 Formic acid electrooxidation mechanisms.

Note: Cartoon representation of (A) Bifunctional mechanism on bimetallic catalyst, (B) third-body effect, where the spheres resemble metal nanoparticles and are placed to show various FAO adsorption processes. (Modified and reproduced from ref.9)

1.3.2 Anodic Catalysts

The structure, morphology and physicochemical properties of an electrocatalyst could affect the performance of DFAFC and remain to be resolved further. Transition metals and their complexes have long been used in industry to catalyze syntheses of a wide variety of organic compounds.[13,14] They are distinguished from main group elements in having partly filled *d*-orbitals that can easily give and take electrons to form different oxidation states, which allow them to interact with the reactant to produce a lower energy intermediate. As shown in Equation 1.1b, CO adsorption could be an

important mechanistic step during the HCOOH electrooxidation, thus transition metal based catalysts could play a key role in enhancing the reaction kinetically that involves the adsorption, diffusion, and bond dissociation steps of CO as demonstrated in the literature.[14,15]

Other than Pt, several other metals or metal combinations have been employed as anode catalysts, which include Pd,[16-26] Pt-M_1 (M_1 = Bi,[10,11,27,28] Pd,[29-35] Pb,[36-38] Sn,[37] Au,[39-41] and Ru[33,42,43]) or Pd-M_2 (M_2 = Bi,[37] V,[37] Mo,[37] Ni,[44,45] Au,[46-51] Cu,[52,53] Co,[54,55] Sn,[53,56] Sb,[12] and Ir[57]) nanomaterials and their alloys. The addition of the second elements to Pt or Pd results in the increase in electrocatalytic activity for formic acid oxidation, lowering of the CO poisoning and the efficiencies could be significantly increased as well.[4,5,11,27,36-40,44,58-62] This is because the addition of the second element decreases the *d*-band gap of the primary transition metal (e.g., Pd or Pt) and weaken the adsorption of the reaction intermediates.[44,63] Besides, non-metal element, P alloyed with Pd,[64,65] and two Pd based ternary catalysts, i.e., Pd_4Co_2Ir[55] and PdCuSn,[53] have also been reported. These attempts, however, have not effectively solved the problem of the rapid decomposition of HCOOH over the catalyst (Equation 1.1b) which is associated with the CO poisoning.[66] The high cost of these catalysts is also a concern for the commercialization of the fuel cells.[4,5]

Furthermore, pure metal- or alloy-based catalysts under the fuel cell operation conditions cannot avoid the inevitable dissolution in HCOOH over the potential window of interest.[67,68] The development of advanced catalyst supporting material has been a promising way to improve the activity and stability of fuel cell electrocatalysts.[4] Carbon-based materials especially carbon black have been widely used due to their good

conductivity, chemical stability, and low cost. However, carbon black is essentially nonporous with a low surface area (<900 m^2/g), resulting in low utilization of expensive precious catalysts. Multi-walled carbon nanotubes (MWCNTs) (500 – 1000 m^2/g)[29,49-51,53,54,69-71] and graphene (2630 m^2/g),[40,72,73] on the other hand, have proved to be potential catalyst support materials for fuel cell applications, owing to their good conductivities, large surface areas, stable and durable mechanical and thermal properties. Since last decade, transition metal oxides based semiconducting materials, such as TiO_2,[71,74-76] SnO_2,[71,77] CeO_2,[58,78] SiO_2,[79] ZrO_2,[80] MnO_2,[72] Al_2O_3,[81] and WO_3,[82,83] have been reported to be effective supports. Nevertheless, as anodic catalyst supports in DFAFC, their chemical and electrochemical stabilities are questionable because these oxides could react with formic acid or could be reduced at the electrode.

Preparation of homogeneously unary or binary composite catalysts in a controllable fashion is another challenge. Many fuel cell catalysts reported in the literature were prepared via chemical reduction of a mixture solution containing metal ions or colloidal components in the presence of carbon black,[16,44,57,65,66,82] or using electro-deposition.[21,34,84-87] As revealed by microscopic characterizations, these catalysts are often made non-uniformly. Furthermore, addition of vanadium or palladium metal ions to the electrolyte solution has found to enhance the electrocatalytic performance of carbon supported Pd catalysts for oxidation of formic acid.[17,88]

1.4 Polyhedral Oligomeric Silsesquioxane (POSS)

Polyhedral oligomeric silsesquioxane (POSS) molecules are a class of unique hybrid organic-inorganic chemicals commercialized by Hybrid Plastics[89] located in Hattiesburg, MS. POSS has a chemical formula of $(RSiO_{1.5})_n$ which is between that of

silica (SiO_2) and silicone (R_2SiO). A typical fully condensed POSS molecule has an inorganic cage structure comprised of 8, 10, or 12 silicon atoms surrounded by a number of organic substituents (Figure 1.4).

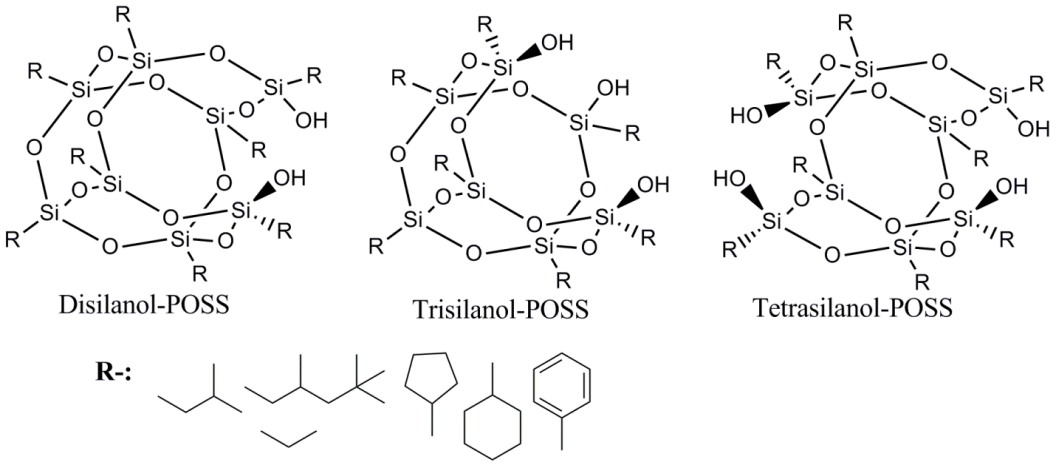

Figure 1.4 Chemical structures of POSS molecules.

The inorganic cage with a diameter of ~1.5 nm provides thermal and chemical stability while the organic substituents can be tailor-made to have desired functionalities. For example, POSS is very stable in both acid and base, and its solubility and reactivity can be readily tuned by changing the organic substituents. The nanoscopic and pore structure, high resistance to acidic media, as well as large surface area (3,600 m^2/g)[89] make POSS a promising candidate as catalyst support in DFAFCs. A variety of transition metal-POSS complexes (M-POSS) that could be potentially used as the catalyst for FAO. Di-, tri-, and tetra-silanols with different organic substituents (Figure 1.4) could be used as precursors for complexation with suitable transition metal salts using modified methods based on the previous literature reports.[3,90-113] The synthesized complexes should be easily coupled with Nafion® PEM membrane but completely insoluble in highly concentrated formic acid which can be achieved by choosing suitable R- groups of

di-, tri-, or tetra-silanol POSS molecules. Additionally, transition metal nanoparticles or nanotubes could be synthesized using POSS as frameworks and blended with M-POSS complexes to prepare composite nanocatalysts for DFAFCs.

Transition metal-POSS (M-POSS) based catalyst may offer several distinct advantages over the presently reported formic acid oxidation catalysts: (1) Low cost— catalysts containing non-precious transition metals either covalently bonded to POSS molecules stoichiometrically (e.g., in a molar ratio of 1:1) or reduced to form metal nanoparticles/nanotubes using POSS as a framework could significantly minimize the use of metals; (2) Fast kinetics and effective mass transfer— the porous POSS molecules could accelerate the diffusion rate or shorten the diffusion path of reactants and products of FAO so that the utilization of the active site of the catalyst could be improved, and the residual time of the intermediate CO_{ad}, hence the CO poisoning probability, could be reduced; (3) High stability— both POSS and M-POSS complexes are stable in acidic media, and they are expected to be stable electrochemically during the operation of DFAFCs; (4) High efficiency— POSS has a very large surface area of ~3,600 m^2/g[89] (vs 917-1374 m^2/g for nanoscale mesoporous silica[114] or 235 m^2/g for carbon black Vulcan XC-72[115]), which allows more active sites of the catalyst accessible to formic acid; (5) Low catalyst poisoning effect— the electronic property of the M-POSS complex is significantly different from that of the traditional metal catalysts as the POSS trisilanols are very acidic, with roughly the same electron withdrawing effect as a CF_3 group.[116,117] As a result, the FAO reaction pathway at POSS-based catalysts may favorably undergo via the dehydrogenation step (Equation 1.1a) due to the formation of H-bonding. Steric effects may also lower the probability of physical adsorption on POSS catalysts; (6)

Synergic effect— sulfonated POSS molecules have been recently used along with the conventional Nafion® membrane to improve the durability and proton exchange capability of PEM,[118,119] thus the use of M-POSS catalysts in the PEM-based fuel cell may be beneficial to the life and efficiency of the cell.

Previous studies have shown that M-POSS complexes could be effective catalysts for many types of chemical reactions in, e.g., the metathesis, polymerization, epoxidation, and Diels-Alder reactions of olefins.[90-94] Conversely, no report on the formic acid oxidation with these kinds of complexes has been found in the literature.

1.5 Rationale

The world's energy consumption rate is predicted to increase by more than 100% over the next 40 years as a result of population and economic growth.[120-122] To mitigate the global energy crisis in a sustainable fashion, the research and development of renewable, green, and sustainable energy supply, as well as the improvement of energy efficient new technologies such as fuel cells, are certainly needed.[3] Catalysts have and will play a vital role for the effective energy conversion. Driven by the necessity as shown in Scheme 1.1, the overall goal of this dissertation is to investigate highly efficient, chemically stable, self-supported, functionally flexible, and low-cost catalysts for DFAFCs.

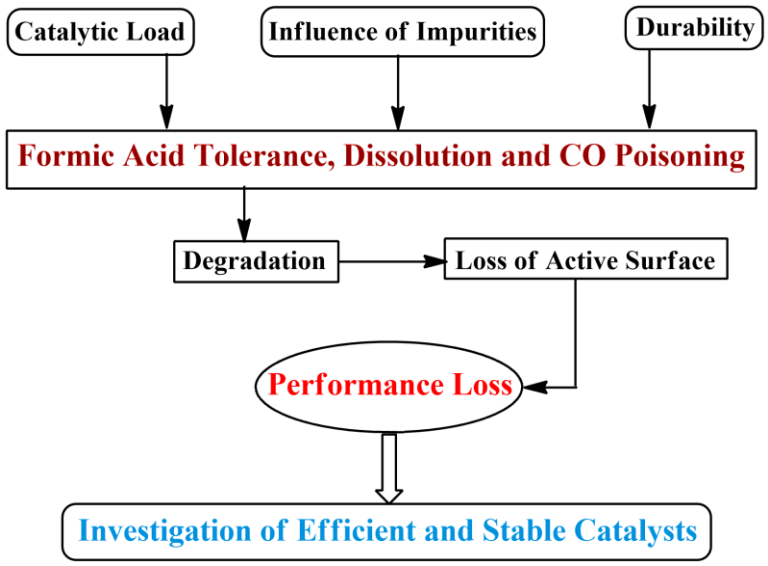

Scheme 1.1 Research problems and rationale.

1.6 Scopes and Methodology

Since it is widely apprehended that a transformative advance in catalyst technology is necessary to render PEM fuel cells competitive with other energy sources, the main objectives of the projects described in this dissertation are:

(1) To synthesize new nanometer-sized anodic catalysts consisting of transition and post-transition metals using, e.g., nanohybrid POSS frameworks;

(2) To characterize the morphology and elemental composition of the synthesized nanocatalysts;

(3) To study the catalytic activity and stability towards formic acid electrooxidation of the newly synthesized catalysts including metal complexes cheated to POSS using a variety of electrochemical techniques;

(4) To understand the effect of electrolyte composition, impurities, or interfering species on electrooxidation of formic acid; and

(5) To investigate the formic acid tolerance, electrochemical active surface area, and factors that could affect the efficiency and stability.

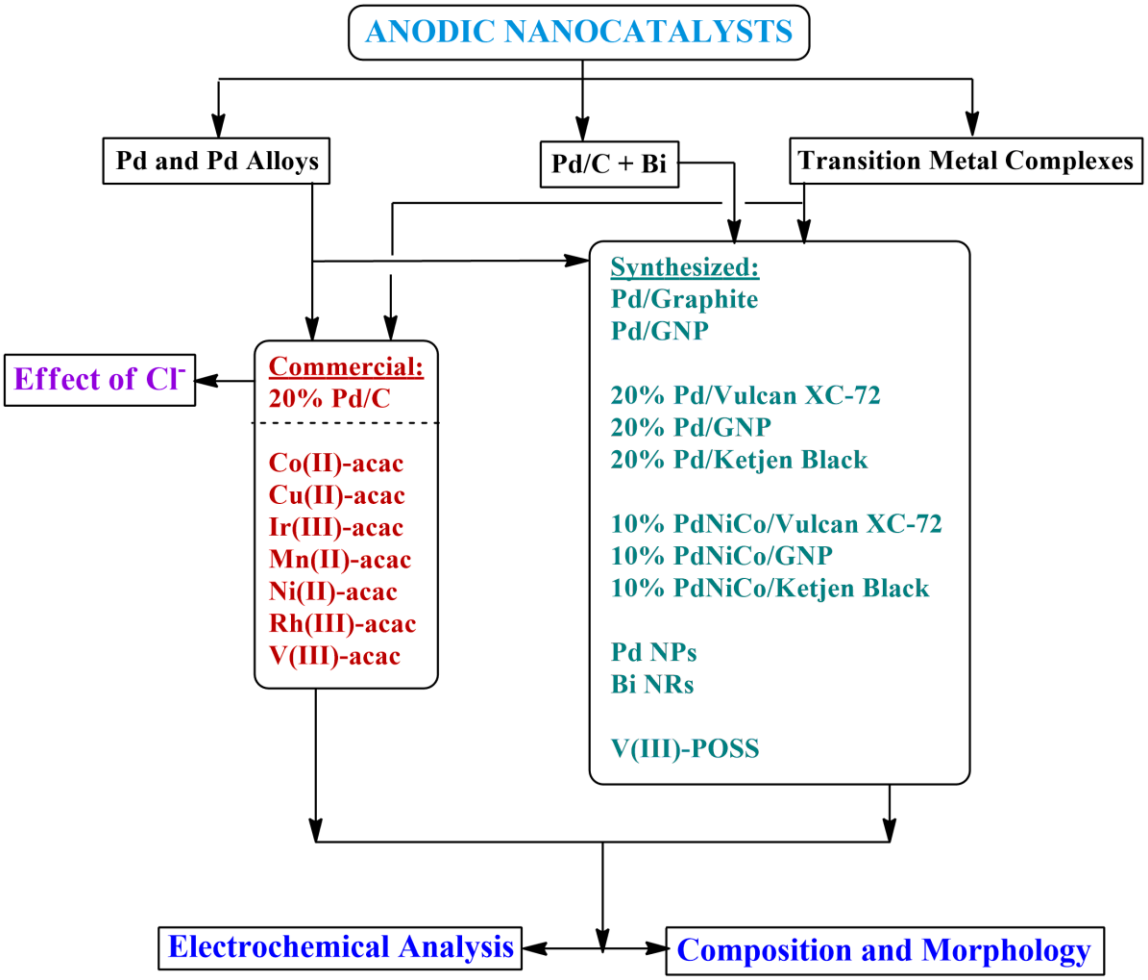

Scheme 1.2 Methodology of the projects.

Note: GNP: graphite nanoparticles, NP: nanoparticle, NR: nanorod, FA: formic acid, ECSA: electrochemical active surface area, CV: cyclic voltammetry, LSV: linear sweep voltammetry, CA: chronoamperometry, CO: carbon monoxide, SEM: scanning electron microscopy, EDX: energy-dispersive X-ray spectroscopy, TEM: transmission electron microscopy.

Methodology followed in the projects is summarized in Scheme 1.2, where three broad classes of electrocatalysts including commercially available activated carbon supported 20 wt% Pd catalyst and seven metal-acetylacetonate (M-acac) complexes will be investigated. The Pd-based mono and ternary composites are synthesized on three

different carbon supports and compared with the commercial Pd/C. Whereas, POSS based particles are prepared separately. Specifically, Bi nanorods are mixed with the commercial Pd/C to examine a different aspect of FAO mechanism. All the synthesized catalysts are analyzed utilizing microscopic techniques such as scanning electron microscope (SEM) and transmission electron microscope (TEM) for structural characterizations. For chemical composition and elemental mapping energy-dispersive X-ray spectroscopy (EDX) is used. The electrochemical analyses are carried out using drop casting methods with constant catalytic loads on the working electrode. Catalytic activities towards FAO are determined by cyclic voltammetry (CV) and linear sweep voltammetry (LSV). The durability and performance over time are measured with chronoamperometry (CA) and multi-potential CA techniques. Additionally, formic acid (FA) tolerance and electrochemical active surface area (ECSA) of the synthesized Pd-based catalysts are evaluated against the commercial Pd/C by CO-stripping voltammetry. Finally, purchased and synthesized metal complexes will be dispersed with the commercial Pd/C to explore the synergistic effects which could be further investigated.

1.7 Electrochemical Analyses

1.7.1 Cyclic Voltammetry (CV)

1.7.1.1 Fundamentals of CV

Cyclic voltammetry (CV) is a simple, flexible but sophisticated potential sweep method to obtain chemical, mechanistic, and kinetic information of the electroactive species. For a Nerstian reversible system, this technique was advanced by Randles and Sevčik[123] where peak current, i_p, is measured for applied potential without agitating the electrolyte. Thus, for diffusion controlled redox reaction, the peak current is given by:

$$i_p = 0.4463\ (F^3/RT)^{1/2}\ n^{3/2}\ AD_O^{1/2}C_O^{*}\upsilon^{1/2} \quad (1.4)$$

where F is the Faraday constant (96485.33 C/mol), n is the number of electrons involved in the electrochemical reaction, A is the area of the working electrode (cm^2), D_O is the diffusion coefficient of oxidant O (cm^2/s), with concentration C_O^* (mol/cm^3), and υ is the scan rate (V/s). At 298 K, the redox peak separation potential, ΔE_p, can be estimated by Equation 1.5:

$$\Delta E_p = E_{pa} - E_{pc} = 57/n\ \text{mV} \quad (1.5)$$

where E_{pa} and E_{pc} are anodic peak potential and cathodic peak potential, respectively.[1,123-125] Figure 1.5 shows a typical cyclic voltammogram of the one electron-transfer reversible process of $[Fe(CN)_6]^{3-}$ at a glassy carbon electrode.

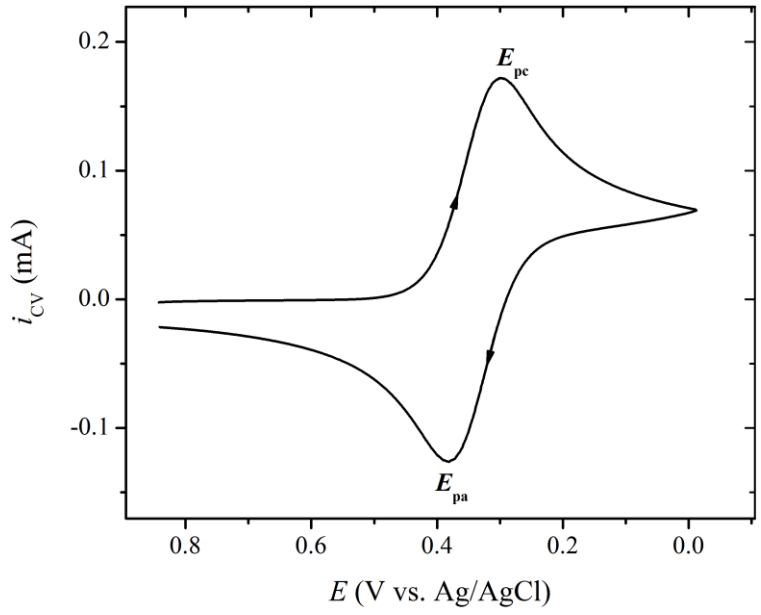

Figure 1.5 Typical cyclic voltammogram of $Fe(CN)_6^{3-}/Fe(CN)_6^{4-}$ redox couple.

Note: CV response of 6.00 mM $K_3[Fe(CN)_6]$ in 0.10 M KNO_3 at a 3-mm glassy carbon electrode with a scan rate of 50.0 mV/s.

1.7.1.2 Experimental Setup and Electrode Modification

The shape of the voltammogram and the value of peak potential provide valuable information, e.g., surface reaction mechanisms. Thus, CV will be predominantly used for investigating of catalytic behavior of newly prepared catalysts towards the electrooxidation of formic acid. This behavior is also compared with that of the commercial materials. Unless otherwise stated, for all CV measurements, a three-electrode electrochemical cell coupled with a computerized potentiostat system (CH Instrument, Austin, TX, USA) is used at room temperature of 24±1 °C. The three electrodes are: (a) Pt (2.0 mm diameter), Au (2.0 mm diameter) or glassy carbon (3.0 mm diameter) (GCE) disk working electrode, (b) either silver/silver chloride, Ag/AgCl (3.0 M KCl) or mercury/mercury sulfate [MSE, Hg/Hg_2SO_4 (satd. K_2SO_4)] reference electrode, and (c) Pt mesh counter electrode.

Figure 1.6 shows the working electrode (WE) modification scheme. Before each electrochemical experiment, the WE is polished with 0.50 µm alumina slurry, rinsed with sufficient amount of Elix® electrodeionized (DI) water. Both working and counter electrodes are then sonicated in ethanol and DI water for 15 min each, respectively. The WE is dried with a Kimwipes® tissue and purged with N_2 gas to blow away any dust particles. The catalysts are ultrasonically dispersed in 10 mL ethanol for 30 min to make the catalyst ink. 9 µL of the ink is then pipetted on the clean WE, and dried at room temperature for 20 min, followed by the casting of 3 µL Nafion® to the top of catalyst ink to wrap the nanomaterials. The electrode is finally dried completely for 30 min prior to use.

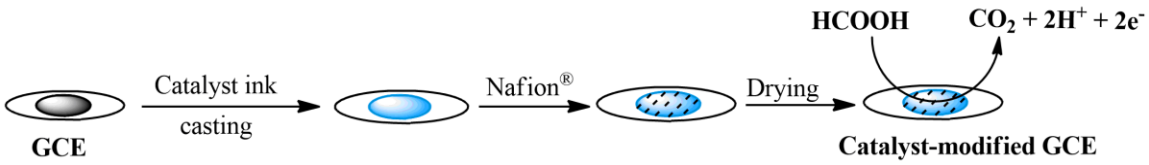

Figure 1.6 Working electrode modification scheme.

1.7.1.3 CV Segments for Formic Acid Oxidation

A typical CV response for FAO is asymmetric at Pt or Pd based catalysts, where different regions can be attributed to the following processes as compared to that obtained from the electrolyte solution (Figure 1.7):[9,126]

1. Forward/anodic sweep (-0.65 to +0.50 V vs. MSE)—

   a. Below -0.6 V vs. MSE: Hydrogen adsorption/desorption region

   b. -0.58 t0 -0.2 V vs. MSE: Dehydrogenation or direct pathway of FAO

   c. Above -0.2 V vs. MSE: Formation of surface oxide and dehydration or indirect FAO pathway, e.g., Pd → PdO_x

2. Reverse/cathodic sweep (+0.50 V to -0.65 V vs. MSE)—

   a. +0.19 V vs. MSE: Reduction of surface oxides, e.g., PdO_x → Pd

   b. -0.19 V vs. MSE: Complete reduction of oxide and further oxidation of HCOOH

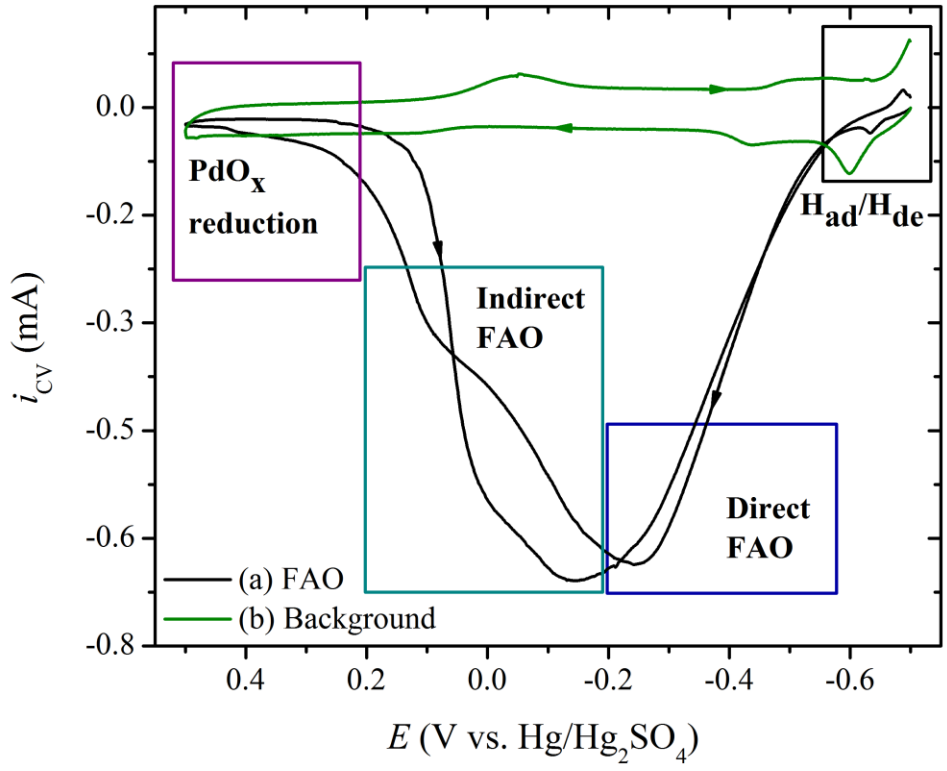

Figure 1.7 Representative cyclic voltammogram regions for FAO.

Note: CV signals obtained from (a) 0.50 M HCOOH in 0.10 M H_2SO_4, and (b) 0.10 M H_2SO_4 blank electrolyte at a 3 mm GCE coated with a thin film of 20 wt% Pd/C (commercial) where the catalytic load was 0.025 mg/cm^2 at a scan rate of 20.0 mV/s.

Figure 1.7 also confirms that the blank electrolyte (0.10 M H_2SO_4) has no impact on FAO except for the hydrogen adsorption/desorption region. Moreover, to lower the adsorption of bisulfate anions, the concentration of HCOOH was maintained as 0.50 M after the initial attempts.[9]

1.7.2 Chronoamperometry (CA)

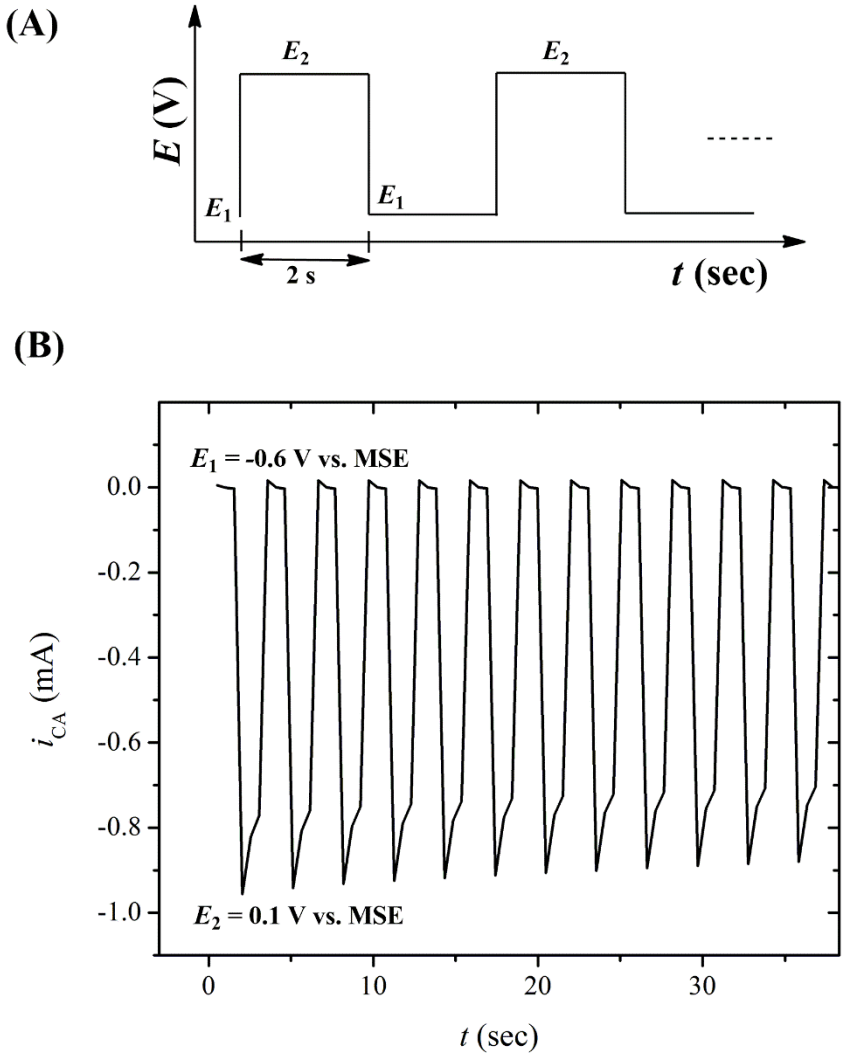

Figure 1.8 Multi-potential step chronoamperometry (CA).

Note: (A) Typical waveform for CA setup where E_1 = -0.6 V and E_2 = 0.1 V vs. MSE, (B) an example of CA response collected using 0.50 M HCOOH in 0.10 M H_2SO_4 at a GCE coated with a thin film of catalyst.

To investigate long-term durability of the prepared nanocatalysts with respect to the commercial catalysts, chronoamperometry (CA) technique will be employed, where FAO current is measured over time at fixed potential values using the same catalytic loads. Figure 1.8A illustrates the waveform applied in the multipotential step CA

experiment. As revealed in the CV responses (Figure 1.7), at potentials less than -0.6 V vs. MSE no FAO occurs. Thus, the initial potential value of E_1 is set as shown in Figure 1.8B. On the other hand, at E_2 = 0.1 V vs. MSE, with FAO, an instantaneous large current flow is obtained, which slightly depletes within 2 sec. After the period of 2 sec step intervals, the potential returns to E_1 and a straight decline in FAO current is observed.[123] Under the same conditions of CV experiments, *i*-t curves are obtained using the catalyst-modified electrode. This simple experimental setup provides useful information including the percentage current change (Δi_{CA}) over time for FAO (Equation 1.6) which presents a direct overview of the catalytic stability and performance towards the use in DFAFCs.

$$\% \text{ Current change, } \Delta i_{CA} = \left(\frac{i_f - i_0}{i_f} \right) \times 100\% \qquad (1.6)$$

1.7.3 Carbon Monoxide Stripping Voltammetry (COSV)

1.7.3.1 Fundamentals of COSV

This technique provides valuable information about fuel-cell catalysts surface, where a monolayer of CO is adsorbed by holding potential for a constant time under a constant flow of CO in a CO-saturated electrolyte. After the adsorption of CO on the catalyst surface at the electrode, CO is removed by purging inert gas like argon or nitrogen. The monolayer is then exposed to CV to desorb the CO completely and subsequent CV cycle is typically used for background correction and to ensure complete desorption of CO. The CO stripping area provides an estimate of electrochemically active surface area (ECSA) of the corresponding catalyst. The onset of CO desorption and shape of the stripping voltammogram are also related to the surface phenomenon.[127-130]

1.7.3.2 CO Oxidation Pathways

It is known that in acidic media, CO is adsorbed almost entirely via the Langmuir-Hinshelwood (L-H) mechanism where CO_{ad} is oxidized by OH_{ad} (Equation 1.7). An alternative Eley-Rideal (E-R) mechanism (Equation 1.8) was also proposed to explain the pre-peak observed in COSV where adsorbed CO is attacked by the water or OH^- from the solution.[127,131-133] Figure 1.9 depicts a schematic of the CO oxidation mechanisms. Consequently, Equation 1.7 b is pivotal for CO oxidation similar to the bifunctional mechanism of FAO. This direct correlation also offers evidence whether alloying enhances dehydrogenation pathway by lowering the active site of CO adsorption and hence, facilitating OH adsorption.

- **The Langmuir–Hinshelwood Mechanism:**

$$H_2O + M \leftrightarrow M\text{-}OH_{ad} + H^+ + e^- \quad (1.7\ a)$$

$$M\text{-}CO_{ad} + M\text{-}OH_{ad} \rightarrow CO_2 + H^+ + e^- + 2\ M \quad (1.7\ b)$$

$$\text{Overall: } CO_{ad} + H_2O_{ad} \rightarrow CO_2 + 2H^+ + 2e^- \quad (1.7)$$

- **The Eley–Rideal Mechanism:**

$$CO_{ad} + H_2O \rightarrow CO_2 + 2H^+ + 2e^- \quad (1.8)$$

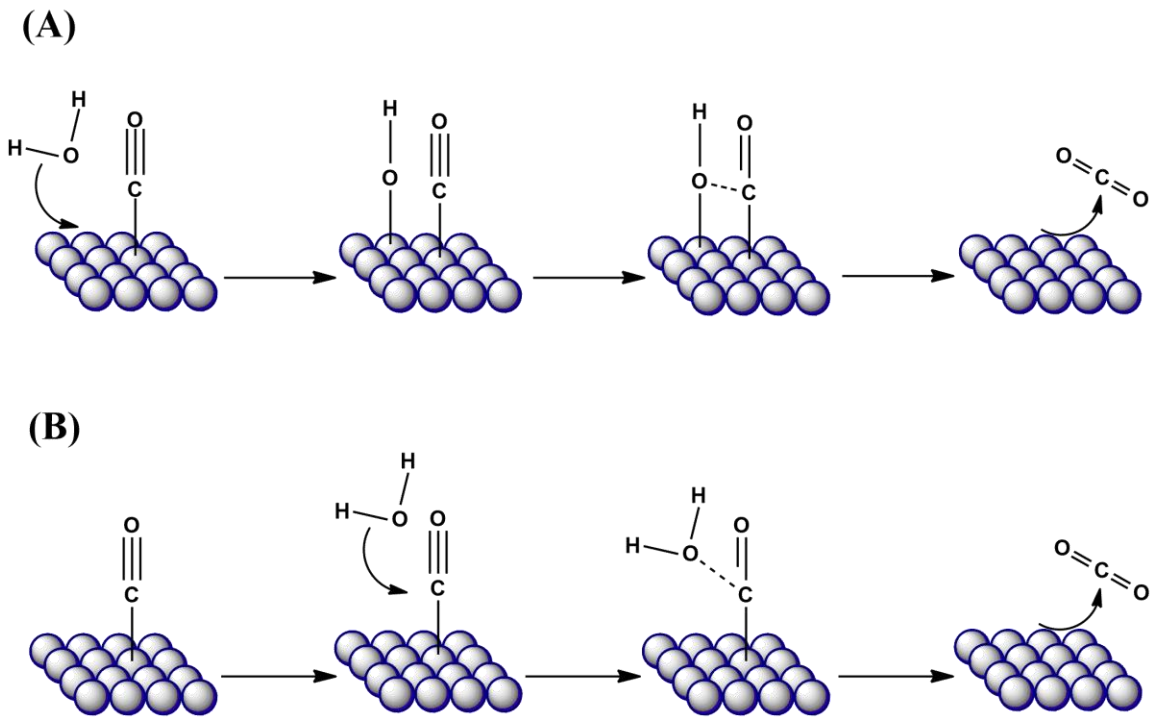

Figure 1.9 Schematic of CO oxidation mechanisms.

Note: (A) The Langmuir-Hinshelwood and (B) the Eley-Rideal mechanisms of oxidation of adsorbed CO by adsorbed oxygen containing species.

1.7.3.3 ECSA Calculation

COSV will be obtained first by purging research grade CO gas in 3 mL 0.10 M $HClO_4$ for 20 min to saturate the electrolyte and a monolayer of CO is electrochemically adsorbed at -0.54 V vs. Hg/Hg_2SO_4 on the respective nanocatalysts (load: 0.100 mg of M/cm^2 of GCE) for 1200 s. The electrolyte is then bubbled with N_2 for 15 min vigorously to completely remove the dissolved CO. CV signals are finally recorded for each catalyst adsorbed with CO from -0.60 to +0.60 V vs. Hg/Hg_2SO_4 at 20.0 mV/s. The stripping of the adsorbed CO from the surface, and succeeding sweep segments are used to verify if the CO monolayer is completely desorbed. The ECSA (cm^2) for the nanocatalysts are estimated using CO stripping area according to the following:[134-139]

$$\text{ECSA} = \frac{n_a \times N_A}{d_m} = \frac{Q_{meas}}{Q_{CO}} \tag{1.9}$$

where, n_a is moles of CO stripped from the surface, and can be calculated From Faraday's Law,

$$n_a = \frac{It}{zF} = \frac{Q_{meas}}{2eN_A} \tag{1.10}$$

where, N_A = Avogadro's number, d_m = surface metal atom density (~ 1.31×10^{15} atoms cm^{-2}), e = electronic charge = 1.602×10^{-19} C, Q_{CO} = oxidation charge to strip adsorbed monolayer of CO = 2e × d_m = 420 μC cm^{-2}, Q_{meas} = area from the COSV, μC = $\frac{1}{\nu}\int_i^f I \cdot dV$, in which, ν = scan rate mV s^{-}, i = onset of CO stripping, and f = end of CO stripping. Therefore,

$$\text{ECSA} = \frac{Q_{meas}}{420} cm^2 \tag{1.11}$$

1.8 Structural Characterization

Scanning electron microscope (SEM) images are captured with a Zeiss Sigma VP, FE-SEM operating at 20 kV and utilizing the secondary and backscatter detectors. Images were taken at low magnifications (100 to 200x) to show overall distribution and homogeneity of the sample, and to locate segments of interest. These areas of interest are then viewed at higher magnifications (3,000 to 60,000x) to analyze the morphology of the particles at the nanometer scale. In addition to imaging with the SEM, a Thermo Scientific UltraDry energy-dispersive X-ray spectroscopy (EDS) detector with NSS 3 microanalysis software is used to investigate the elemental distribution and characterization of the samples. EDX mapping is also utilized for

composite catalysts to evaluate homogeneity, particle distribution, and bulk metal compositions. All samples are first dispersed in ethanol by ultrasonication and then drop casted on clean silicon wafers. After drying, the coated wafers were sputtered with silver, and the instrument calibrated with a pure copper before capturing the images and EDX analyses.

Lastly, for template assisted catalysts, to examine the particle shape and size precisely a JEOL 2100 transmission electron microscope (TEM) operating at 200 kV is utilized. Samples are prepared on copper mesh grids with Formvar support film.

CHAPTER II – INHIBITIVE EFFECT OF CHLORIDE IONS ON Pd/C NANOCATALYST TOWARDS FORMIC ACID ELECTROOXIDATION

2.1 Introduction

One of the unresolved problems for the booming commercialization of direct formic acid fuel cells (DFAFC) is the lack of appropriate catalysts that show high activity towards formic acid oxidation (FAO) (Equation 2.1) and stability against poisoning. As discussed in Chapter I, the electrocatalytic oxidation of formic acid (HCOOH) to CO_2 proceeds via a "dual pathway" mechanism characterized by the following equations,[4,5,7]

At the anode: $HCOOH \rightarrow CO_2 + 2H^+ + 2e^-$ $E° \sim -0.25$ V vs SHE (2.1)

$HCOOH \rightarrow$ reactive intermediates $\rightarrow CO_2 + 2H^+ + 2e^-$ (dehydrogenation step) (2.1a)

$HCOOH \rightarrow CO_{ad} + H_2O \rightarrow CO_2 + 2H^+ + 2e^-$ (dehydration step) (2.1b)

where direct oxidation of reactive weakly-adsorbed intermediates to CO_2 through dehydrogenation (Equation 2.1a) occurs in parallel with the indirect oxidation pathway involving HCOOH dehydration and subsequent electrooxidation of the resultant strongly-adsorbed CO to CO_2 (Equation 2.1b) via bifunctional or third-body effect mechanisms depending on the electrocatalyst utilized.[9]

Typically, Pt or Pd nanocatalysts on carbon-based support material are used commercially among many other transition metals based electrocatalysts.[15,17,22,25,57,65] The common contaminants that poison the catalyst and have adverse effect on the durability are mostly halide ions from the synthesis of catalysts, water feed, airborne salts etc. The dissolution and inhibition of catalytic activity of transition metal-based catalysts due to the presence of halide ions for PEM based fuel cells are also of great concern but have been rarely studied.[140-148] Given the fact that Ag/AgCl (3.0 M KCl) or Hg/Hg_2Cl_2 (sat.

KCl) reference electrodes, which could be a significant source of chloride ions, are still widely used in fuel cell studies when Pd or Pt is used as an electrocatalyst.[40,58,62,77,88,138,149-151] Thus, it would be interesting to observe if the use of such a reference electrode could significantly affect the electrooxidation performance of formic acid at Pd/C on GCE. In other words, from now on, should a chloride containing reference electrode, e.g., Ag/AgCl or Hg/Hg_2Cl_2, be replaced with a non-chloride chloride containing reference electrode in fuel cell studies? On the other hand, for research purposes, the modification of the working electrode using nanomaterials to promote high surface area for direct electrooxidation of formic acid has been extensively studied.[4,5,9,152]

This chapter focuses on the effect of chloride ions on the electrooxidation of formic acid when Pd/C is used as the electrocatalyst. The results could provide a guideline on how to choose a suitable reference electrode for fuel cell studies so that reproducible results can be obtained. Therefore, we report the correspondence between the inhibitive behavior of the chloride ions either added or leached from the Ag/AgCl (3.0 M KCl) reference electrode and the decline in electrooxidation peak current of FAO.

2.2 Experimental Section

2.2.1 Chemicals

All starting materials, including carbon supports and electrolytes were commercially available and were used as received. From Sigma-Aldrich, $PdCl_2$ (99%) and Nafion perfluorinated resin solution (Nafion®, 5 wt% in 2-propanol, *n*-propanol; 15-20% water) were purchased. $NaBH_4$ (≥99%), HCOOH (50%, HPLC Grade) were purchased from Fluka Analytical. H_2SO_4 (Certified ACS Plus, 95.0 - 98.0 w/w%) and

HCl (Certified ACS Plus, 12.1 normality) were obtained from Fisher Scientific. Graphite nanoparticles (GNP) (~10 nm) was purchased from ACS Materials. Vulcan XC-72 was obtained from Cabot Corp. and graphite powder from Central Scientific Co. (CENCO). The commercial 20 wt% Pd/C (Palladium, 20% on activated carbon powder, standard, reduced, normally 50% water wet) catalyst was purchased from Alfa Aesar.

2.2.2 Preparation of Pd/C

2.2.2.1 Preparation of Pd/GNP and Pd/Graphite

Palladium catalysts on carbon supports were synthesized as reported with some modifications.[17] Anhydrous $PdCl_2$ (35.5 mg, 0.200 mmol) dissolved in 40.00 mL of 0.10 M HCl was sonicated and stirred for 3 h with 10.0 mg graphite nanoparticles (GNP) (~10 nm) and graphite separately. Excess $NaBH_4$ (75.7 mg, 2.000 mmol) was dissolved in 20.00 mL DI water and added into the above mixture as reducing agent with a mini-flow variable-speed pump (VWR International). The black particles were then centrifuged, washed exhaustively with deionized (DI) water and ethanol. Then the Pd/GNP and Pd/graphite were collected under ethanol and air dried. The weight ratio of Pd to carbon support was about 2:1.

2.2.2.2 Preparation of 20 wt% Pd/Vulcan-XC 72

Anhydrous $PdCl_2$ (20.0 mg, 0.113 mmol) was dissolved in 3.13 mL 0.10 M HCl using ultrasonication. 60 mg Vulcan XC-72 carbon was mixed with the $PdCl_2$ solution and 6.87 mL DI water was added to make the final volume of the mixture to 10.00 mL. The suspension obtained was ultrasonicated for 30 min and stirred for 4 h. The pH of the suspension was adjusted to pH ~9 with few drops of concentrated Na_2CO_3 solution. 20.00 mL of $NaBH_4$ (52.9 mg, 1.4 mmol) solution was then delivered into the above mixture as

reducing agent with a mini-flow variable-speed pump (VWR International) and further stirred for 2 h. Subsequently, the mixture was filtered, washed several times with DI water to remove any excess reagents and dried in the vacuum oven at 60 °C for 12 h. The 20.0 wt% Pd/C was then collected and stored in a desiccator.

2.2.3 Chemical Characterization

The morphology of the synthesized Pd/GNP and Pd/graphite were analyzed with scanning electron microscopy (SEM, Zeiss Sigma VP) and the compositions were studied with electron dispersive X-ray spectroscopy (EDX) on SEM using the Thermo Scientific UltraDry EDS Detector with NSS 3 microanalysis software. SEM samples were prepared by dispersing freshly ultrasonicated materials in ethanol on Si wafer followed by air drying.

2.2.4 Immobilization of Catalyst Ink

Before the immobilization of the catalyst ink, the working electrode (WE) was polished with 0.50 µm alumina slurry, rinsed with sufficient amount of DI water. Both working and counter electrodes were then sonicated in ethanol and DI water for 15 min each, respectively. The WE was dried with a Kimwipes® tissue and purged with N_2 gas to blow away any dust particles. The catalysts were ultrasonically dispersed in 10.00 mL ethanol for 30 min to make the catalyst ink. The ink (9.0 µL) was then pipetted on the clean WE, and dried at room temperature for 20 min, followed by the casting of 3.0 µL Nafion® to the top of the catalyst ink to wrap the nanomaterials. The electrode was finally dried in air completely for 30 min prior to use.

2.2.5 Electrochemical Measurements

Unless otherwise stated, for all electrochemical measurements, a three-electrode electrochemical cell coupled with a CHI 900B computerized potentiostat system (CH Instrument, Austin, TX, USA) was used at room temperature of 24±1 °C. The three electrodes were: (a) Pt (2.0 mm diameter), Au (2.0 mm diameter), or glassy carbon (3.0 mm diameter) (GCE) disk working electrode; (b) either silver/silver chloride, Ag/AgCl (3.0 M KCl), or mercury/mercury sulfate (MSE), Hg/Hg_2SO_4 (satd. K_2SO_4) reference electrode (CH Instrument); and (c) Pt mesh counter electrode. The electrolytes were deaerated with ultrapure N_2 gas for 15 min and all electrochemical measurements were done under N_2 atmosphere. The CV responses of FAO were measured in a 2.00 mL solution containing 0.50 M HCOOH and 0.10 M H_2SO_4 at GCE coated with Pd/C. To detect the influence of chloride ions on electrooxidation of HCOOH, the CV experiments were conducted with electrolytes containing different concentrations of added KCl. Alternatively, the experiments were performed in electrolyte solutions in contact with a Ag/AgCl (3.0 M KCl) reference electrode for different periods of time. The leached Cl^- ions effect on FAO was subsequently investigated. In this case, 3.0 M KCl was introduced to the Ag/AgCl electrode before each time the reference electrode was submerged into the formic acid so that the volume or pressure inside the glass tube of the reference electrode remained the same.

2.3 Results and Discussion

2.3.1 Characterization of the Pd/GNP and Pd/Graphite Catalysts

The SEM images in Figure 2.1 show the formation of nanoparticles of ~20-50 nm size distribution on the carbon supports. The Pd particles are larger than GNP (~10 nm, not shown) but smaller than graphite (~200 – 500 nm, see Figure 2.4 for details). The EDX spectra and elemental analyses on different SEM spots of interest (Figure 2.2) confirm that Pd nanoparticles are indeed deposited on the carbon support of GNP (Figure 2.2a) and graphite (Figure 2.2b).

As the samples were prepared on clean Si wafers placed on Al stubs, there elements as well as some surface oxygen are present in the spectra. Table 2.1 summarizes the estimated weight% of elements presented in the samples. The large weight% ratio of Pd to C could indicate that the carbon support is "wrapped" with Pd nanocatalysts.

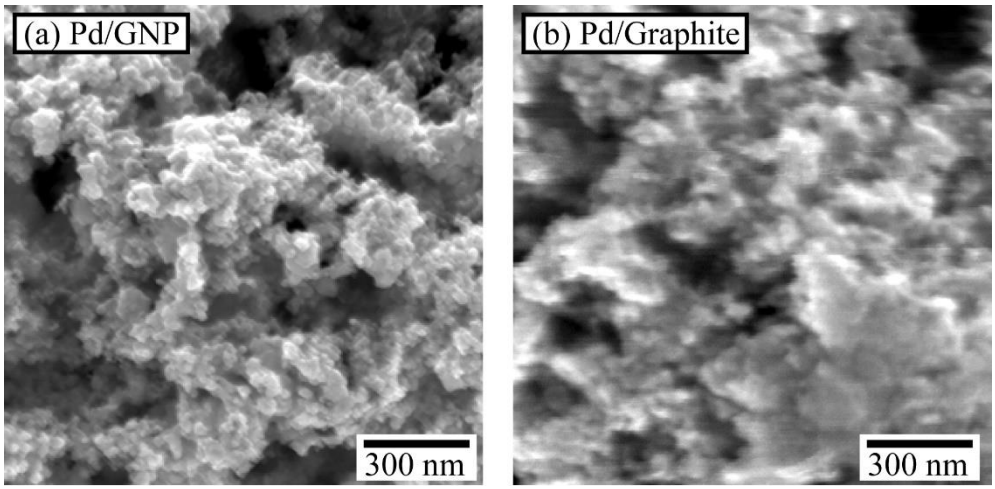

Figure 2.1 SEM images of (a) Pd/GNP and (b) Pd/Graphite.

Note: Images were captured at 20 kV and 50,000 x magnification without Ag sputtering.

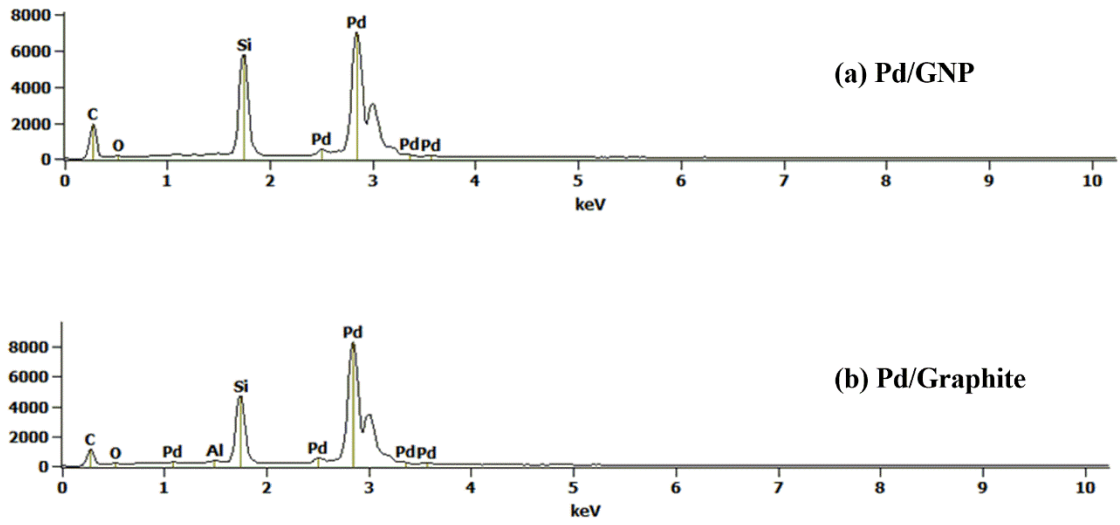

Figure 2.2 EDX spectra of (a) Pd/GNP and (b) Pd/Graphite.

Note: EDX spectra display the elemental distribution of the prepared (a) Pd/GNP and (b) Pd/graphite nanomaterials that were casted on Si wafers attached to Al-stubs.

Table 2.1

Estimated elemental composition of Pd/GNP and Pd/Graphite by EDX.

Weight %	**C**	**Pd**	**Si**	**O**	**Al**
Pd/GNP	14.88±0.17	66.35±0.37	17.66±0.11	1.11±0.20	-
Pd/graphite	7.73±0.16	75.43±0.52	14.45±0.10	1.99±0.35	0.39±0.04

2.3.2 Formic Acid Electrooxidation on Pd/C with Ag/AgCl Reference Electrode

Many reports in the literature have shown that the cyclic voltammogram of FAO on Pd/C or Pt/C illustrates an asymmetric response between the forward and reverse potential scans.[9] Our initial studies, however, could not repeat such results. As shown in Figure 2.3, at Pd/GNP (Figure 2.3a) or Pd/graphite (Figure 2.3b) coated electrode, the FAO current on the forward scan is much larger than that on the reverse scan. The higher peak current from Pd/GNP with respect to that from Pd/graphite can be attributed to the

fact that the former has much smaller particle size, hence larger surface area and better surface distribution as revealed by the SEM images shown in Figure 2.4, where Pd/GNP (Figure 2.4a) and Pd/graphite (Figure 2.4b) were casted on a Si wafer after respective catalyst ink was dispersed in ethanol and Nafion®.

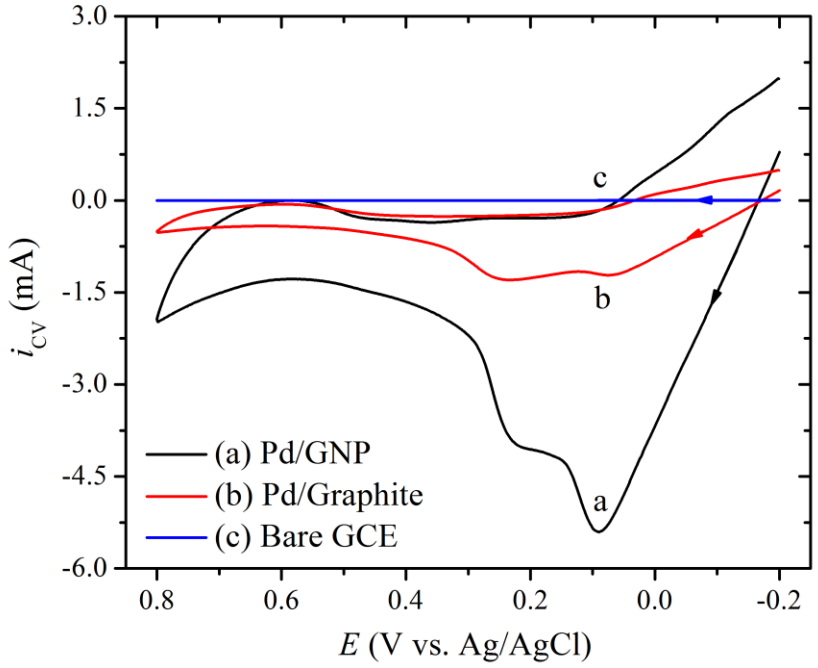

Figure 2.3 Formic acid oxidation CV responses using Ag/AgCl (3.0 M KCl) reference electrode.

Note: CV signals of 0.10 M HCOOH - 0.10 M H_2SO_4 using GCE coated with (a) Pd/GNP, (b) Pd/graphite, and (c) bare GCE electrode using Ag/AgCl (3.0 M KCl) reference electrode at a scan rate of 50.0 mV/s.

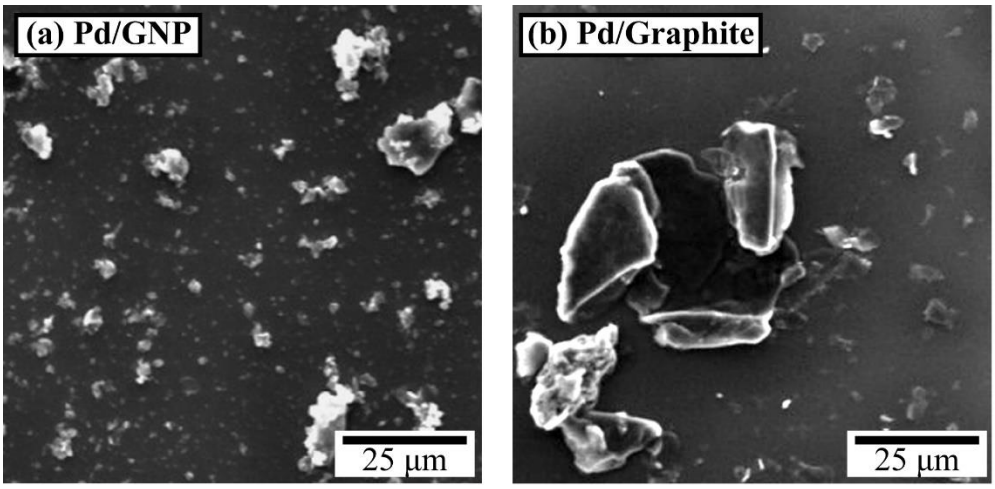

Figure 2.4 SEM images of nanocatalysts coated with Nafion®.

Note: (a) Pd/GNP and (b) Pd/graphite were dispersed in ethanol mixed with Nafion® solution before casting on the Si wafers.

Similar "unusual" CV behavior was observed from Pd/Vulcan XC-72 and commercial Pd on activated carbon (not shown) when Ag/AgCl reference electrode was used (Figure 2.5A). As shown in Figure 2.5A, upon the anodic potential scanning, HCOOH is electrocatalytically oxidized at the Pd/Vulcan XC-72/GCE with an anodic peak current of 0.72 mA. On the reverse scan, however, the oxidation peak current is significantly decreased to 0.26 mA. The subsequent CV cycle shows an anodic peak current of 0.31 mA and a cathodic oxidation peak current of 0.08 mA. In other words, when a Ag/AgCl reference electrode is used, the FAO current decreases remarkably over the potential cycling or time.

On contrast, as shown in Figure 2.5B, the above CV behavior is completely changed right after the Ag/AgCl (3.0 M KCl) reference electrode is replaced with a Hg/Hg_2SO_4 (satd. K_2SO_4) whereas other experimental conditions remain the same. Clearly, the electrocatalytic oxidation current of HCOOH on forward and reverse scan is close (2.34 mA vs. 2.52 mA for the 1st CV cycle), and the current decrease over potential

cycling or time is small. Moreover, under the same catalytic load (*i.e.*, 0.025 mg Pd/cm^2 of GCE), pre-waiting time of CV scanning (*i.e.*, a time window between the electrodes are placed in the electrolyte solution and the CV scan starts), much larger oxidation peak current (~2.4 mA) is observed using Hg/Hg_2SO_4 reference electrode (Figure 2.5A) when compared with its counterpart using Ag/AgCl reference electrode (Figure 2.5B). Note that, in Figure 2.5B, the minor hump around 0.19 V vs. Hg/Hg_2SO_4 on the forward scans can be attributed to the Pd oxidation and indirect FAO pathway. On the reverse scan, the sudden jump in FAO current could be explained that at this potential (~0.04 V), the initially oxidized Pd surface is largely reduced back to fresh Pd resulting in large catalytic oxidation of HCOOH.

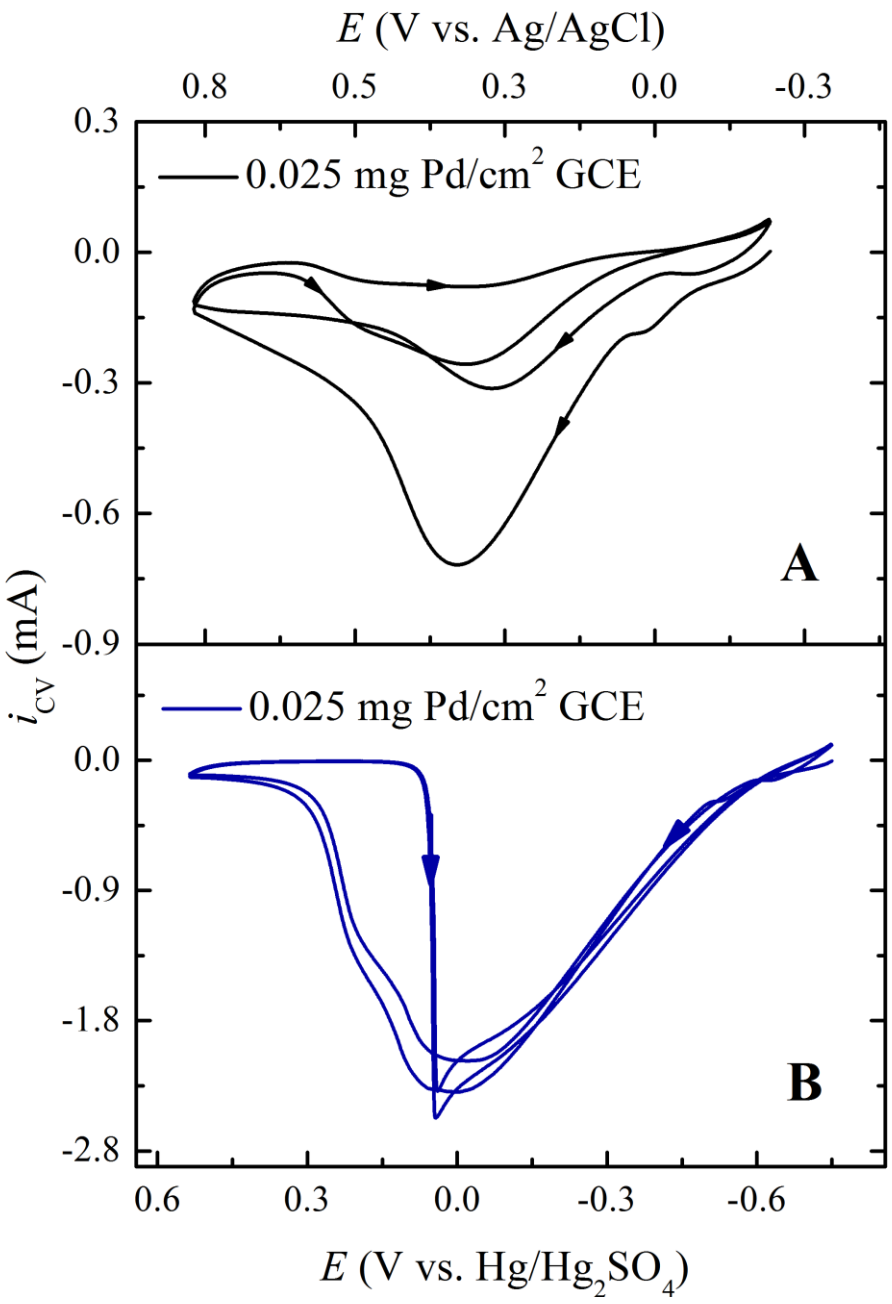

Figure 2.5 Comparison of CV signals collected using Ag/AgCl vs. Hg/Hg_2SO_4 reference electrodes.

Note: CV responses of 0.10 M HCOOH - 0.10 M H_2SO_4 using GCE coated with 20 wt% Pd/Vulcan XC-72 catalyst (0.025 mg Pd/cm^2 load) using: (A) Ag/AgCl (3.0 M KCl) and (B) Hg/Hg_2SO_4 (satd. K_2SO_4) reference electrodes at a scan rate of 20.0 mV/s.

To verify this phenomenon, new experiments using the commercial 20 wt% Pd/C with the same catalytic load and Hg/Hg_2SO_4 reference electrode were conducted at various scan rates (Figure 2.6). As expected, with the increase of scan rate, the overall current of FAO increases. When the scan rate is increased from 10 mV/s (Figure 2.6A) to 20 mV/s (Figure 2.6B), the "stripping" peak on the cathodic scan starts to appear. At higher scan rates (Figures 2.6c-e), "stripping" oxidation become evident. This is characteristic of the sudden increase in effective catalytic surface after the Pd oxide reduction.[77] Therefore, to avoid ambiguity between the "stripping" peak and FAO peak, the optimized scan rate of 20.0 mV/s was used throughout the projects in this dissertation.

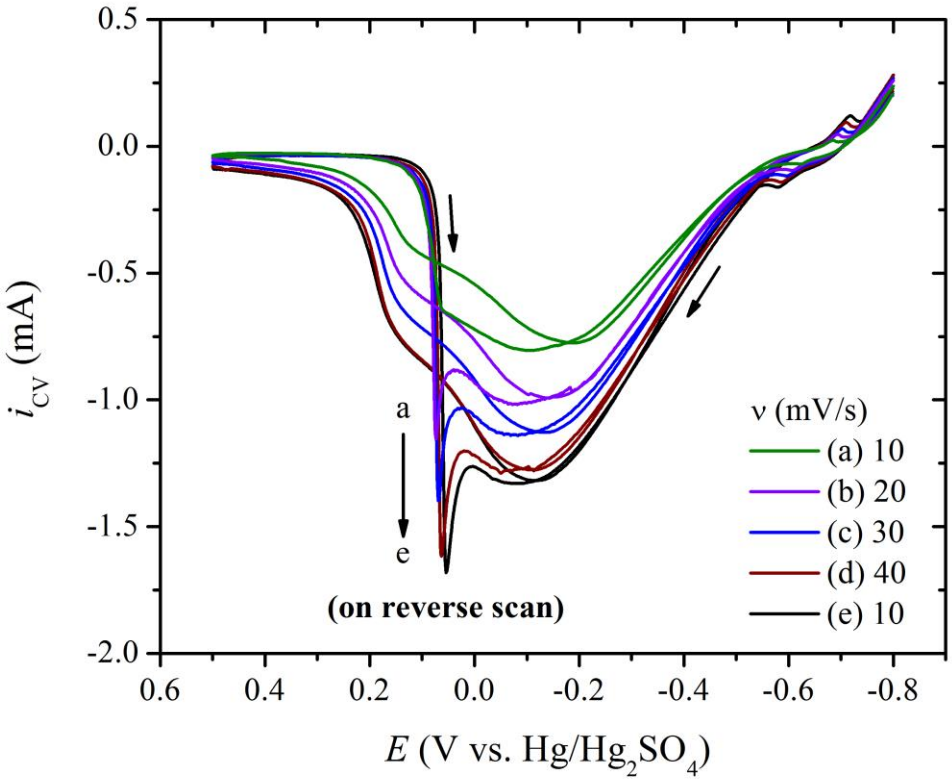

Figure 2.6 Effect of scan rates on FAO at 20% Pd/C.

Note: CV signals collected from 0.50 M HCOOH in 0.10 M H_2SO_4 where 0.025 mg Pd/cm^2 load at GCE using Hg/Hg_2SO_4 (satd. K_2SO_4) was utilized 20 wt% Pd/C commercial catalyst at the scan rate of (a) 10.0 mV/s to (e) 50.0 mV/s.

After validating all the experimental conditions such as purity of formic acid and supporting electrolyte, protocols to clean the electrodes and vials, it was conclusive that chloride ions could be the cause of "unusual" CV responses when Ag/AgCl (3.0 M KCl) was used as the reference electrode, that needs to be further investigated.

2.3.3 Impact of Chloride Ions on Electrocatalytic Oxidation of Formic Acid

Electrooxidation of formic acid in presence of the sulfuric acid as supporting electrolyte has been usually quantified or compared using 20 wt% Pd nanoparticles on carbon-based supporting materials.[4,5,9,153] Therefore, commercial 20 wt% Pd on activated carbon (Pd/C) was used as catalyst, and drop casted on GCE (0.025 mg Pd/cm^2) to evaluate CV behavior of the 0.50 M HCOOH – 0.10 M H_2SO_4 system. As shown in Figure 2.7a, in the absence of chloride ions, the CV response (forward scan) shows typical electrooxidation peak at ~ -0.10 V vs. Hg/Hg_2SO_4 (satd. K_2SO_4). After addition of chloride ions into the formic acid, the oxidation current significantly decreases with the increase of chloride ion concentrations (Figure 2.7b-i). For example, a peak current of 1.04, 0.70, and 0.03 mA is seen for a chloride concentration of 0, 0.5, and 7.0 mM, respectively. In other words, the oxidation current is reduced by ~97% at [Cl^-] = 7.0 mM with respect to that of [Cl^-] = 0 mM. Figure 2.7B displays the overall trend of anodic peak current change for FAO over a range of added chloride ion concentrations. Additionally, the oxidation peak potential is shifted towards the negative potential with the increase of chloride ion concentrations. These data suggest that chloride ions can inhibit the FAO at Pd, probably by strong adsorption on the Pd surface, thereby blocking

considerable amount of active Pd surface needed for catalytic oxidation of HCOOH (see Section 2.3.5 for details).

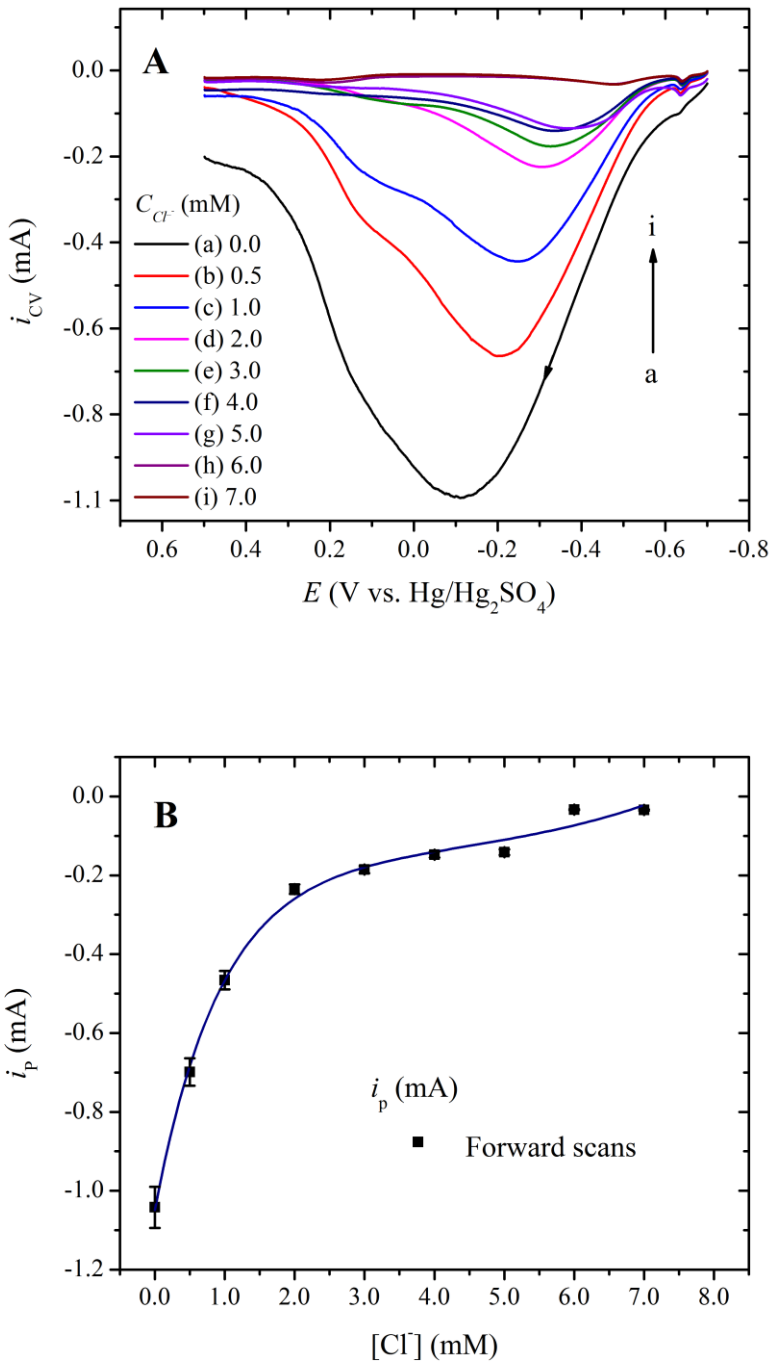

Figure 2.7 Effect of added [Cl^-] on formic acid oxidation at 20% Pd/C modified GCE.

Note: CV responses to obtain the effect of [Cl^-] (A) on the anodic current of FAO and (B) overall trend from 0.0 mM to 7.0 mM of added KCl to 0.50 M HCOOH in 0.10 M H_2SO_4 obtained from GCE coated with Nafion® modified 20% Pd/C (commercial) at a scan rate of 20.0 mV/s. Catalytic load: 0.025 mg Pd/cm^2 of GCE.

To investigate the effect of chloride ions leaked from the frit of a typical Ag/AgCl (3.0 M KCl) reference electrode, a Ag/AgCl (3.0 M KCl) electrode was immersed in a freshly prepared HCOOH-H_2SO_4 electrolyte solution each time at 1 min intervals starting from 1 min up to 10 min. Figure 2.8 outlines the decrease of CV responses over the time used for Ag/AgCl immersion (Figure 2.8A) and the overall trend of peak current along with the immersion time (Figure 2.8B). After submerging the Ag/AgCl electrode into the electrolyte solution for 7-10 min, FAO current signals become barely detectable, elucidating that the Pd catalyst surface could have exhausted to further oxidize formic acid.

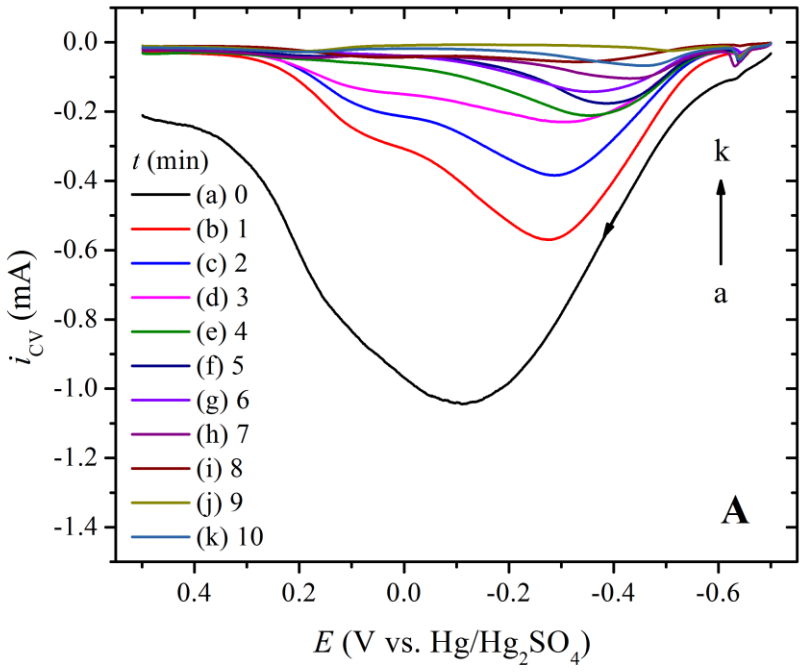

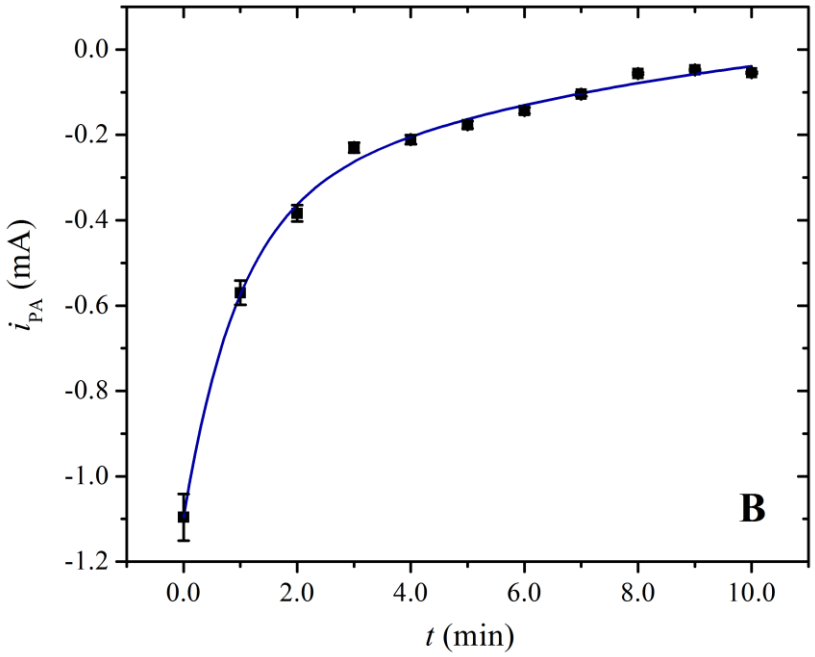

Figure 2.8 Time-dependent study of leached Cl^- ions on formic acid oxidation.

Note: Effect of chloride ions leaked from the frit of a Ag/AgCl (3.0 M KCl) reference electrode over time from 0 to 10 min. (A) CVs of the electrooxidation of HCOOH and (B) overall trend of peak current change after immersing the reference electrode in 0.50 M HCOOH mixed with 0.10 M H_2SO_4 obtained from GCE coated with Nafion® modified 20% Pd/C at a catalytic load of 0.025 mg Pd/cm^2 of GCE and a scan rate of 20.0 mV/s was used.

2.3.4 Estimation of Leaked Chloride Ion Concentration

To estimate the amount of chloride ions leaked from the frit of the reference electrode, the Ag/AgCl electrode was immersed in solution containing 10.0 mM $AgNO_3$ – 0.10 M $LiNO_3$ at 2.5 min intervals from 0.0 to 12.5 min. White precipitation of AgCl was expected (due to the Ag^+ ions reaction with the leaked Cl^-) and observed upon immersion of the Ag/AgCl (3.0 M KCl) electrode. The amount of precipitate continued to increase with time as more of the leaked chloride ions reacted with silver ions. Consequently, the free [Ag^+] remained in the electrolyte solution was decreased and

estimated using cyclic voltammetry, in which a freshly polished Au working electrode and a Hg/Hg_2SO_4 reference electrode was used.

The CV signals illustrated in Figure 2.9A show the decline of the reduction peak currents of Ag^+ ions, which is directly related to the chloride ions concentration as the molar ratio of Ag^+ ions consumed by the leaked Cl^- ions was 1:1. The trend of the Ag^+ reduction peak current change over time (Figure 2.9B) shows that at 10 min, the reduction peak current depletes completely. In other words, at this time the leaked Cl^- concentration should be close to 10.0 mM.

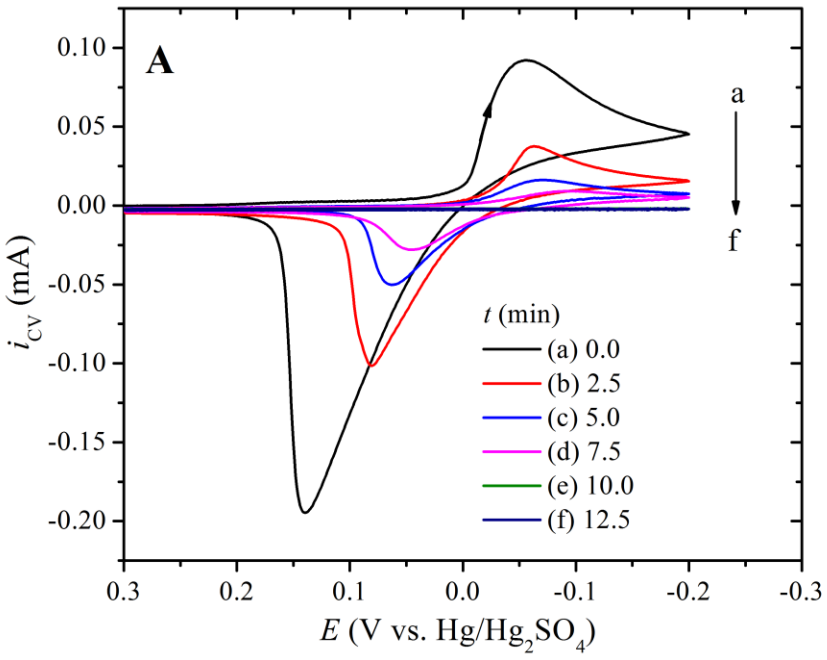

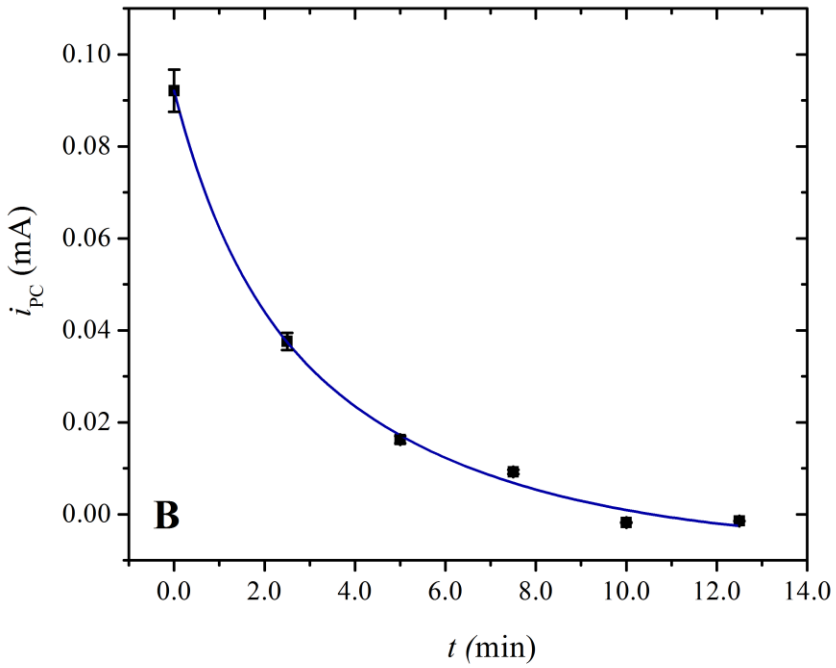

Figure 2.9 Time-dependent study to estimate the leaked [Cl^-].

Note: Estimation of chloride ions leaked from the frit of a Ag/AgCl (3.0 M KCl) reference electrode over time up to 12.5 min. (A) CVs of Ag^+ ions and (B) Ag^+ reduction peak current change as a function of the immersion time of Ag/AgCl in 10.0 mM $AgNO_3$ - 0.10 M $LiNO_3$. CVs were run at a 2 mm Au electrode at a scan rate of 50.0 mV/s.

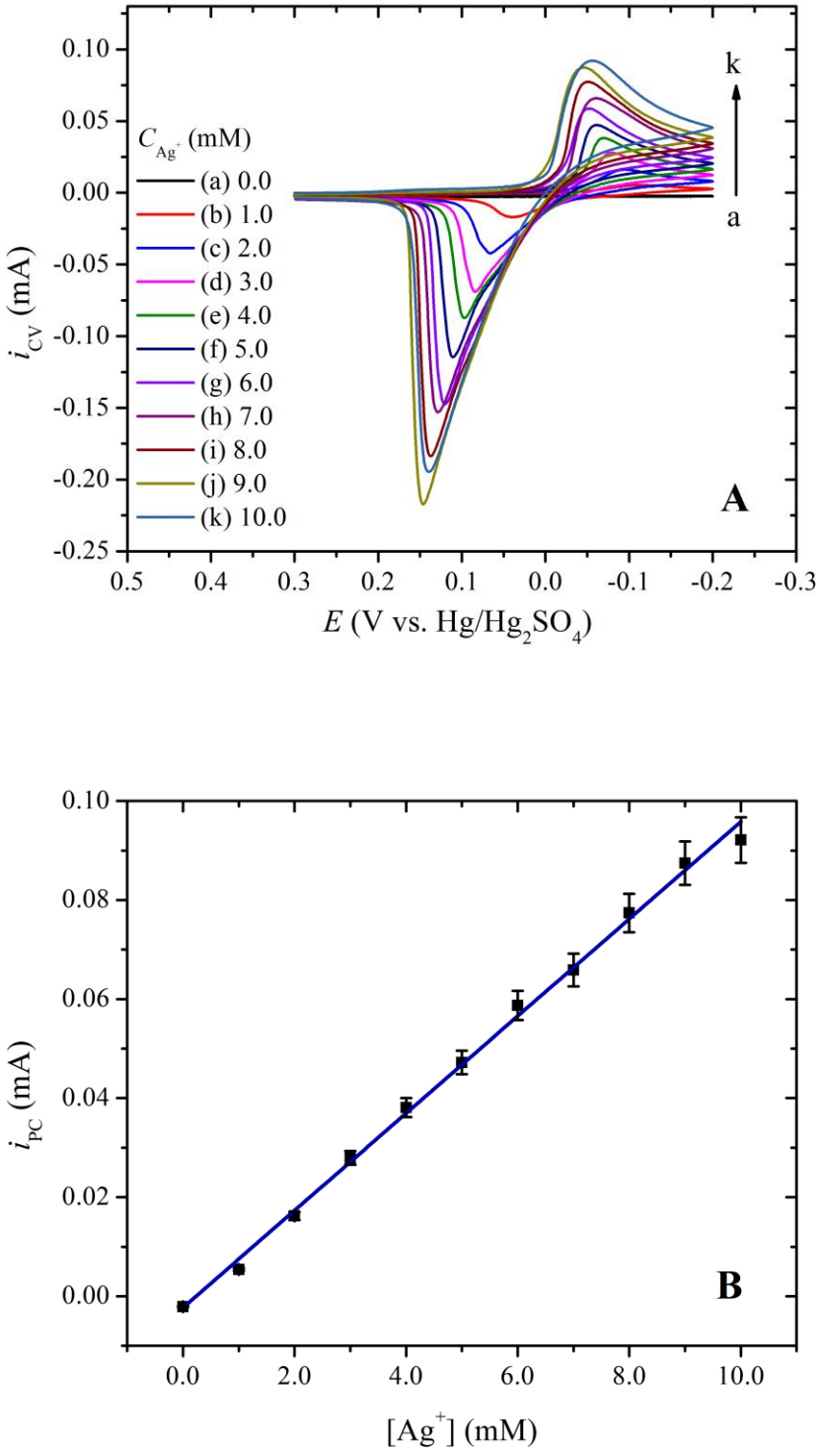

Figure 2.10 Standard $AgNO_3$ – $LiNO_3$ calibration curve.

Note: CV signals of: (A) silver ions reduction peak current and (B) standard calibration curve of $AgNO_3$ in 0.10 M $LiNO_3$ obtained from Au electrode at a scan rate of 50.0 mV/s.

To estimate the concentration of chloride ions, one must find the concentration of Ag^+ remained in the solution. Figure 2.10A shows the CV responses of standard $AgNO_3$ solutions. A linear relationship between the Ag^+ reduction peak current and the Ag^+ concentration is plotted in Figure 2.10B. Accordingly, the Ag^+ concentration in Figure 2.9 can be estimated. As a result, the leaked Cl^- from Ag/AgCl reference electrode at a given time is calculated as shown in Figure 2.11.

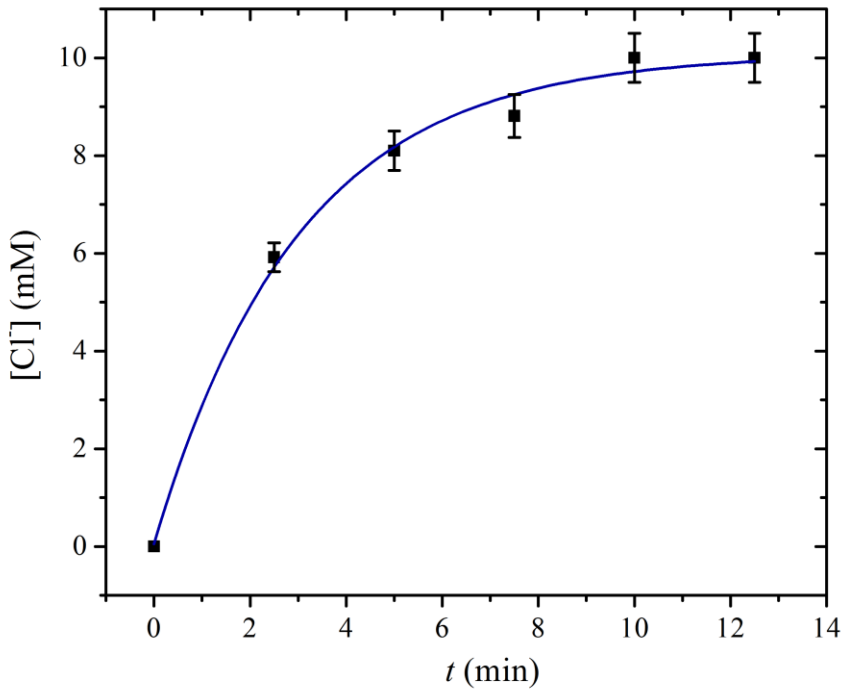

Figure 2.11 Correlation between leached $[Cl^-]$ vs. time.

Note: Evaluation of the amount of leaked chloride ion from the frit of a Ag/AgCl (3.0 M KCl) reference electrode.

Considering the results of Figure 2.8 and 2.11, it is clear that after ~8-9 min of immersion of the Ag/AgCl reference electrode, $[Cl^-]$ reaches about 9.0 mM and the FAO

current approaches to 0 mA, *i.e.*, the catalytic activity of Pd is nearly completely lost. Note that the above estimation could vary depending on the materials used such as the pore size of the frit of the Ag/AgCl reference electrodes, the concentration of KCl electrolyte, and the loading of Pd catalyst.

2.3.5 Proposed Chloride Ion Inhibition Mechanism of Pd Catalyst for Formic Acid Oxidation

Based on the data presented and the literature review, in the absence of chloride ions, formic acid oxidation involves the direct and the indirect pathways (Scheme 2.1A).[9,154] The direct FAO pathway involves the adsorption of HCOOH on the catalyst surface which forms CO_2 *via* reactive intermediate formation or, so-called C-H activation. Whereas, the indirect pathway of FAO comprises of the adsorption of CO which forms CO_2 with the OH_{ad} on a catalyst surface.[154] However, the presence of Cl^- ions could lower the active catalytic sites, thereby inhibit FAO (Scheme 2.1B).

Specifically, chloride ions could hinder the formation of essential OH_{ad} for formic acid dehydration step (indirect pathway) and further inhibit the formation of CO_2. In the presence of chloride ions formic acid oxidation peak current decreases significantly, where the chloride ions are competitively being adsorbed on the effective catalyst surface due to electrostatic attraction between the chloride anion and the metal (Pd).

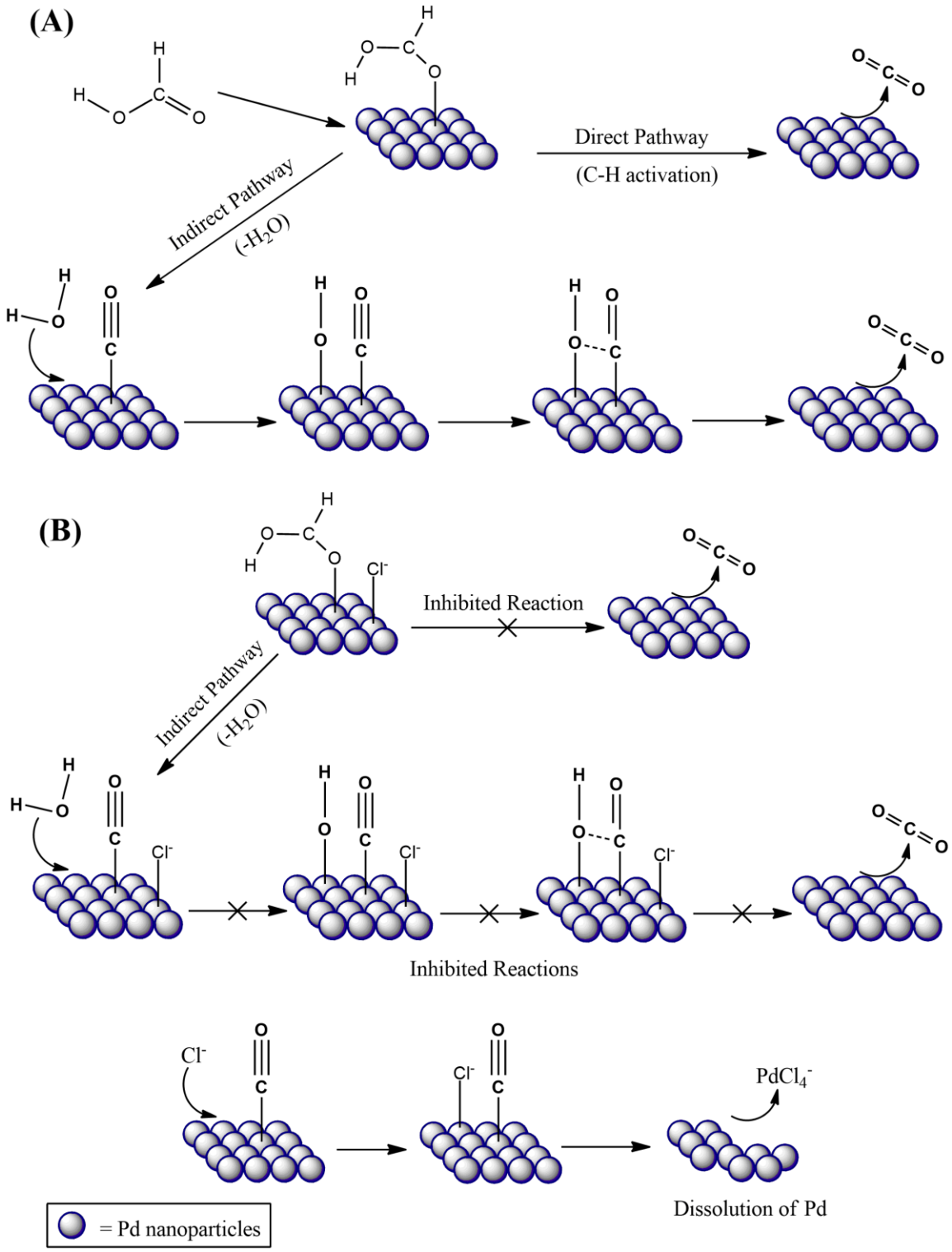

Scheme 2.1 Proposed formic acid oxidation mechanism and inhibitive effect of Cl^- on Pd catalyst.

Note: (A) In the absence of chloride ions FAO follows "dual pathway" mechanism; (B) In the presence of chloride ions, adsorbed chloride ions are blocking the active catalyst sites, and possible dissolution of Pd nanomaterials after formation of palladium-chloride complex ions.

Consequently, the crucial steps for FAO (Scheme 2.1A) are constraining by the adsorbed Cl^- ions lowering the amount of OH_{ad} and active Pd nanomaterial surface (Scheme 2.1B). On the other hand, presence of chloride ions could potentially result in the dissolution of the metal particles, *i.e.*, Pd from the surface (Scheme 2.1B).

2.4 Conclusion

The depleted FAO current from the CV responses while using the Ag/AgCl reference electrode was investigated towards the inhibitive effect of chloride ions on Pd/C. This work confirms that only a few mM (~6.0 mM) of chloride containing impurities could drastically hinder FAO activity at GCE coated with Pd/C (0.025 mg Pd/cm^2 of GCE). Additionally, the immersion of Ag/AgCl into the formic acid electrolyte for ~6-8 min could inhibit the catalytic activity of Pd for FAO. Hence, chloride ion containing reference electrodes such as Ag/AgCl (3.0 M KCl), saturated calomel electrode [Hg/Hg_2Cl_2 (satd. KCl), SCE] should be avoided for the electrochemical studies of FAO to circumvent the chloride contamination. Consequently, non-chloride containing reference electrodes, e.g., Hg/Hg_2SO_4 (satd. K_2SO_4), and standard hydrogen electrode (SHE), are recommended.

CHAPTER III – INVESTIGATION OF FORMIC ACID ELECTROOXIDATION OVER Pd AND PdNiCo TERNARY NANOCATALYSTS ON NANOSTRUCTURED CARBON SUPPORTS

3.1 Introduction

As discussed in Chapter I, the challenge to commercialize direct formic acid fuel cells (DFAFCs) is mainly the utilization of cost effective, stable against poisoning, high performance, and durable anodic catalyst for formic acid oxidation (FAO). The "dual pathway" mechanism characterized by the following equations can be elaborated further on a bimetallic composite catalyst as follows,[4,5,7,153]

$HCOOH \rightarrow$ reactive intermediates $\rightarrow CO_2 + 2H^+ + 2e^-$ (dehydrogenation step) (3.1a)

$HCOOH \rightarrow CO_{ad} + H_2O \rightarrow CO_2 + 2H^+ + 2e^-$ (dehydration steps) (3.1b)

$HCOOH + M(1)^0 \rightarrow M(1)\text{-}CO_{ad} + H_2O$ (3.1b, i)

$M(2)^0 + H_2O \rightarrow M(2)\text{-}OH_{ad} + H^+ + e^-$ (3.1b, ii)

$M(1)\text{-}CO_{ad} + M(2)\text{-}OH_{ad} \rightarrow M(1)^0 + M(2)^0 + CO_2 + H^+ + e^-$ (3.1b, iii)

As shown in Equation 3.1b, CO adsorption is an important mechanistic step during the FAO. Thus transition metal based catalysts could play a key role in enhancing the rate of reaction extensively that involves the adsorption of CO and OH moiety (Equation 3.1b, i and 3.1b, ii), diffusion and bond dissociation steps of CO_{ad} (Equation 3.1b, iii) as demonstrated in the literature.[14,15]

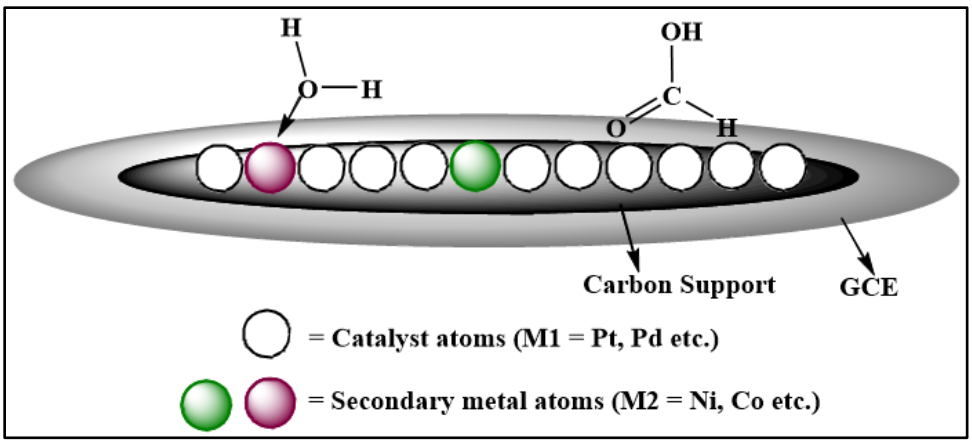

Figure 3.1 Bifunctional effect on FAO mechanism.

Other than Pt and Pd, several other metals or metal combinations have been employed as anode catalysts. The addition of the second elements to Pt or Pd results in the increase in electrocatalytic activity for formic acid oxidation via bifunctional mechanism and electronic effect (Figure 3.1).[9] The composite catalysts could lower the CO poisoning, and hence increase the efficiency towards FAO.[4,5,11,27,36-40,44,58-62] These attempts, however, have not effectively solved the CO poisoning problem.[66] The high cost of these catalysts is also a concern for the commercialization of the DFAFCs.[4,5]

Pure metal- or alloy- based catalysts under the fuel cell operation conditions cannot avoid the inevitable dissolution in HCOOH over the potential window of interest.[67,68] The development of advanced catalyst supporting materials, especially nanostructured carbon supports have been a promising way to improve the activity and stability of fuel cell electrocatalysts.[4] Carbon-based materials especially carbon black have been widely used due to their good electrical conductivity, chemical stability, and low cost. However, carbon black is essentially nonporous with a low surface area, resulting in low utilization of expensive precious catalysts. Multi-walled carbon

nanotubes (MWCNTs)[29,49-51,53,54,69-71] and graphene,[40,72,73] on the other hand, have proved to be potential catalyst support materials for fuel cell applications, owing to their good conductivities, large surface areas, stable and durable mechanical and thermal properties. Very recently, transition metal oxides based semiconducting materials have been reported to be effective supports.[58,71,72,74-83] Nevertheless, as anodic catalyst supports in DFAFCs, their chemical and electrochemical stabilities are questionable because these oxides could react with formic acid or could be reduced at the electrode.

Table 3.1

Surface properties of the nanostructured carbon supports.

Materials	Activated Carbon	Graphite Nanoparticles	Ketjen Black EC600	Vulcan XC-72
Surface area, m^2/g	~500	660 - 720	1400	232
Particle size, nm	N/A	~10	N/A	~30 - 50

Note: Data were collected from manufacturers.

Herein, we report the extensive comparison results of formic acid electrooxidation with 20 wt% Pd/C and novel 10 wt% PdNiCo/C nanocatalysts, where C indicates Vulcan XC-72 (VXC), Ketjen Black EC600 (KBE), graphite nanoparticles (GNP), and activated carbon. These support materials, as listed in Table 3.1, vary in surface area and particle size. Therefore, their catalytic activity towards formic acid oxidation could be different. To decrease the use of precious metal Pd, earth-abundant metals, *i.e.,* Ni and Co, were selected to prepare the ternary nanocomposites with half the amount of Pd on the nanocarbon supports. Previously, both Ni and Co based bimetallic catalysts have been tested for DFAFCs.[44,45,54,55,126] However, to our best knowledge, NiCo combination with Pd towards FAO has not been reported. Consequently, studies presented in this chapter

could provide significant insight on how to choose suitable carbon supports and use alternative metals to effectively catalyze formic acid oxidation.

3.2 Experimental Section

3.2.1 Chemicals

All starting materials, carbon supports, and electrolytes are commercially available and were used as received. From Sigma-Aldrich, $PdCl_2$ (99%), $NiCl_2 \cdot 6H_2O$ (≥99.9%) and Nafion perfluorinated resin solution (Nafion®, 5 wt% in 2-propanol, *n*-propanol; 15-20% water) were purchased. $CoCl_2 \cdot 6H_2O$ (≥99.9%) was purchased from Alfa Aesar. $NaBH_4$ (≥99%) and HCOOH (50%, HPLC Grade) were purchased from Fluka Analytical. H_2SO_4 (Certified ACS Plus, 95.0 - 98.0 w/w%) and $HClO_4$ (ACS reagent grade, 70.0 w/w%) were obtained from Fisher Scientific. Graphite nanoparticles (GNP) (~10 nm) were purchased from ACS Materials. Vulcan XC-72 (VXC) and Ketjen Black EC600 (KBE) were obtained from Cabot Corp. and Azko Nobel Surface Chemicals LLC, respectively. CO gas (Research grade, 99.99%) and ultrapure N_2 were procured from Airgas, Inc.

3.2.2 Syntheses of Pd/C and PdNiCo/C

The metal ion precursors were anhydrous $PdCl_2$, $NiCl_2 \cdot 6H_2O$, and $CoCl_2 \cdot 6H_2O$. To prepare the 20 wt% catalysts, anhydrous $PdCl_2$ (20.0 mg, 0.113 mmol) was dissolved in 3.13 mL 0.10 M HCl using ultrasonication. 60 mg Vulcan XC-72 carbon was mixed with the $PdCl_2$ solution and 6.87 mL DI water was added to make the final volume of the mixture to 10.00 mL. The suspension obtained was ultrasonicated for 30 min and stirred for 4 h. The pH of the suspension was adjusted to ~9 with few drops of concentrated Na_2CO_3 solution. 20.00 mL of $NaBH_4$ (52.9 mg, 1.4 mmol) solution was then delivered

into the above mixture as reducing agent with a mini-flow variable-speed pump (VWR International) and further stirred for 2 h. Subsequently, the mixture was filtered, washed several times with DI water to remove any excess reagents and dried in a vacuum oven at 60 °C for 12 h. The 20.0 wt% Pd/C was then collected and stored inside a desiccator. Similarly, 10 wt% PdNiCo/C nanocomposite catalysts were prepared using half the amount of Pd^{2+} mixed with Ni^{2+} and Co^{2+} in a 1:1:1 (Pd:Ni:Co) mass ratio in the same solution utilizing respective carbon supports.

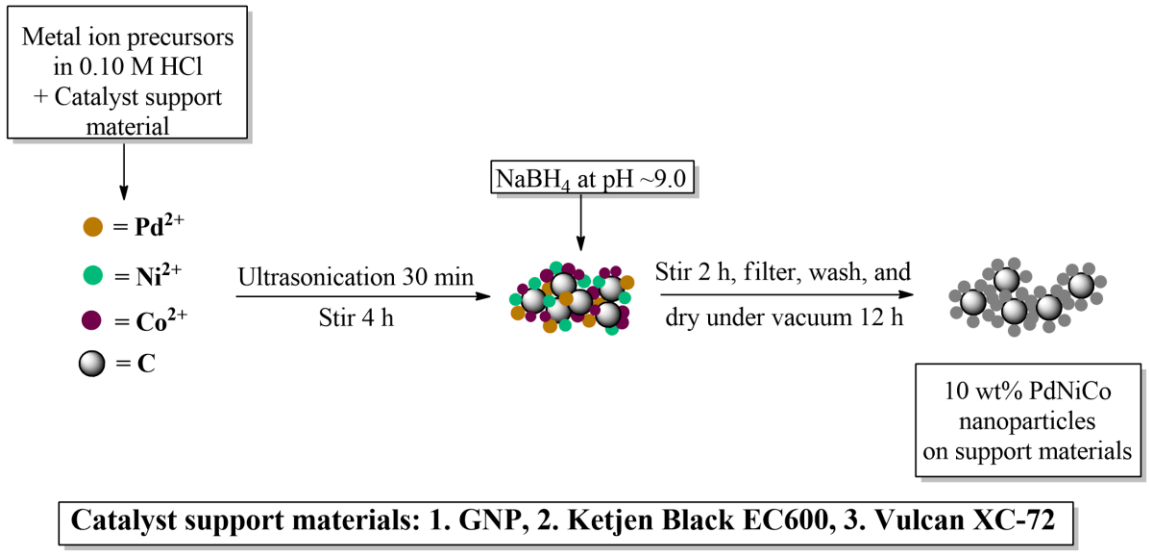

Figure 3.2 One pot synthesis scheme of carbon-supported nanomaterials.

Consequently, six different batches of catalysts (20 wt% Pd/C and 10 wt% PdNiCo/C) with (a) GNP (Pd/GNP and PdNiCo/GNP), (b) Ketjen Black EC600 (Pd/KBE and PdNiCo/KBE), and (c) Vulcan XC-72 (Pd/VXC and PdNiCo/VXC) support materials were prepared following the one pot synthesis strategy (Figure 3.2) from literature with modifications.[17]

3.2.3 Characterization

The morphology of the synthesized Pd/VXC, Pd/KBE, Pd/GNP, PdNiCo/VXC, PdNiCo/KBE, and PdNiCo/GNP were analyzed using scanning electron microscopy (SEM, Zeiss Sigma VP) and the compositions were studied utilizing electron dispersive X-ray spectroscopy (EDX) on SEM using the Thermo Scientific UltraDry EDS Detector with NSS 3 microanalysis software. The elemental mapping with spectrum imaging of the composites (PdNiCo/VXC, PdNiCo/KBE, and PdNiCo/GNP) were obtained from the same EDS instrument. The samples were prepared by dispersing using ultrasonication in ethanol and casting on Si wafer, drying in air followed by Ag-sputtering.

3.2.4 GCE Modification and Electrochemical Studies

Unless otherwise stated, for all cyclic voltammetry (CV), multi-potential chronoamperometry (CA) and CO stripping voltammetry (COSV) measurements, a three-electrode electrochemical cell coupled with a CHI 900B computerized potentiostat system (CH Instrument, Austin, TX, USA) was used at room temperature (24±1 °C). The three electrodes were (a) catalyst-modified glassy carbon (3 mm diameter) disk working electrode (GCE), (b) mercury/mercury sulfate [MSE, Hg/Hg_2SO_4 (satd. K_2SO_4)] reference electrode, and (c) Pt mesh counter electrode. Before each electrochemical experiment, the working electrode was cleaned and modified with a thin-film of the catalysts using the procedure described in Chapter I (Section 1.7.1.1). The catalytic load was 0.025 mg of metal(s)/cm^2 of GCE for CV and CA experiments. For COSV experiments, 0.100 mg of metal(s)/cm^2 of GCE load was maintained.

The CV responses for FAO were measured with the electrochemical workstation using 2.00 mL solution containing 0.50 M HCOOH and 0.10 M H_2SO_4 from -0.60 to

+0.50 V vs. Hg/Hg_2SO_4 (satd. K_2SO_4) at a scan rate of 20.0 mV/s with a freshly coated thin-film of nanocatalysts on GCE after the electrolytes were deaerated with high purity N_2 gas for 15 min and under N_2 atmosphere. Multi-pulse CA and COSV experiments were performed following the protocol stated in Chapter I (Section 1.7.3.2). The long-term durability, catalytic activity, anti-CO poisoning characteristic, and the ECSA (cm^2) for the nanocatalysts were compared with the commercial 20 wt% Pd/C (activated carbon).

3.3 Results and Discussion

3.3.1 Characterization of the Prepared Catalysts

Figures 3.3 a – d show the SEM images of Pd catalysts on the carbon support of activated carbon, GNP, Ketjen Black (KBE), and Vulcan XC-72 (VXC), respectively. All particles have nanoflower shape with diameters of 10-20 nm. Additionally, the particles of the commercial Pd/C and Pd/GNP (Figures 3.3 a and b) are more aggregated as compared to those of Pd/KBE and Pd/VXC (Figures 3.3 c and d).

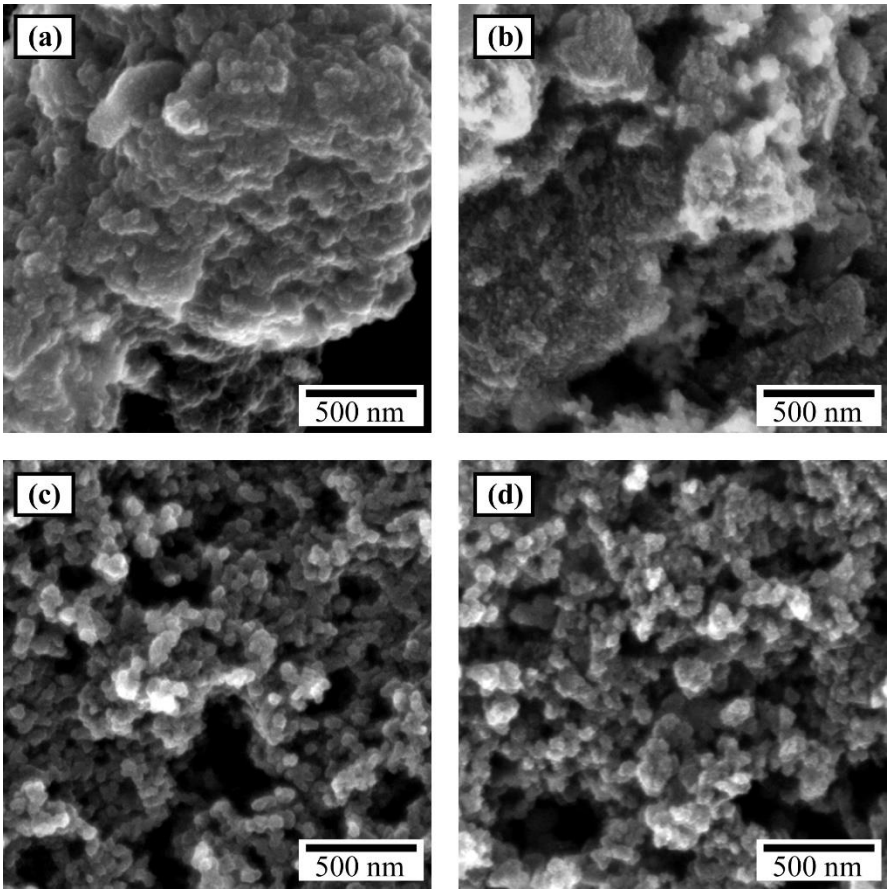

Figure 3.3 SEM images of (a) Pd/C, (b) Pd/GNP, (c) Pd/KBE, and (d) Pd/VXC.

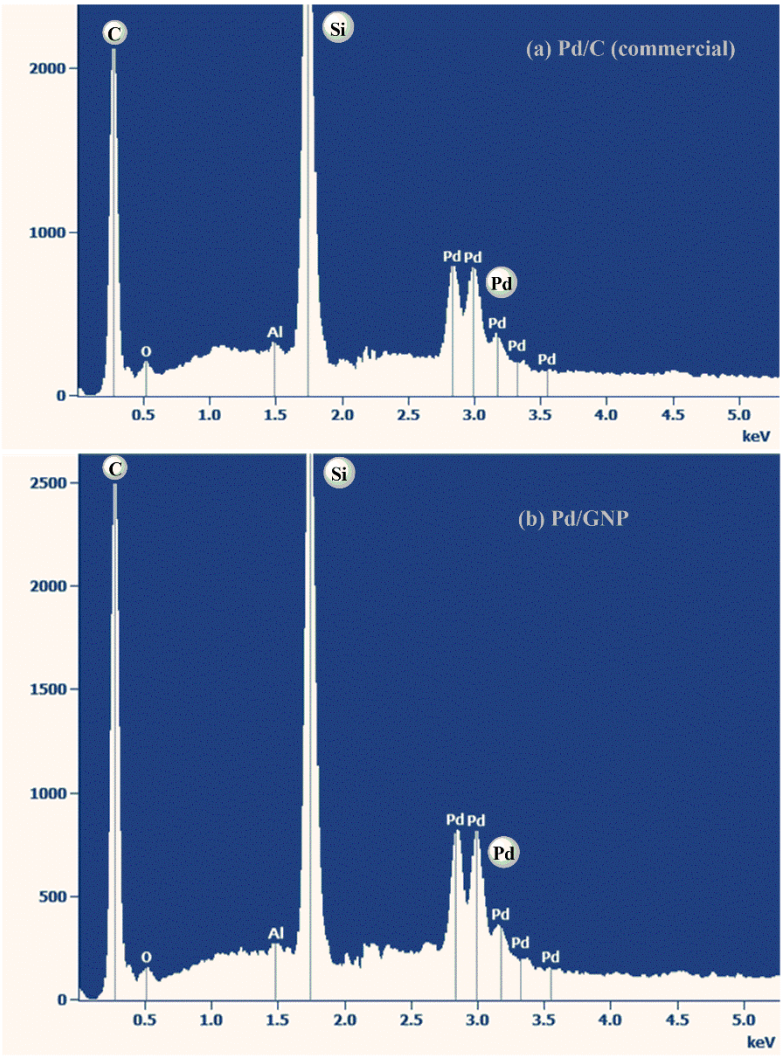
(a) Pd/C (commercial)
C
Si
O
Al
Pd
2000
1000
0
0.5
1.0
1.5
2.0
2.5
3.0
3.5
4.0
4.5
5.0
keV
(b) Pd/GNP
2500
1500
500

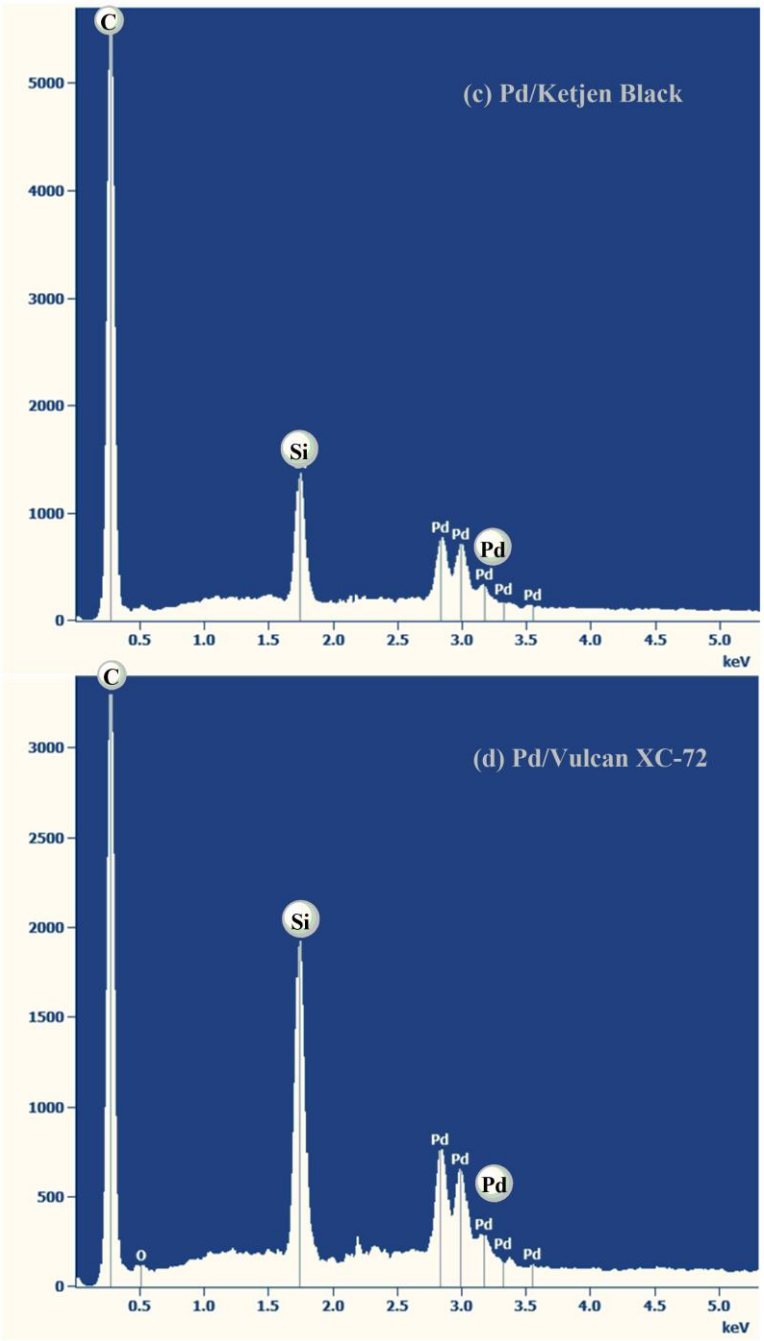

Figure 3.4 EDX of (a) Pd/C, (b) Pd/GNP, (c) Pd/KBE, and (d) Pd/VXC.

EDX data shown in Figure 3.4 confirm the formation of Pd catalyst on carbon support, in which Si and Al signals are from Si wafer and Al stub used to hold Pd nanocalatysts. The EDX spectra also provide a good estimation of the elemental

composition and their weight% of the catalysts, which are listed in Table 3.2. For the prepared Pd/C catalysts, the weight % ratio of Pd to C ranges from 11 – 15% which is in close proximity to the commercial Pd/C (~16%).

Table 3.2

Elemental composition of Pd/C, Pd/GNP, Pd/KBE, and Pd/VXC.

Weight %	C	Pd	Si	O	Al
Pd/C	63.24±0.85	10.10±0.61	22.25±0.17	4.09±0.62	0.32±0.06
Pd/GNP	70.27±0.90	8.49±0.62	19.33±0.16	1.55±0.59	0.36±0.06
Pd/KBE	82.73±0.77	9.16±0.54	8.10±0.08	-	-
Pd/VXC	74.54±0.73	11.55±0.60	13.30±0.11	0.61±0.62	-

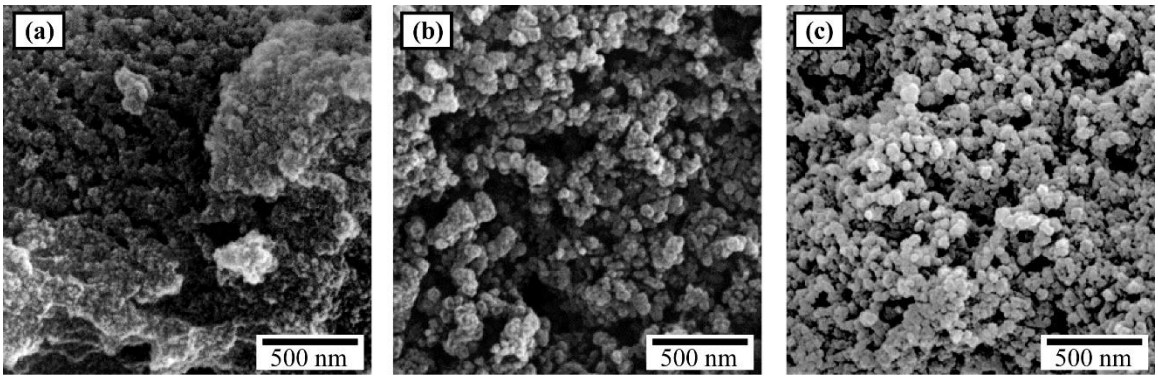

Figure 3.5 SEM images of (a) PdNiCo/GNP, (b) PdNiCo/KBE, and (c) PdNiCo/VXC.

Figure 3.5 displays the nanoflower shape morphology with a size distribution of ~10 nm for the ternary nanocomposites of PdNiCo on different carbon supports. Although the GNP-based catalysts are agglomerated as bigger lumps, individual particles are still within the same size region (Figure 3.5a).

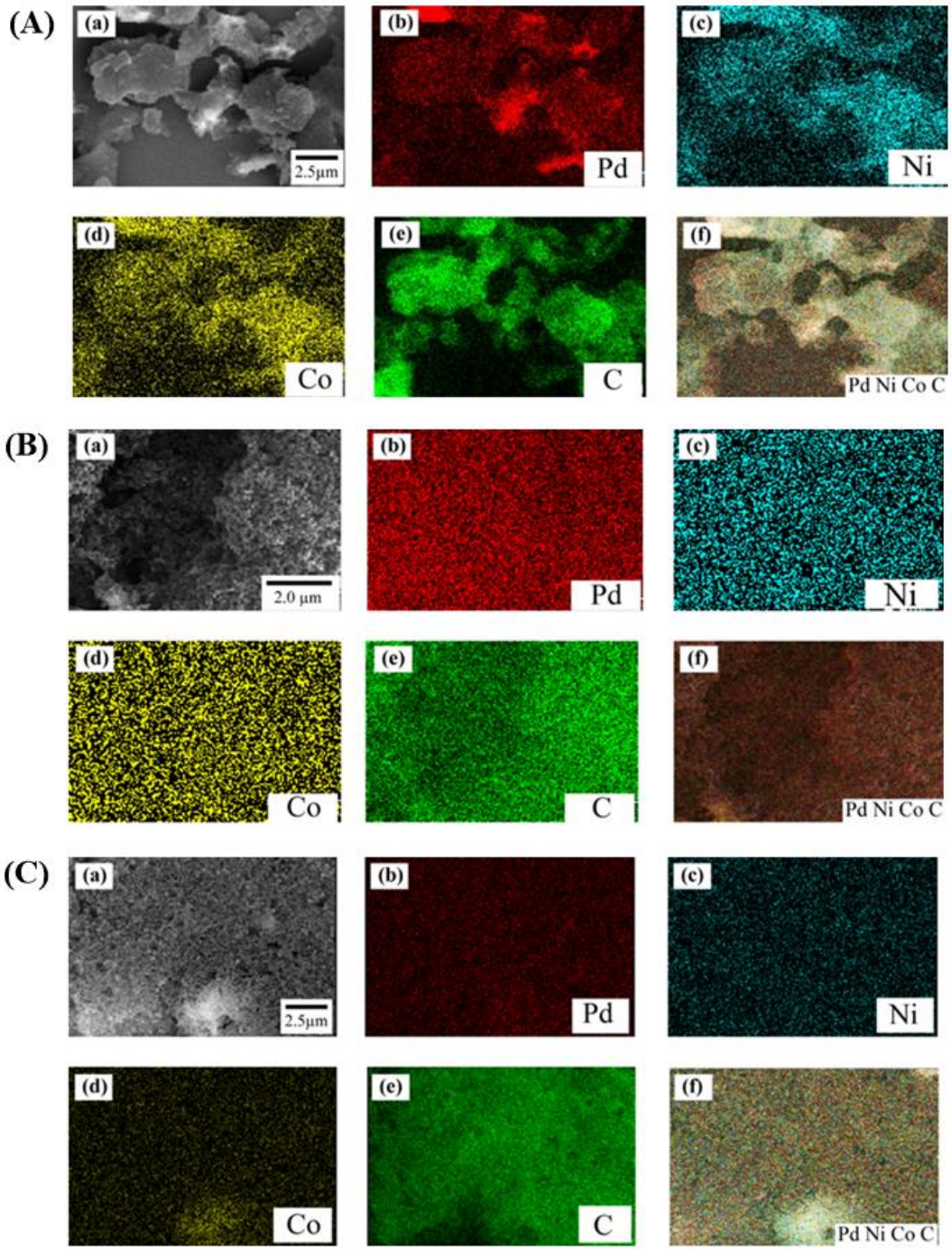

Figure 3.6 EDX mapping spectra of (A) PdNiCo/GNP, (B) PdNiCo/KBE, and (C) PdNiCo/VXC.

Note: (a) SEM images; (b) – (e) EDX mapping images of Pd, Ni, Co and C, respectively; and (f) integrated (overlay) EDX mapping images of (b) to (e).

The EDX mapping images clearly show that the metal nanoparticles (Pd, Ni and Co) are well-dispersed on the carbon support materials (Figure 3.6). Both Si and Ag are detected as background elements and discarded from the images.

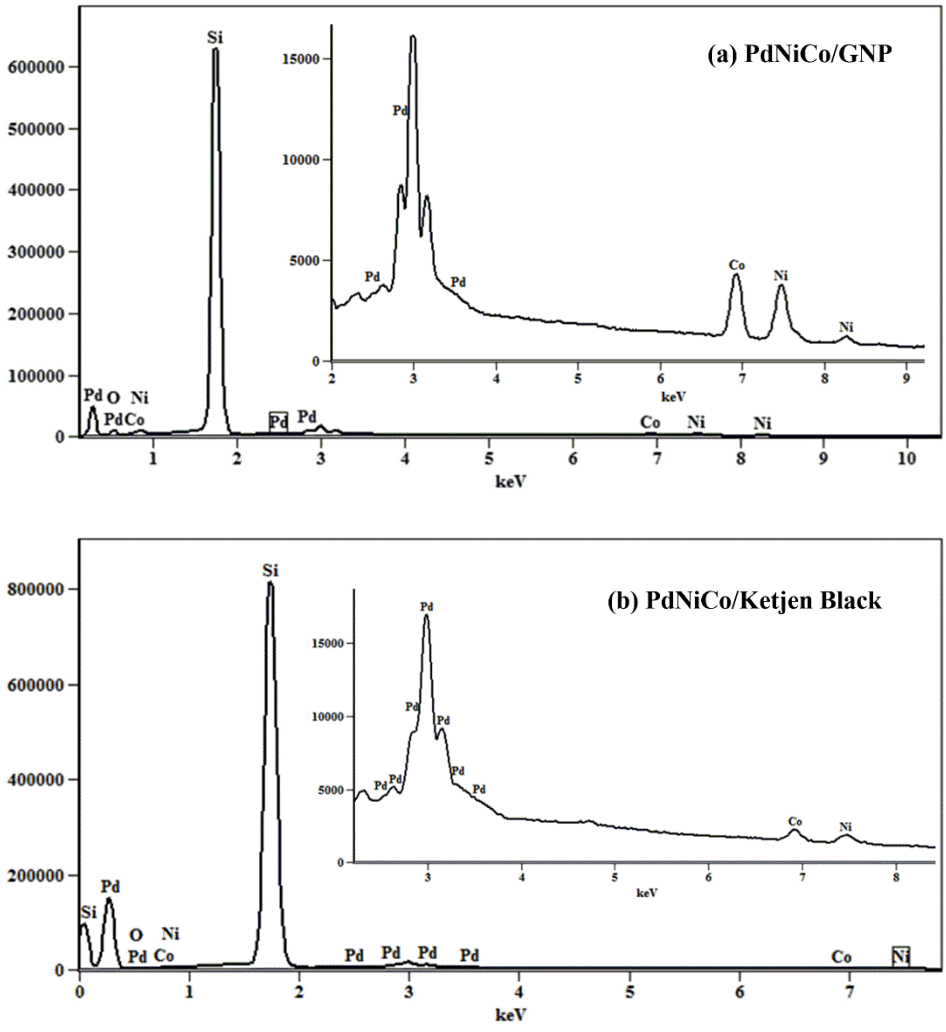

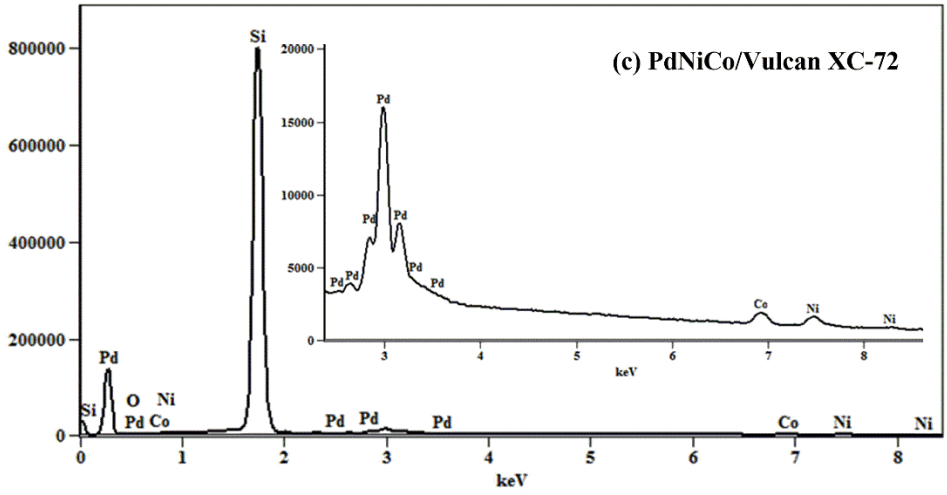

Figure 3.7 EDX spectra of (a) PdNiCo/GNP, (b) PdNiCo/KBE, and (c) PdNiCo/VXC.

The elemental compositions measured from EDX spectra are shown in Table 3.3 for all the synthesized ternary catalysts. The spectra (Figure 3.7) also confirm that the catalysts were prepared without any notable contaminations.

Table 3.3

Elemental composition of (a) PdNiCo/GNP, (b) PdNiCo/KBE, and (c) PdNiCo/VXC.

Weight %	C	Pd	Ni	Co	Si	O	Ag
PdNiCo/GNP	31.23 ±0.17	2.12 ±0.04	1.93 ±0.03	1.89 ±0.03	53.25 ±0.17	4.59 ±0.05	4.99 ±0.05
PdNiCo/KBE	56.16 ±0.24	0.91 ±0.01	0.23 ±0.02	0.25 ±0.02	39.69 ±0.13	-	2.76 ±0.03
PdNiCo/VXC	51.38 ±0.54	0.95 ±0.03	0.32 ±0.02	0.37 ±0.02	42.48 ±0.14	0.85 ±0.03	3.29 ±0.03

The weight% ratio of Pd:Ni:Co on GNP, KBE, and VXC has an approximate value of 1:1:1, 4:1:1, and 3:1:1, respectively. Note that the above values are obtained from micro-sized sample surfaces, and they may not well represent the real compositions of the bulk samples that are used for the following studies.

3.3.2 Electrochemical Characterization

3.3.2.1 FAO Activity and Stability: CV and CA Studies

The FAO activities of the synthesized catalysts were investigated and compared with those obtained from the commercially available 20.0 wt% Pd/C (Pd/C) using a constant catalytic load of 0.025 mg of metal/cm^2 of GCE. As shown in Figure 3.8, Pd/VXC has a FAO peak current of 2.34 mA on the forward scan (Figure 3.8d), which is 2.5 times of that 0.94 mA obtained from Pd/C (Figure 3.8b). This finding could be attributed to the smaller particle size hence larger surface area and better catalytic dispersion of Vulcan XC-72 as compared with activated carbon (Figure 3.3d vs. 3.3a). On the other hand, similar peak current values of FAO on Pd/KBE (0.80 mA, Figure 3.8a), Pd/GNP (1.17 mA, Figure 3.8c), and Pd/C (0.94 mA, Figure 3.8b) are evident, although SEM images of those three catalysts have shown quite different morphologies (Figure 3.3). The above data suggests that the surface area of a carbon support is not the only factor affecting catalytic activities. Instead, the number of active catalyst particles on the electrode surface may play an even more important role in determining the catalytic reactions effectiveness. For example, Ketjen Black has the largest surface area among all presently studied carbon supports (Table 3.1), but its porous morphology could have made fewer metal particles available on the surface as compared with those on Vulcan XC-72. Whereas, GNP itself is small in size but the aggregated morphology of Pd/GNP as shown in the SEM images results in less active towards FAO as compared with Pd/VXC. Similar trends were observed in the case of the PdNiCo composites (Figure 3.8B), namely PdNiCo/VXC (1.03 mA), PdNiCo/GNP (0.36 mA), and PdNiCo/KBE (0.48 mA), where the specific load of Pd was 0.5 times of that of all the monocatalysts

discussed earlier. Addition of second or third metals is known to enhance the FAO activity by bifunctional effect and modifying the *d*-band center of Pd, which can lead to a weaker Pd-CO bond facilitating the direct FAO pathway.[9] Hence, peak potential shift towards negative direction on the CV is expected as illustrated in Figure 3.8, indicating a greater catalytic activity.

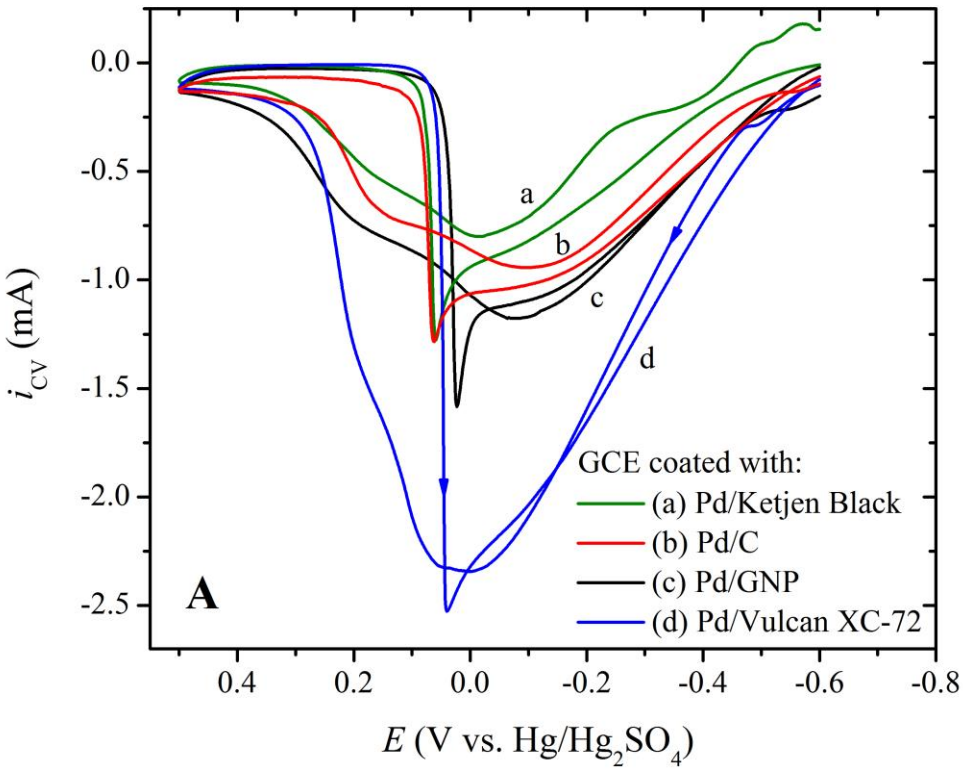

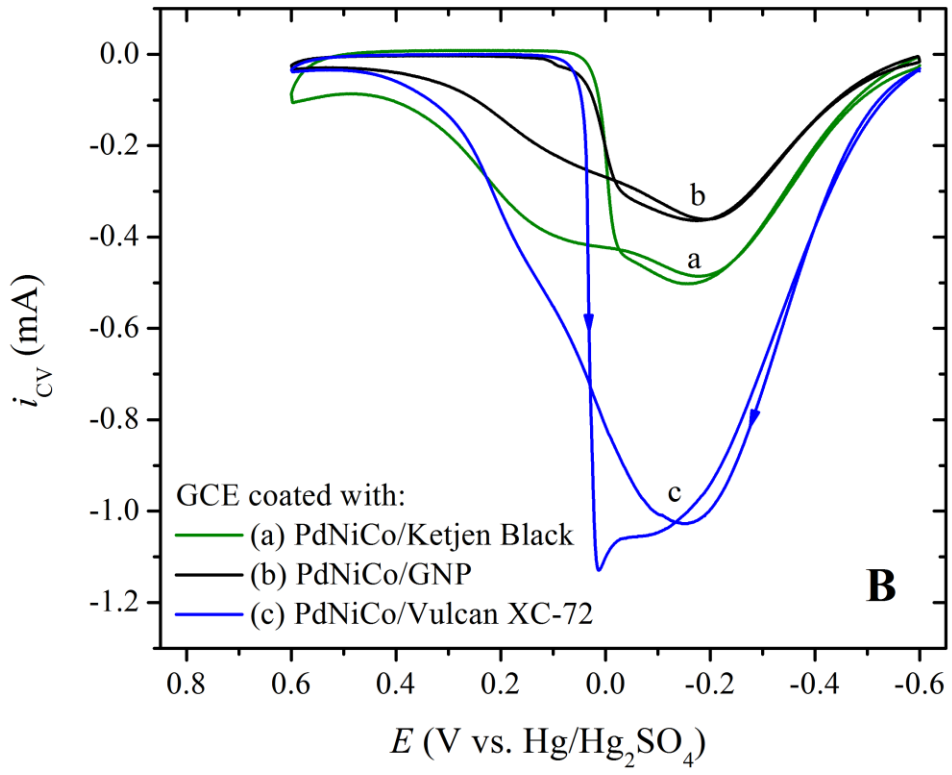

Figure 3.8 Cyclic voltammograms of FAO at prepared and commercial catalysts.

Note: CV signals of 0.50 M HCOOH with 0.10 M H_2SO_4 using the constant catalytic load of 0.025 mg of metal/cm^2 GCE coated with (A) 20 wt% Pd/C, (B) 10 wt% PdNiCo/C at a scan rate of 20.0 mV/s.

Table 3.4 illustrates the specific oxidation peak potentials on the forward scans of all the catalysts. The ternary composites demonstrated an average potential shift of -142.6 mV vs. the synthesized monocatalysts and -85.5 mV vs. the commercial 20% Pd/C. These data verify the superior FAO activities of the ternary composite catalysts.

Table 3.4

Comparison of FAO peak potential shifts.

Carbon based support materials	Peak potential, *E*/V (vs. Hg/Hg_2SO_4) for 20% Pd/C	Peak potential, *E*/V (vs. Hg/Hg_2SO_4) for 10% PdNiCo/C	Potential shift vs. prepared 20% Pd/C, mV	Potential shift vs. commercial 20% Pd/C, mV	Average potential shift
Vulcan XC-72	0.0135	-0.1554	-141.9	-62.7	-142.6 mV vs. prepared 20% Pd/C
GNP	-0.0796	-0.1989	-119.3	-106.2	
Ketjen Black	-0.0136	-0.1802	-166.6	-87.5	-85.5 mV vs. commercial 20% Pd/C
Commercial	-0.0927	-	-	-	

Note: The average potential shifts showing the superior catalytic activity of the prepared catalysts, specially the PdNiCo nanocomposites compared with the commercial 20 wt% Pd/C.

Chronoamperometry (CA) curves of Pd/GNP, Pd/KBE, and Pd/VXC were compared with Pd/C at -0.20 V vs. Hg/Hg_2SO_4 over a period of 1200 s to evaluate the stability. As shown in Figure 3.9, all currents of FAO decay over time. Specifically, Pd/KBE shows ~95.00% current decay (Figure 3.9a), which could be attributed to the porous nature of the support material so relatively less active catalytic sites are present on the surface. Whereas, the rest of the materials show similar behavior (Figures 3.9b-d). Much larger FAO current on Pd/VXC (Figure 3.9d) over the entire period of time is consistent with the CV data discussed earlier, indicating that this type of catalyst is relatively stable with a high efficiency (Table 3.5).

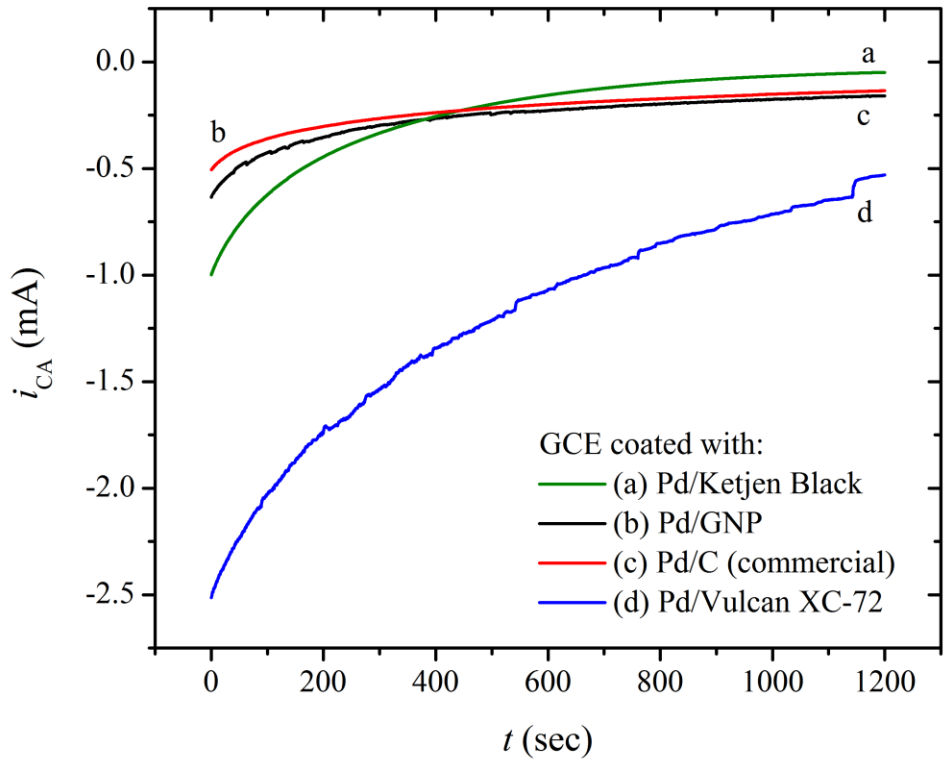

Figure 3.9 Chronoamperometry results.

Note: CA responses of prepared 20 wt% Pd/C vs. commercial 20 wt% Pd/C at -0.2 V vs. Hg/Hg_2SO_4 for 1200 sec.

To better understand and compare the stability of all the above catalysts over a longer period of time, multi-pulse chronoamperometry technique was exploited. The pulse was stepped between E_1 and E_2 that were chosen based on the CV responses of FAO as shown in Figure 3.8. At E_1 (-0.60 V vs. Hg/Hg_2SO_4), there is no FAO activity and at E_2 (0.10 V vs. Hg/Hg_2SO_4), direct oxidation of formic acid takes place. Thus, by pulsing between these two potential steps with a pulse width of 2 s for ~4000 cycles, the % current change was assessed for all the nanomaterials vs. the commercial Pd/C (Table 3.5).

Table 3.5

Comparison of the % FAO current decays.

Nanocatalysts	% Change (after 1200 sec) (CA)	% Change (after 4.27 h) (Pulsing)
20% Pd/Vulcan XC-72	-78.94	-58.11
20% Pd/GNP	-74.65	-54.78
20% Pd/Ketjen Black	-95.00	-41.93
10% PdNiCo/Vulcan XC-72	-	-95.84
10% PdNiCo/GNP	-	-91.72
10% PdNiCo/Ketjen Black	-	-73.80
20% Pd/C (commercial)	-74.84	-91.74

Note: From CAs and multi-pulse CA results, % current changes were calculated using Equation 1.6.

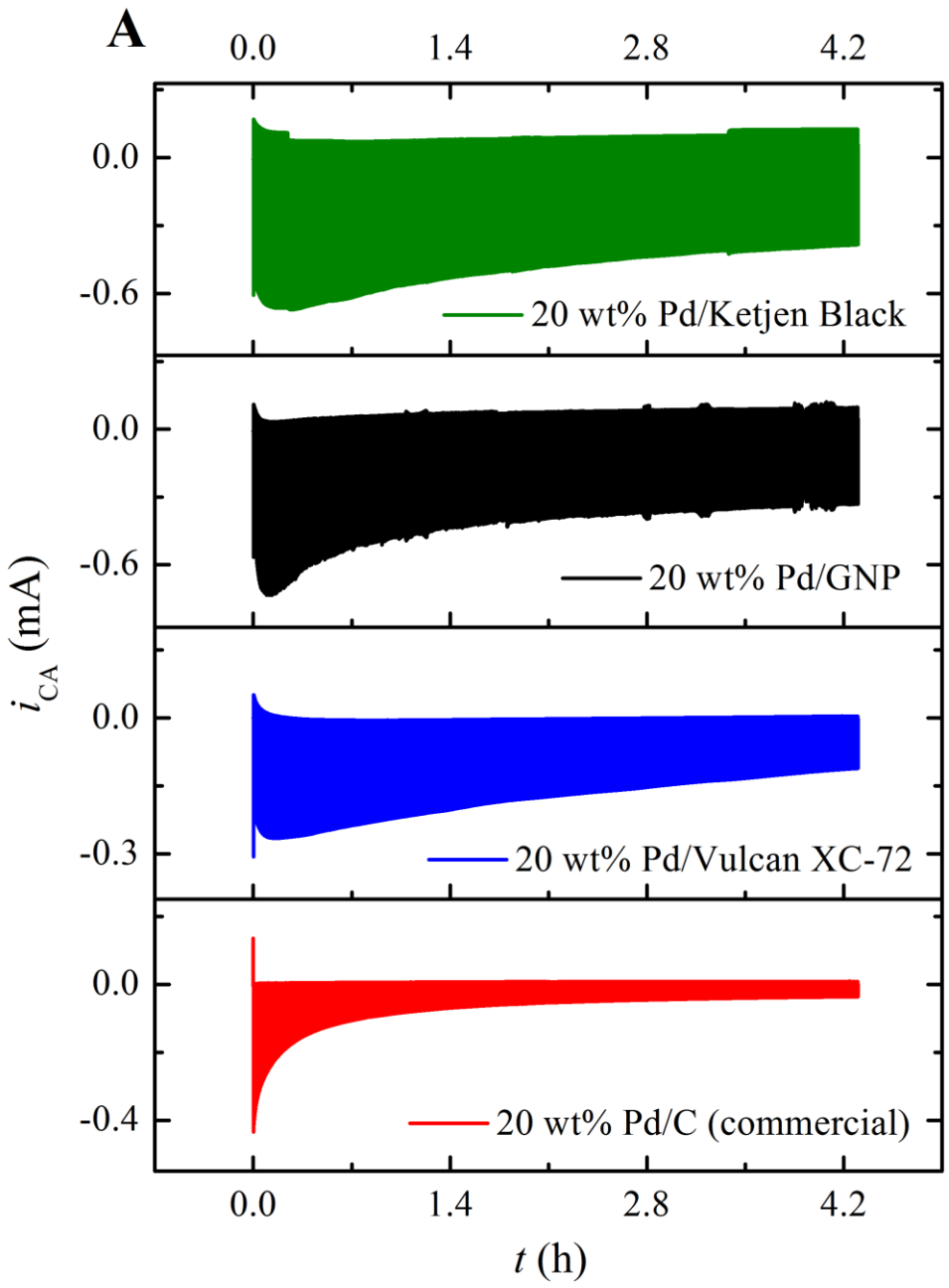
A
0.0
1.4
2.8
4.2
0.0
-0.6
20 wt% Pd/Ketjen Black
0.0
-0.6
20 wt% Pd/GNP
0.0
-0.3
20 wt% Pd/Vulcan XC-72
0.0
-0.4
20 wt% Pd/C (commercial)
i_{CA} (mA)
t (h)

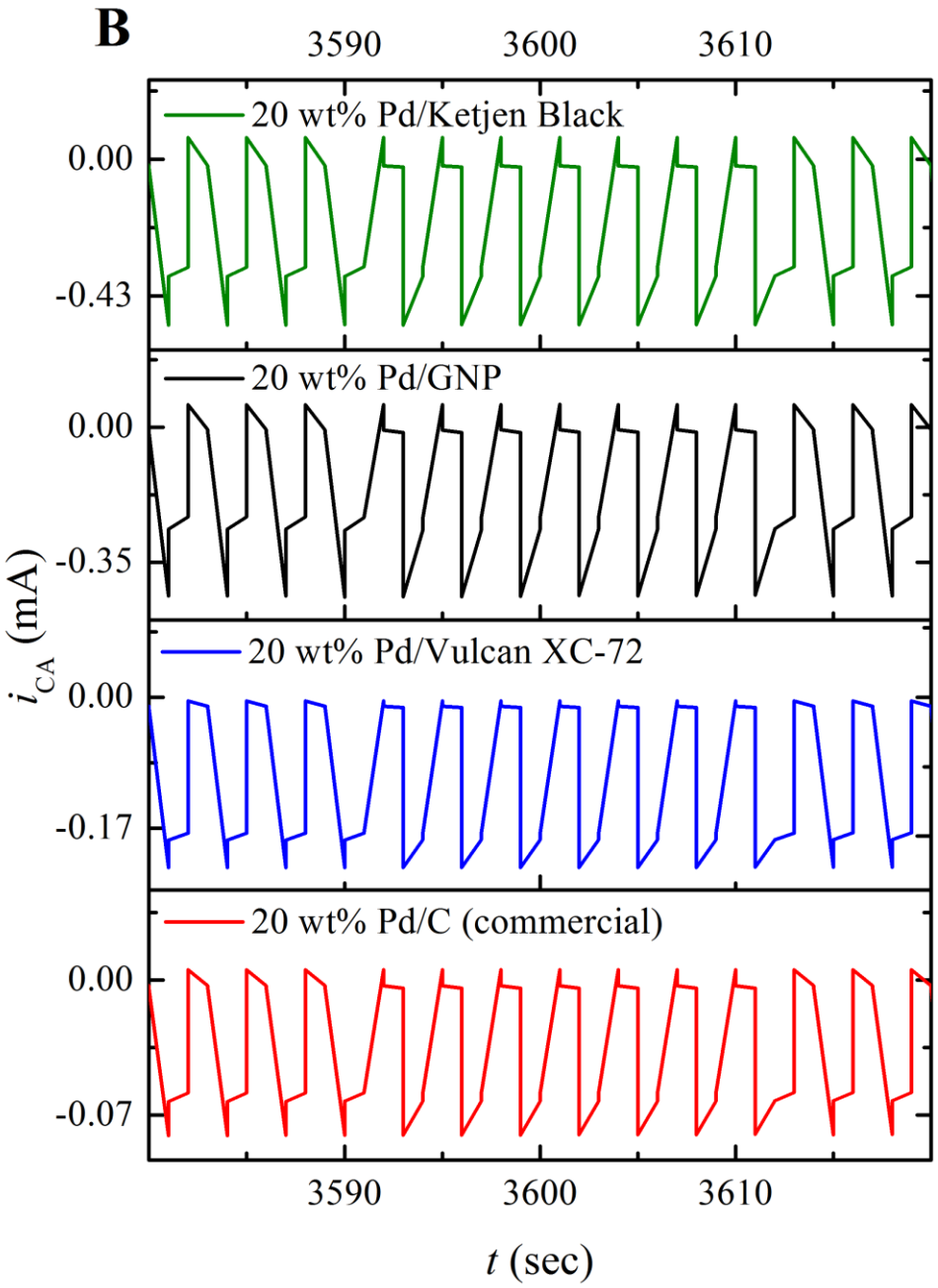

Figure 3.10 Multi-pulse chronoamperometry curves of 20% Pd/C batches.

Note: Pulse CA signals of (A) prepared 20 wt% Pd/C vs. commercial 20 wt% Pd/C for ~4000 step cycles (4.27 h) between 0.1 and -0.6 V vs. Hg/Hg_2SO_4, (B) Close-up around 3600 sec (1 h).

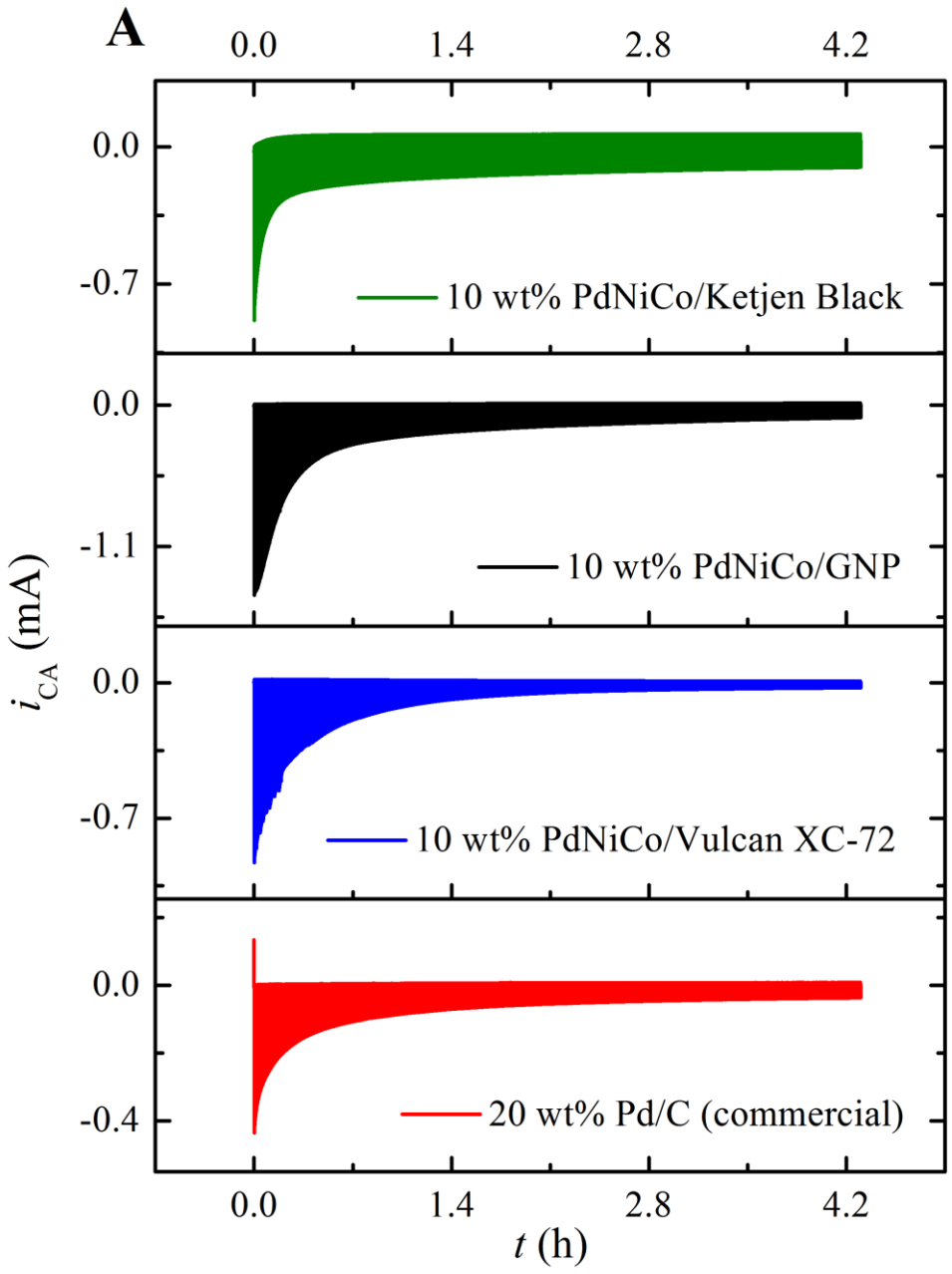
A
0.0
1.4
2.8
4.2
0.0
-0.7
10 wt% PdNiCo/Ketjen Black
0.0
-1.1
10 wt% PdNiCo/GNP
0.0
-0.7
10 wt% PdNiCo/Vulcan XC-72
0.0
-0.4
20 wt% Pd/C (commercial)
i_{CA} (mA)
t (h)

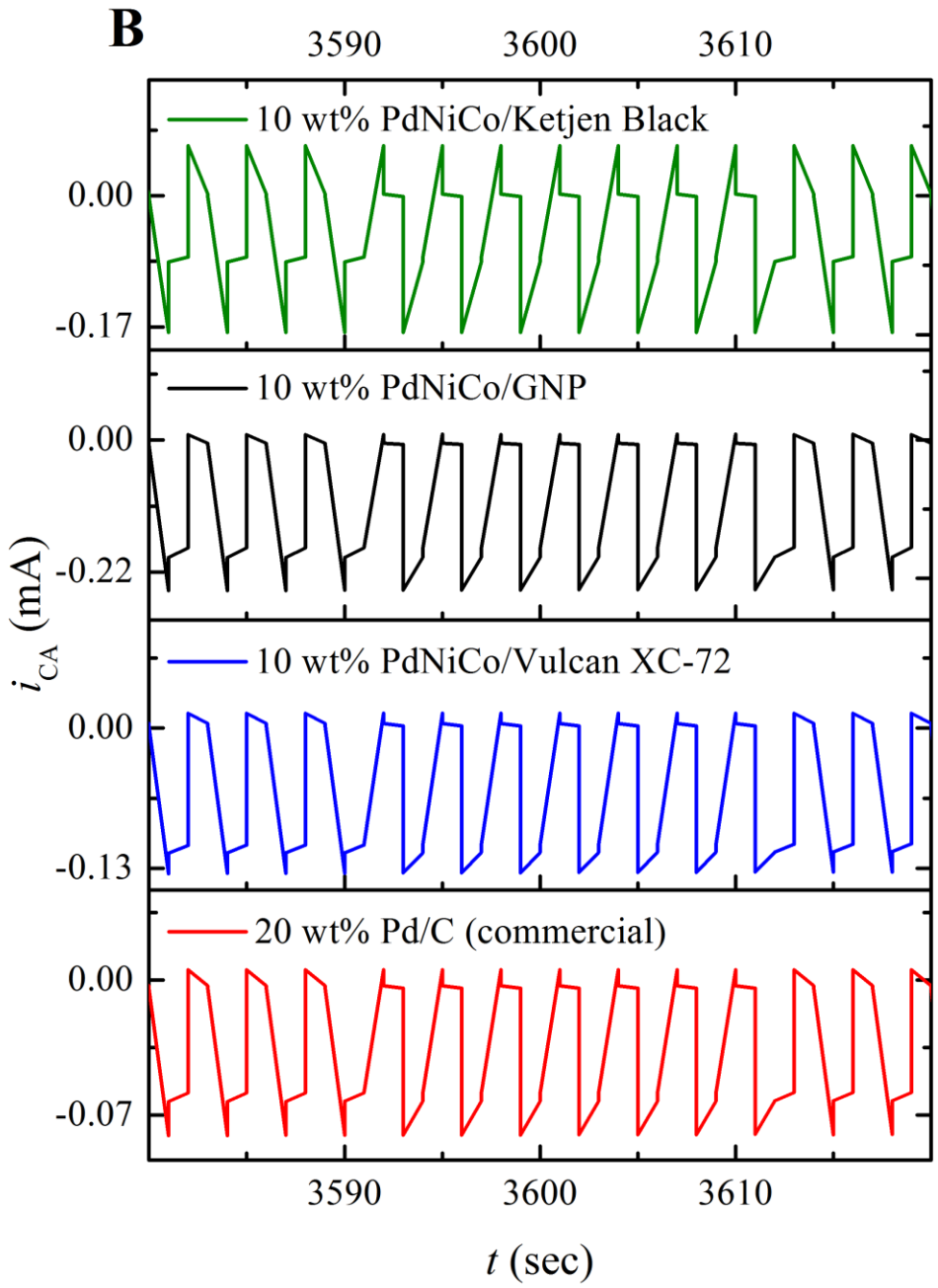

Figure 3.11 Multi-pulse chronoamperometry curves of 10% PdNiCo/C composites.

Note: Pulse CAs of (A) prepared 10 wt% PdNiCo/C vs. commercial 20 wt% Pd/C for ~4000 step cycles (4.27 h) between 0.1 and -0.6 V vs. Hg/Hg_2SO_4, (B) Close-up around 3600 sec.

Figures 3.10 and 3.11 show the overall profiles of multi-pulse CA for 4.27 h and close-up images around 3600 s (1 h). Over a longer period of time, Ketjen Black supported catalysts were highly stable probably because the nanometal materials adsorbed on porous Ketjen Black have a less leaching and CO poisoning rate and a high surface regeneration capabilities under the experimental conditions. Except for PdNiCo/VXC, all other catalysts are more stable than the commercial Pd/C. Furthermore, all three PdNiCo ternary nanocatalysts show much less stability than Pd on their corresponding carbon supports. Relatively high dissolution rate of Ni and Co could be responsible for the above observation.

Finally, 10% PdNiCo ternary catalysts on both Vulcan XC-72 and GNP are almost as stable as 20% Pd/C. Their prolonged durability should be utilized to save precious Pd metal, not to mention that all ternary catalysts have shown high catalytic activity towards FAO. The use of Ketjen Black as support material and earth-abundant metals like Ni and Co with a lower amount of precious metals could lead to the production of cost effective and highly efficient anodic catalysts for FAO.

3.3.2.2 CO Oxidation and ECSA Estimation: COSV Data

CO-stripping voltammetry (COSV) technique was pivotal to investigate anti-CO poisoning activities of the nanomaterials and for the estimation of electrochemical active surface area (ECSA). The CO-stripping signals were collected after pre-adsorbing a monolayer of CO on the electrode surface. The second sweep signals were used to verify if CO was completely desorbed from the catalyst surface and to obtain the baseline corrected CO-stripping peaks. The CO-stripping charge, Q_{meas} (in Coulomb, C) was

determined by integrating the area under the CO-stripping peaks. Finally, ECSAs were calculated using Equation 1.11.

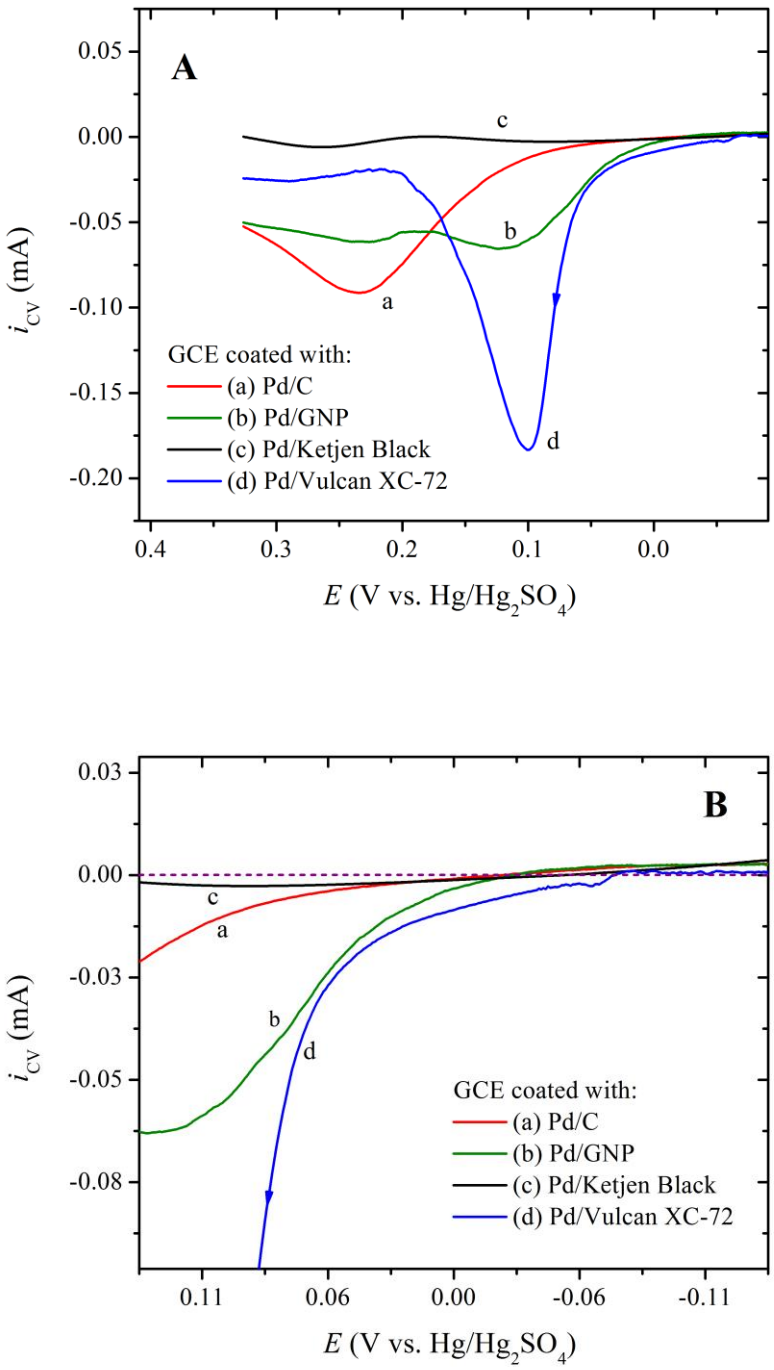

Figure 3.12 CO-stripping voltammograms of 20% Pd/C.

Note: COSVs of (A) prepared 20 wt% Pd/C vs. commercial 20 wt% Pd/C in 0.10 M $HClO_4$ at a scan rate of 20.0 mV/s. CO was preadsorbed at -0.54 V vs. Hg/Hg_2SO_4 for 20 min followed by N_2 purging. (B) Close-up.

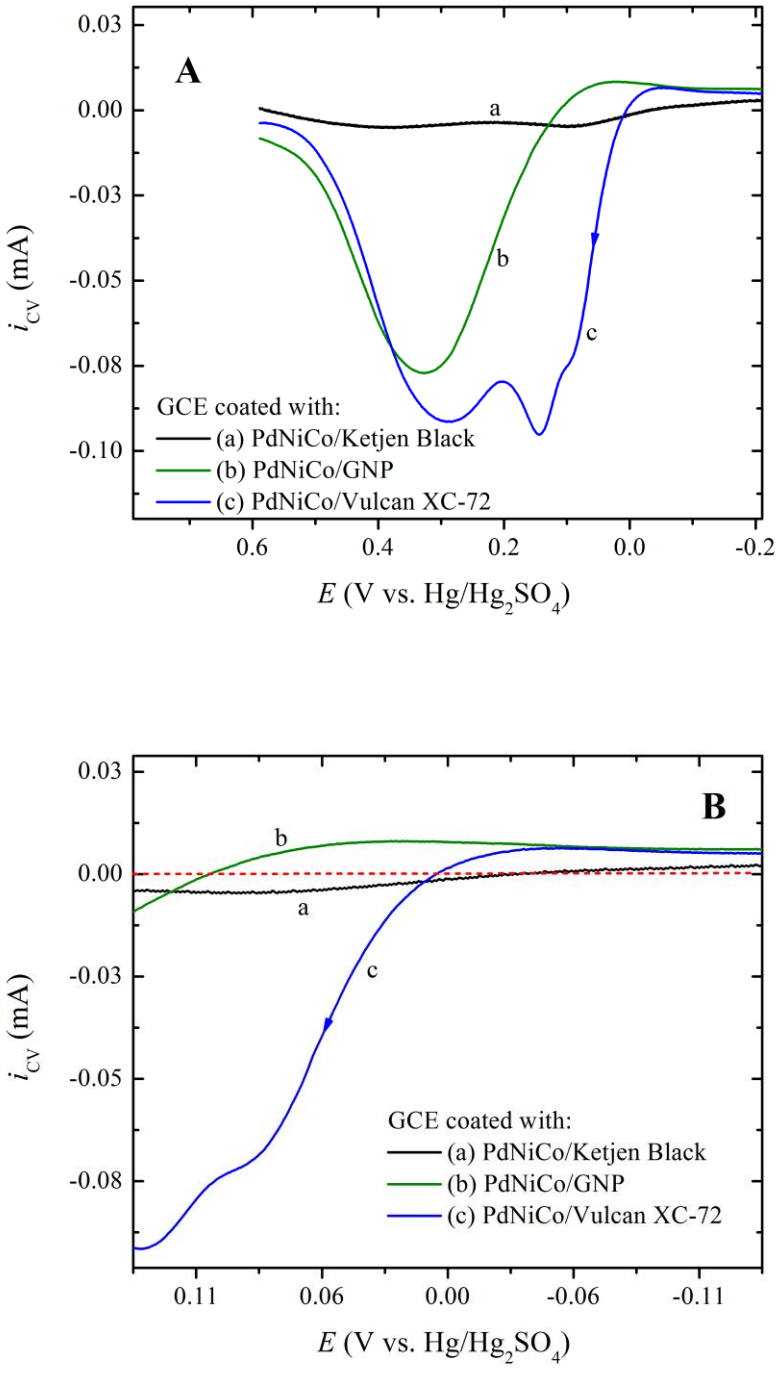

Figure 3.13 CO-stripping voltammograms of 10% PdNiCo/C.

Note: COSVs of (A) synthesized 10 wt% PdNiCo/C in 0.10 M $HClO_4$ at a scan rate of 20.0 mV/s. CO was preadsorbed at -0.54 V vs. Hg/Hg_2SO_4 for 20 min followed by N_2 purging. (B) Close-up.

As displayed in Figures 3.12 and 3.13, COSVs reveal that both Vulcan XC-72 and GNP supported catalysts have higher ECSAs as compared with the commercial catalyst. Specifically, the ECSA of 10% PdNiCo/VXC ternary nanocomposite (3.648 cm^2) is two times greater than that of the commercial 20% Pd/C (1.826 cm^2) and a few other commercial ones found in the literature, including 46.8% Pt/C, TKK (3.100 cm^2) and 35% Pd/C, BASF (0.790 cm^2) with even higher loads.[135] According to the Langmuir-Hinshelwood (L-H) mechanism, higher OH adsorption enhances CO oxidation, hence, particle size, morphology, and the addition of Ni and Co could play important roles for these catalysts.[134] Additionally, Ketjen Black supported catalysts have the lowest ECSAs among all tested catalysts, which could be attributed to the porous morphology of Ketjen Black and the lack of active catalytic materials on the surface (Table 3.6).

To explore the ani-CO poisoning activities, the onset potentials of CO-oxidation, E_O, V vs. Hg/Hg_2SO_4, were compared (Figures 3.12B and 3.13B). Except for the ternary PdNiCo/VXC and PdNiCo/GNP, all four other prepared catalysts have the E_O values either lower than or in close proximity to that of the commercial catalyst. This explains the anti-CO poisoning and superior catalytic activities of these catalysts towards FAO as well. The higher onset potentials of PdNiCo/VXC and PdNiCo/GNP could be caused by the presence of surface oxygen as revealed by the EDX spectra (Figure 3.7).

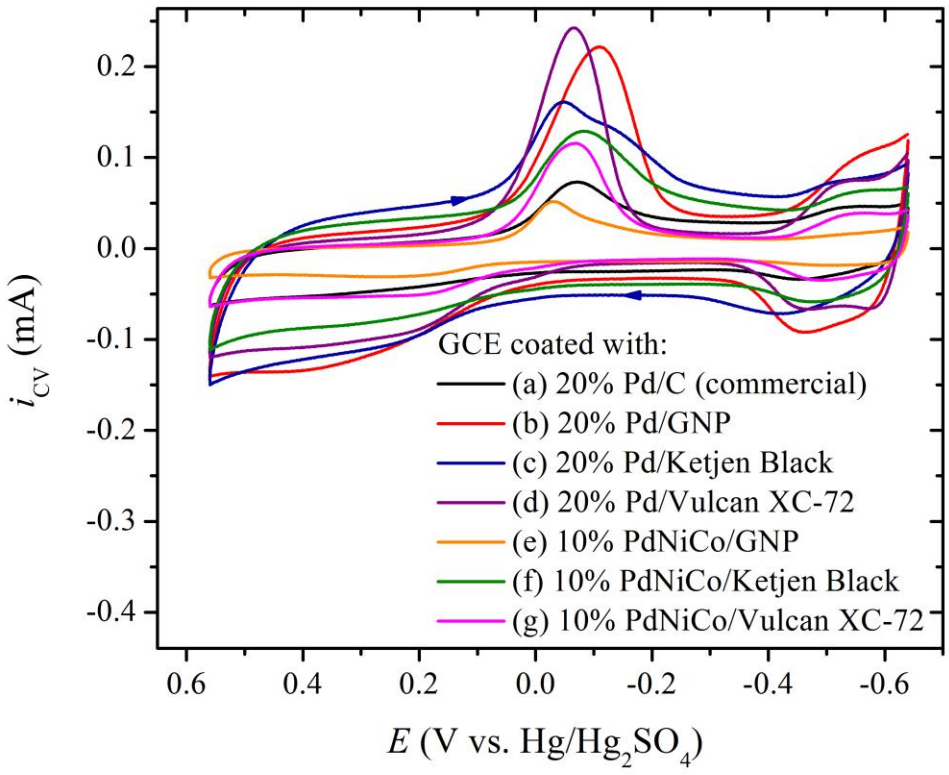

Figure 3.14 Background cyclic voltammograms after CO-stripping.

Note: CV signals were collected for all seven electrocatalysts after the CO oxidation scan to verify complete oxidation of the CO monolayer in 0.10 M $HClO_4$ at a scan rate of 20.0 mV/s.

Alternatively, the NiCo combination with Pd could enhance the adsorption of oxygen containing species. The lower the onset potential is, the easier the CO gets oxidized, hence the better the anti-CO poisoning activity would be. Background CV responses were also acquired to validate the absence of CO oxidation peaks (Figure 3.14), where significant reduction peaks on the reverse scans are due to the surface oxide reduction at ~0.0 V vs. Hg/Hg_2SO_4.

Table 3.6

Summary of COSV Results.

Nanocatalysts	E_O (V vs. Hg/Hg_2SO_4)	Q_{meas} (C)	ECSA (cm^2)
20% Pd/Vulcan XC-72	-0.074	9.805E-04	2.334
20% Pd/GNP	-0.029	8.836E-04	2.104
20% Pd/Ketjen Black	-0.052	4.455E-05	0.106
10% PdNiCo/Vulcan XC-72	+0.006	1.532E-03	3.648
10% PdNiCo/GNP	+0.106	9.058E-04	2.157
10% PdNiCo/Ketjen Black	-0.025	1.040E-04	0.248
20% Pd/C (commercial)	-0.029	7.668E-04	1.826

Note: The onset potentials, E_O (V vs. Hg/Hg_2SO_4) were obtained from the close-up CVs. Q_{meas}, (in Coulomb, C) and ECSA (cm^2) were also estimated for all the catalysts.

3.4 Conclusion

In this chapter, 20.0 wt% Pd and 10 wt% Pd with Ni and Co on Vulcan XC-72, Ketjen Black EC600, and graphite nanoparticles were synthesized using a simple one pot synthesis strategy. Their compositional effects on FAO, specific catalytic activities, long-term stabilities, and CO oxidation were investigated and compared to the commercial 20.0 wt% Pd/C. Enhanced specific FAO peak current was observed for 20.0 wt% Pd/VXC, with FAO electrocatalytic efficiency in the order of Pd/VXC > Pd/GNP > PdNiCo/VXC > Pd/C > PdNiCo/GNP ~ PdNiCo/KBE. On the other hand, extended surface area, morphology, and porosity played distinctive role on the stability of the nanocatalysts. Both CAs and multi-pulse CAs studies gave intricate comparison of the support materials towards enhancing the durability of the studied catalysts, which is in

the order of Ketjen Black EC600 > GNP > Vulcan XC-72 > activated carbon (commercial). Meanwhile, the addition of Ni and Co improved FAO activities by lowering the peak potential, which subsequently resulted the lower use of precious Pd. Hence, the ternary nanocomposites could be a promising electrocatalyst for DFAFCs. Finally, COSV results depicted that addition of Ni and Co also has a positive effect towards improved anti-CO poisoning. Although morphology plays an important role, the highest ECSA of Vulcan XC-72 supported catalysts also explained the high specific FAO current. In terms of ECSAs, the prepared catalysts could be positioned in the order of Vulcan XC-72 > GNP ~ activated carbon (commercial) > Ketjen Black EC600. Consequently, Vulcan XC-72 supported mono and ternary nanocomposites will be promising anode catalysts for DFAFCs, whereas Ketjen Black EC600 supported materials could be beneficial for long-term durability.

CHAPTER IV – TEMPLATE ASSISTED SYNTHESES OF NANOMATERIALS TOWARDS FORMIC ACID OXIDATION

4.1 Introduction

The ideal catalyst for formic acid oxidation (FAO), specifically the dehydrogenation pathway, should possess few crucial characteristics, which includes small particle size, roughness of the surface, presence of alloying component.[9] To promote the so-called third-body effect, Leiva et al. and Peng et al. studied the surface coverage effect of Bi and Sb on Pt to enhance the "direct pathway" and mitigate the CO poisoning.[155,156] Following their theoretical models, several approaches were taken to elevate coverage of monolayer (ML) of Bi and Sb on carbon-supported Pt and Pd nanoparticles.[4,10-12,27,37,152] It has also been established that an optimized amount of ML is needed to provide steric hindrance and to promote CH-down adsorption of HCOOH by diluting the Pt or Pd catalysts.[9,157]

On the other hand, Pd and Pt nanoparticles have been synthesized by chemical reduction reactions as well as electrochemical deposition.[4,5,23,27,35,40,151] Because smaller particle size increases the dispersion of the catalyst, Zhou et al. showed the optimum Pd/C size is around 6 – 7 nm that depends on the potential applied for FAO.[158] Very recently, Qian et al. reported the hydrothermal synthesis and enhanced FAO activity of Pd-Pt nanoparticles using octa-maleamic acid POSS stabilizer.[159] On the basis of previous studies,[160-165] Pd, Pt or other metal nanomaterials can be prepared using POSS as framework as shown in Figure 4.1. Amine-functionalized POSS such as octa-ammonium POSS (commercially available) can electrostatically interact with negatively charged transition metal complex ions such as $Pd^{II}Cl_4^{2-}$. The surface-confined metal ions

are then reduced by a reducing agent such as $NaBH_4$. With the nucleation and growth processes, metal nanoparticles are formed at the POSS cage corners. Self-assembly of POSS nanostructures could occur subsequently, leading to the formation of M-POSS nanosheets. This could be followed by a rolling-up process resulting in the production of M-nanotubes. Alternatively, M-nanoparticles could be obtained during the chemical reduction process.

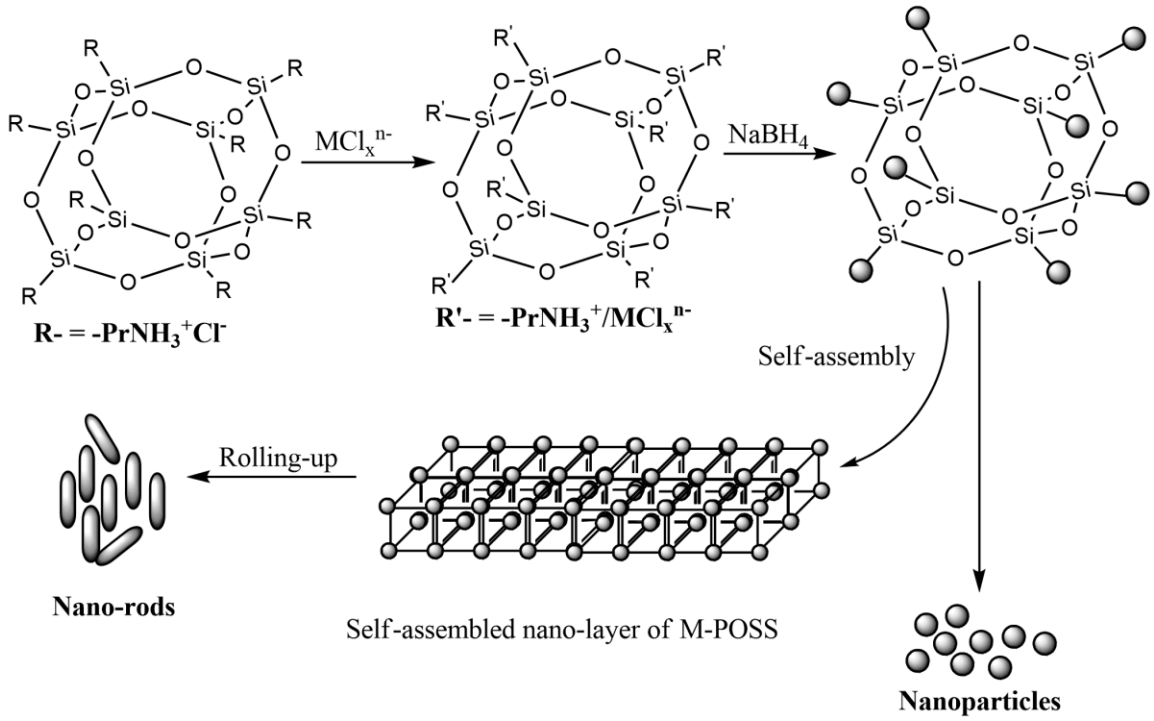

Figure 4.1 Strategy of template-assisted syntheses of nanomaterials using POSS.

In this chapter, the syntheses of Bi nanorods (Bi NRs) using OctaAmmonium POSS® (OA-POSS) as template and their characterization by SEM, EDX and TEM techniques are reported. The prepared Bi NRs are then mixed with 20 wt% Pd/C (commercial) to investigate the third-body enhancement effect for FAO. Different loadings of Bi NRs are also studied to optimize the Bi coverage with a fixed amount of Pd/C. The optimized composite is further characterized using SEM to show the surface

morphology. Additionally, well-dispersed Pd nanoparticles (Pd NPs) are prepared using POSS framework. Chemical and electrochemical characterizations are subsequently studied on the Pd NPs towards FAO.

4.2 Experimental Section

4.2.1 Chemicals

The chemicals were used as received. OctaAmmonium POSS® (OA-POSS, AM0285, $C_{24}H_{72}Cl_8N_8O_{12}Si_8$) was obtained from Hybrid Plastics Inc. $Bi(NO_3)_3 \cdot 5H_2O$ (≥99.99%) was purchased from Sigma Aldrich. Other reagents and catalyst have been described in previous chapters.

4.2.2 Syntheses of Bi NRs and Pd NPs using OA-POSS Template

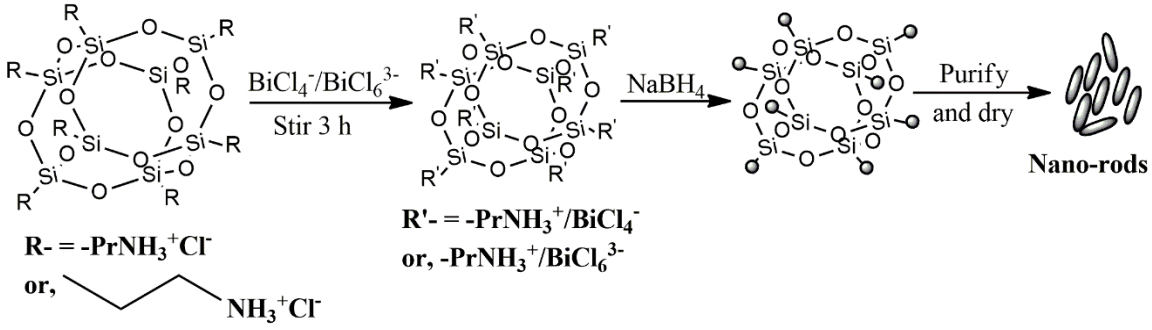

Figure 4.2 Preparation scheme of Bi NRs.

First, 20.00 mL of 10.0 mM $Bi(NO_3)_3 \cdot 5H_2O$ (97.0 mg) solution was prepared with a control of pH 2.0 using HCl to avoid insoluble $Bi(OH)_3$ generation. OA-POSS (117.3 mg) was dissolved in 20.00 mL deionized (DI) water separately to make a 5.0 mM solution. Equal volumes of the solutions were then mixed together to a total volume of 40.00 mL and stirred vigorously for 3 h. Afterwards, 10.00 mL solution of 40.0 mM $NaBH_4$ (15.1 mg) was delivered into the mixture using a mini-flow variable-speed pump (VWR International). The reaction was monitored by color change from colorless to

black. The pH was adjusted to ~4.0 immediately using HCl to avoid Bi NR dissolution. The product was centrifuged with exhaustive washing using DI water and ethanol. Finally, the product was dried under vacuum at 60 °C for 2 h and stored in a desiccator. Similarly, Pd NPs were synthesized utilizing the above one pot synthesis strategy using $PdCl_2$ and OA-POSS reactants. In this case, the color change was from brown to black.

4.2.3 Catalyst Ink Preparation and Working Electrode Modification

The prepared Bi NRs were mixed with 20% Pd/C from the stock solutions. Various catalytic loads of Bi NRs were maintained using a fixed amount of Pd/C (0.025 mg Pd) and different amounts of Bi NRs (0.100 mg to 0.00625 mg Bi). The catalysts were ultrasonicated to disperse and drop casted on a clean GCE following the same protocol as before as described in Chapter III. Pd NP-modified GCE was also investigated towards FAO separately.

4.3 Results and Discussion

4.3.1 Characterization

Bismuth nanorods (Bi NRs), 1:1 mixture of Bi NRs with Pd/C, and Pd NPs were dispersed separately in ethanol by ultrasonication. SEM and TEM (JEOL 2100) images were captured following the usual protocol. EDX spectra and mapping were also utilized to obtain elemental compositions.

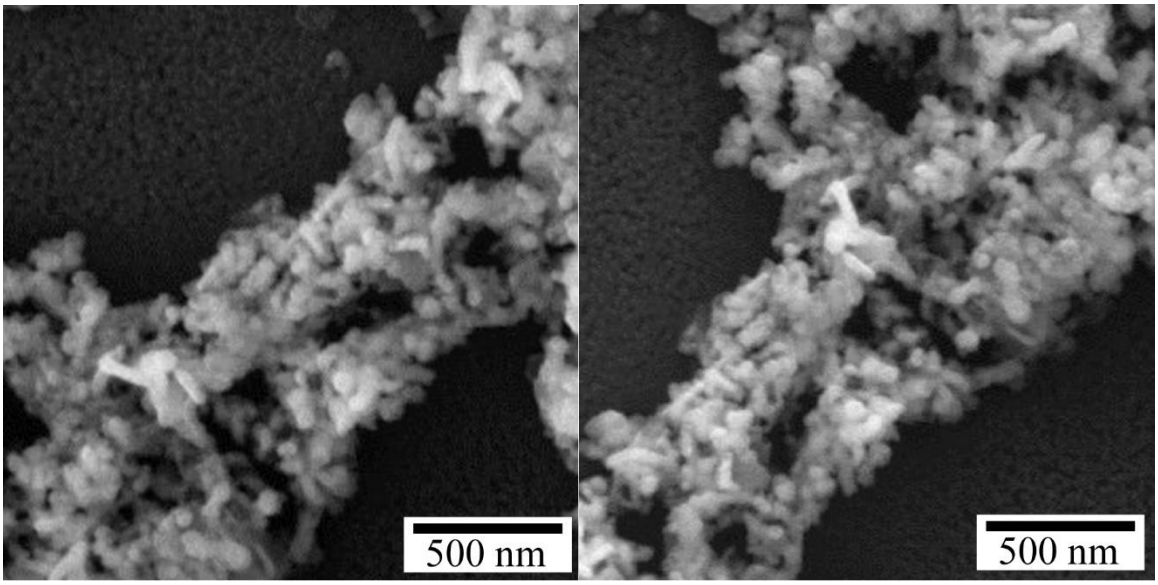

Figure 4.3 SEM images of Bi NRs.

Note: SEM images were taken on Si wafer after Ag-sputtering.

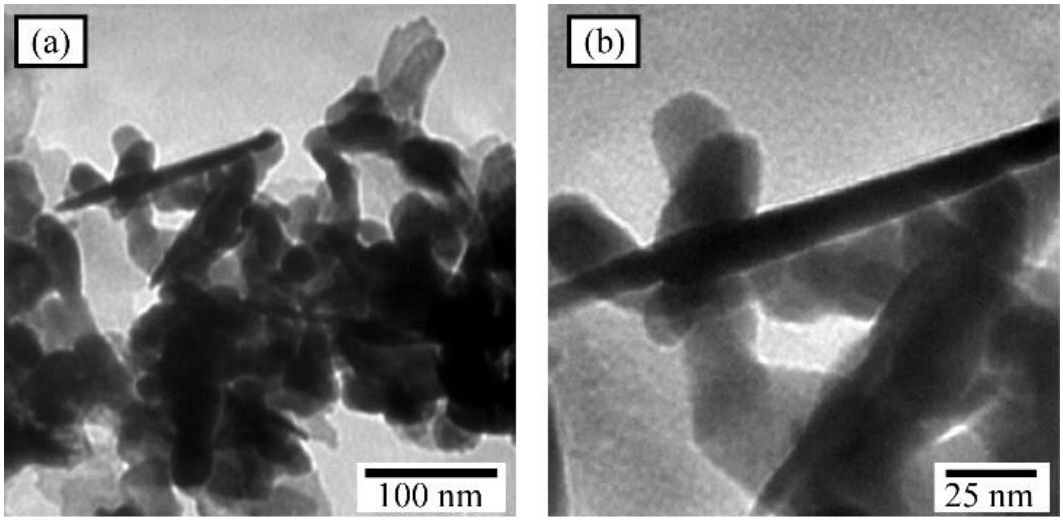

Figure 4.4 TEM images of (a) Bi NRs and (b) close-up.

Note: TEM images were captured on a Cu-grid.

Both Figures 4.3 and 4.4 reveal that the rod-like clustered morphology of the Bi NRs has an average dimension of ~50 × 20 nm^2. Although, few needle-shaped rods are

also formed but the nanorice shapes are predominant. The high surface area of the Bi NRs could provide more surface coverage with a small amount of the material.

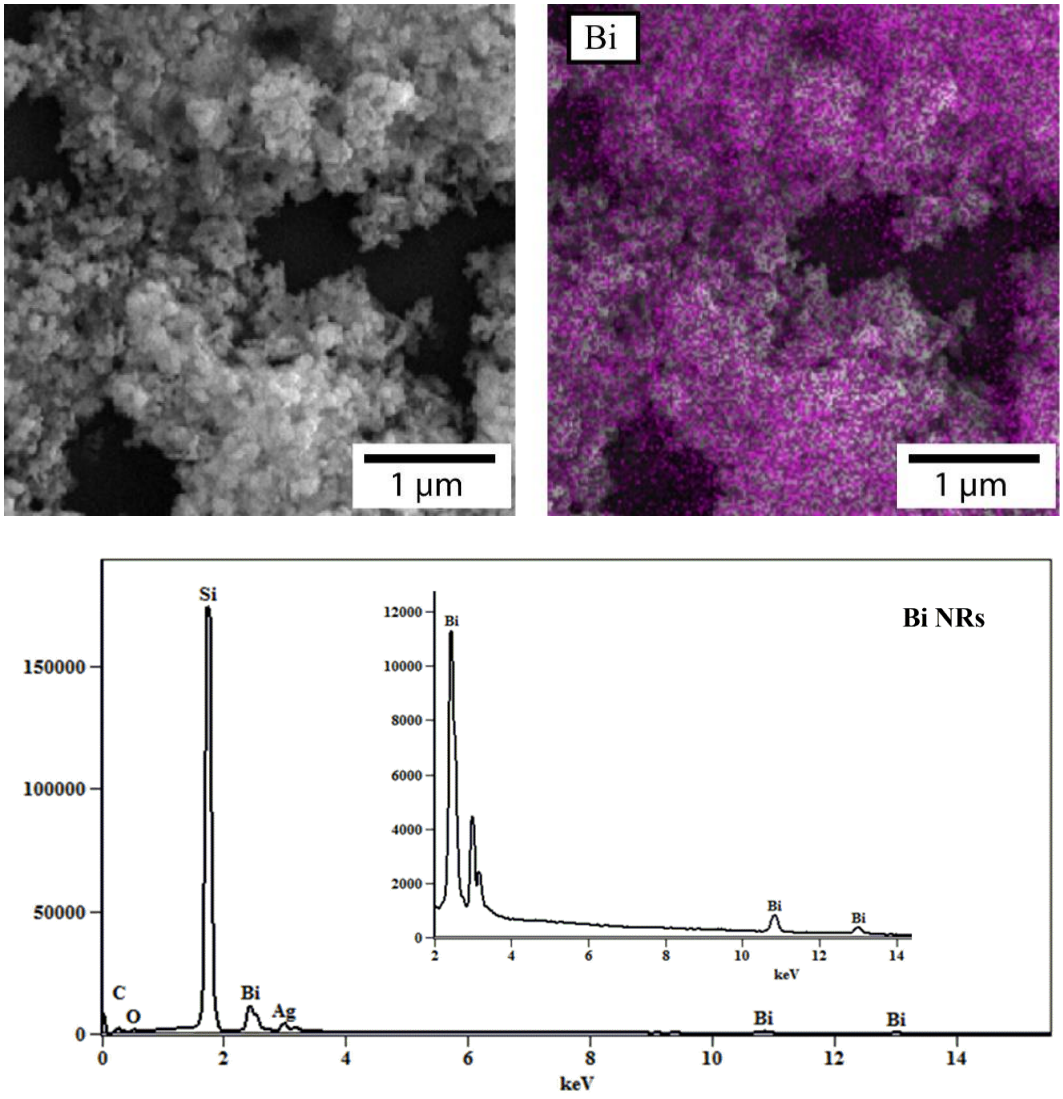

Figure 4.5 EDX mapping and spectra of Bi NRs.

Note: EDX mapping and spectra were collected to find the elemental composition of the Bi NRs. Si, Ag, C and O were discarded from the mapping images as background.

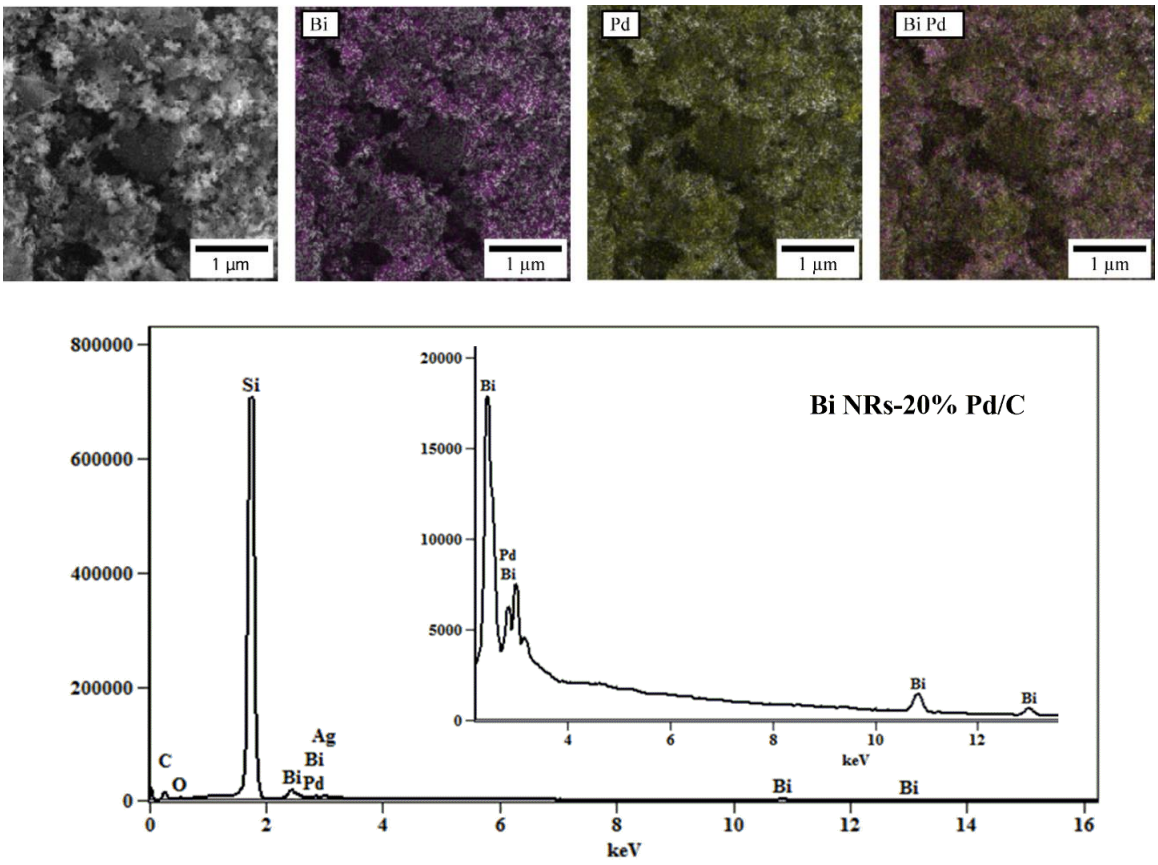

Figure 4.6 EDX mapping and spectra of Bi NRs mixed with 20% Pd/C.

Note: EDX mapping and spectra were obtained to find the distribution, morphology and elemental composition of the 1:1 mixture of Bi NRs and 20% Pd/C. Si, Ag, C and O were discarded from the mapping images as background.

The EDX mappings and spectra confirm the composition of the prepared Bi NRs and the composite (Figures 4.5 and 4.6). The agglomerated Bi NRs were ultrasonicated for 60 min to disperse in the 20% Pd/C before each experiment. Thus, the mapping clearly shows the nano-rods are well-dispersed on the surface of the Pd/C. Moreover, Table 4.1 displays the estimated weight% of the samples, where Si, Ag and small % of O are listed as background elements.

Table 4.1

Elemental compositions of Bi NRs and the 1:1 mixture of Bi NRs with 20% Pd/C.

Weight%	Bi	Pd	Si	Ag	O	C
Bi NRs	9.41±0.06	-	81.80±0.26	7.58±0.05	1.22±0.03	-
Bi NRs + Pd/C	7.94±0.05	1.73±0.03	72.58±0.23	2.43±0.05	1.97±0.04	13.35±0.13

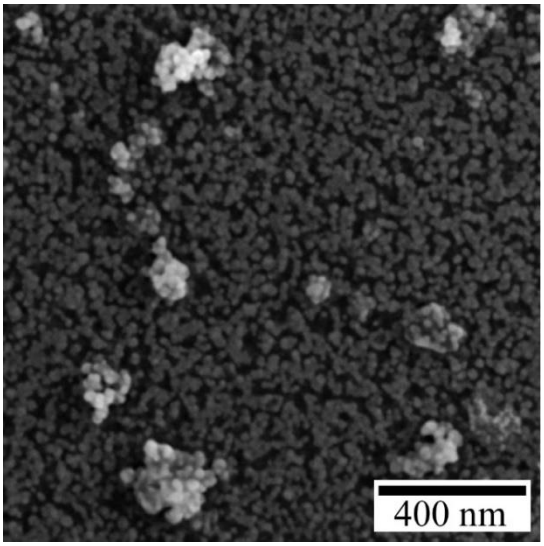

Figure 4.7 SEM image of Pd NPs.

Note: SEM images were taken on Si wafer after Ag-sputtering.

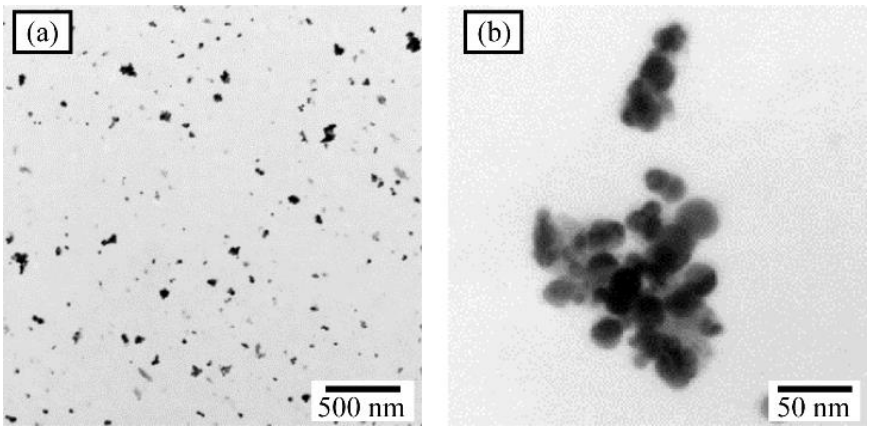

Figure 4.8 TEM images of (a) Pd NPs and (b) close-up.

Note: TEM images were captured on a Cu-grid.

The SEM and TEM images (Figures 4.7 and 4.8) of Pd NPs display the well-dispersed spheres with the presence of few clusters. The TEM image also shows an average particle size of ~10 nm diameter. The EDX spectra confirm the elemental composition as illustrated in Figure 4.9, where Ag signal from sputtering was removed for clarity. The close-up spectra in Figure 4.9 clearly shows the presence of Pd, which was confirmed further by detecting five other different samples on several spots (not shown). The agglomeration was caused probably because the particles were not supported or not capped by any capping agents. Ultrasonication for a longer time period of 60 min made the samples well-dispersed before capturing the final images.

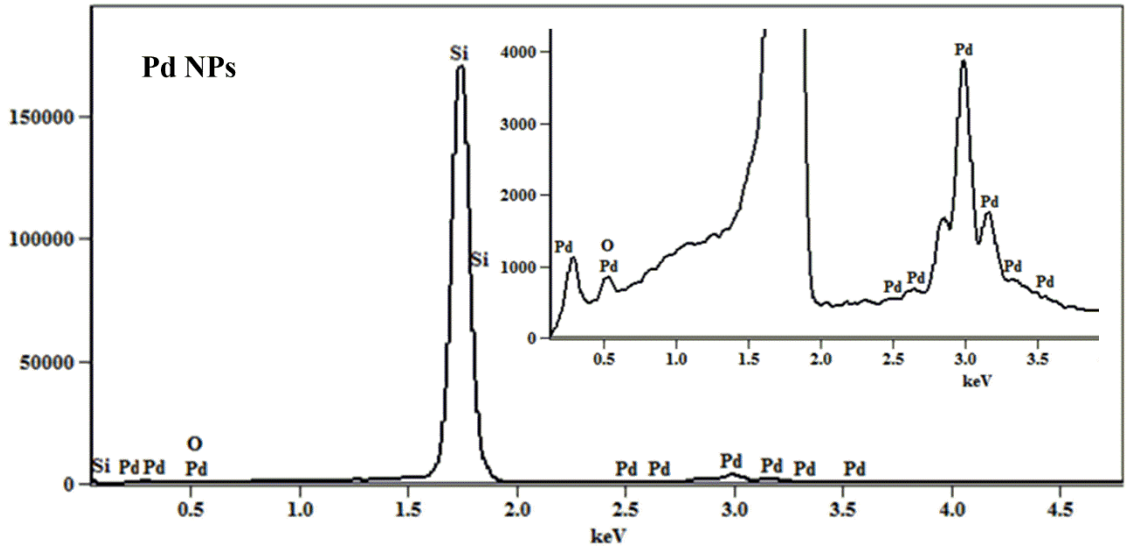

Figure 4.9 EDX spectra of Pd NPs.

4.3.2 Electrochemical Studies

4.3.2.1 Third-body Effect of Bi NRs towards FAO

The background CV response (Figure 4.10) was collected for a wide potential window to completely observe the typical hydrogen adsorption/desorption region from -0.23 V to -0.90 V vs. Hg/Hg_2SO_4 at a Bi NRs modified GCE. The experiment was carried out under N_2 environment, therefore the peak at -0.39 V is solely due to hydrogen desorption. The high current from this region also corresponds to high surface area of the prepared nano-rods.[10] Figure 4.10 further confirms that Bi alone has no catalytic activity towards FAO and could be utilized as a surface blocker for FAO catalysts.

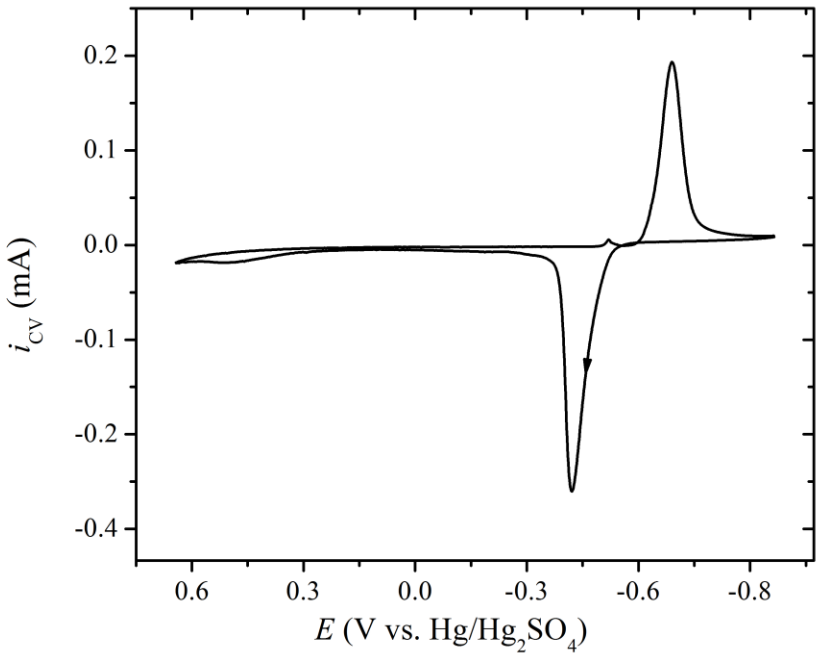

Figure 4.10 Background CV at Bi NRs modified GCE.

Note: CV signal was collected at Bi NRs modified GCE using 0.50 M HCOOH with 0.10 M H_2SO_4 at a scan rate of 20.0 mV/s.

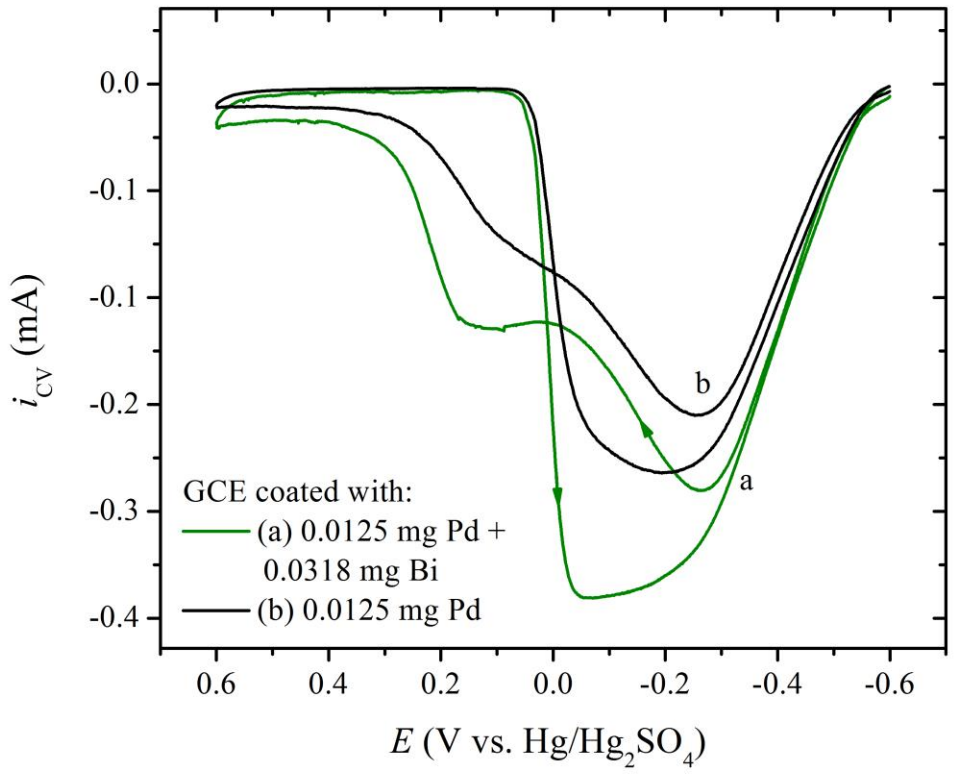

Figure 4.11 Cyclic voltammograms showing the effect of (a) Bi NRs addition to 20% Pd/C vs. (b) 20% Pd/C only.

Note: CV responses of 0.50 M HCOOH with 0.10 M H_2SO_4 using (a) 20% Pd/C mixed with Bi NRs where the load is 0.0125 mg Pd with 0.0318 mg Bi and (b) 20% Pd/C only with a load of 0.0125 mg Pd/cm^2 GCE at a scan rate of 20.0 mV/s.

To monitor the effect of added Bi to Pd/C, CVs were initially obtained with and without the Bi NRs from a fixed loading of 0.0125 mg Pd. Figure 4.11a shows a FAO peak current of 0.27 mA on the forward scan and 0.34 mA on the reverse scan at Bi NRs-Pd/C electrode. Figure 4.11b shows that without Bi NRs, the peak currents from Pd/C only are 0.22 mA and 0.25 mA, respectively. The enhanced FAO peak current led to the

following experiments, in which the influence of Bi loading on the FAO efficiency at Bi NRs-Pd/C electrode was investigated.

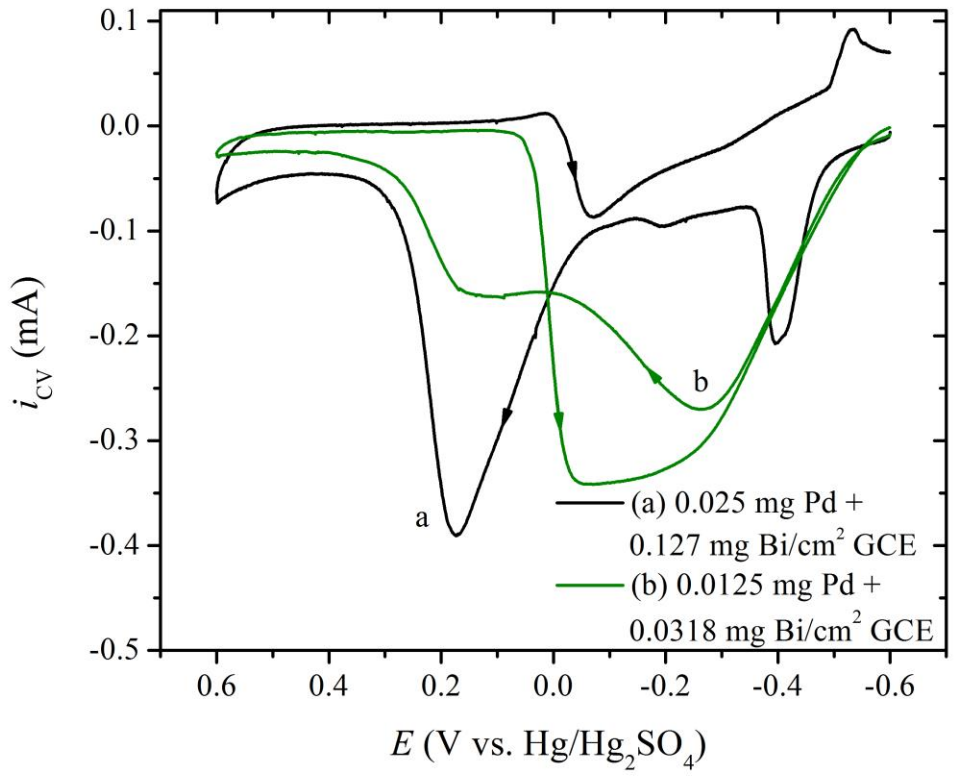

Figure 4.12 Cyclic voltammograms of different loads of Bi NRs with 20% Pd/C.

Note: CV responses of 0.50 M HCOOH with 0.10 M H_2SO_4 using 20% Pd/C mixed with Bi NRs where the loads are (a) 0.025 mg Pd with 0.127 mg Bi and (b) 0.0125 mg Pd with 0.0318 mg Bi/cm^2 GCE at a scan rate of 20.0 mV/s.

As displayed in Figure 4.12a, a higher loading of Bi essentially blocks the Pd surface and the FAO predominantly follows the indirect pathway on the forward scan with a peak current of 0.39 mA at 0.17 V vs. Hg/Hg_2SO_4. On the reverse scan, the FAO peak appears at -0.09 V with a low current of 0.07 mA. At ~-0.40 – -0.50 V region, the typical hydrogen adsorption/desorption peaks are present as well. On the other hand,

when lower loadings of Bi NRs mixed with Pd/C were used, CV responses showed mainly direct FAO peaks on both forward and reverse scans along with a small shoulder on the forward scan involving indirect FAO.

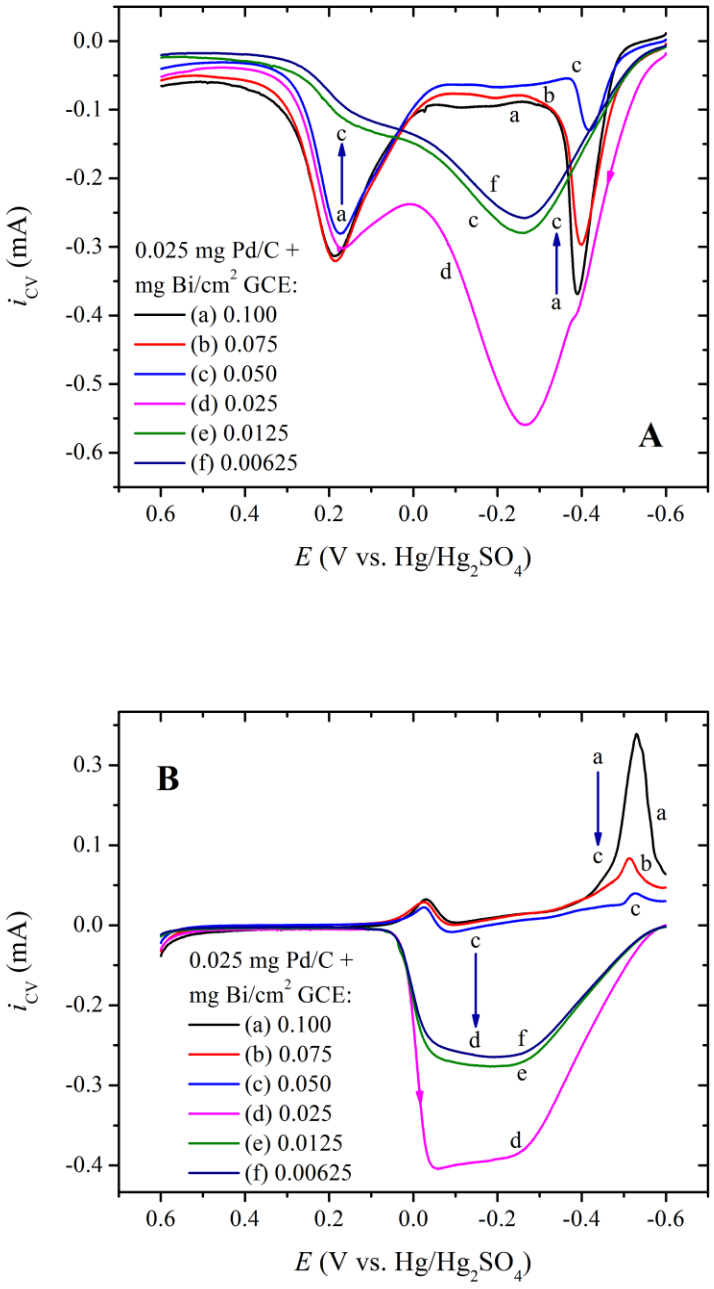

Figure 4.13 Study of the different loads of Bi NRs to a fixed load of 20% Pd/C.

Note: CV responses of 0.50 M HCOOH with 0.10 M H_2SO_4 using 0.025 mg Pd load of 20% Pd/C mixed with Bi NRs where the loads are (a) 0.100 mg Bi to (f) 0.00625 mg Bi/cm^2 GCE collected at a scan rate of 20.0 mV/s.

Thus, a fixed amount of 20% Pd/C catalyst (0.025 mg Pd) was dispersed ultrasonically with different amounts of Bi NRs to maintain loadings starting from 0.100 to 0.00625 mg Bi/cm^2 of GCE. Figure 4.13 shows the loading dependent study of Bi vs. Pd. The higher loadings of 0.100 to 0.050 mg Bi mostly cover the Pd surface and thereby the FAO follows the indirect pathway. The 1:1 mass ratio of Pd:Bi (2:1 molar ratio) showed the highest peak current and the dual pathways of FAO. Furthermore, the hydrogen adsorption/desorption peak currents also decrease with a decrease in Bi loading. At 0.0125 mg of Bi (Figure 4.13e), the low peak current could be attributed to the absence of hydrogen adsorption/desorption peaks and only FAO current is observed with a peak potential shift of 172.8 mV vs. the Pd/C only. This phenomenon illustrates the third-body effect of Bi when dispersed with Pd/C. Because the Bi rods have high surface area, only a small amount could be beneficial to obtain the enhanced FAO due to the steric hindrance provided by the Bi coverage on Pd/C. Additionally, the optimum Bi-coverage could enhance the C-H down pathway of HCOOH adsorption,[9] which leads to the peak potential shift, hence greater FAO efficiency.

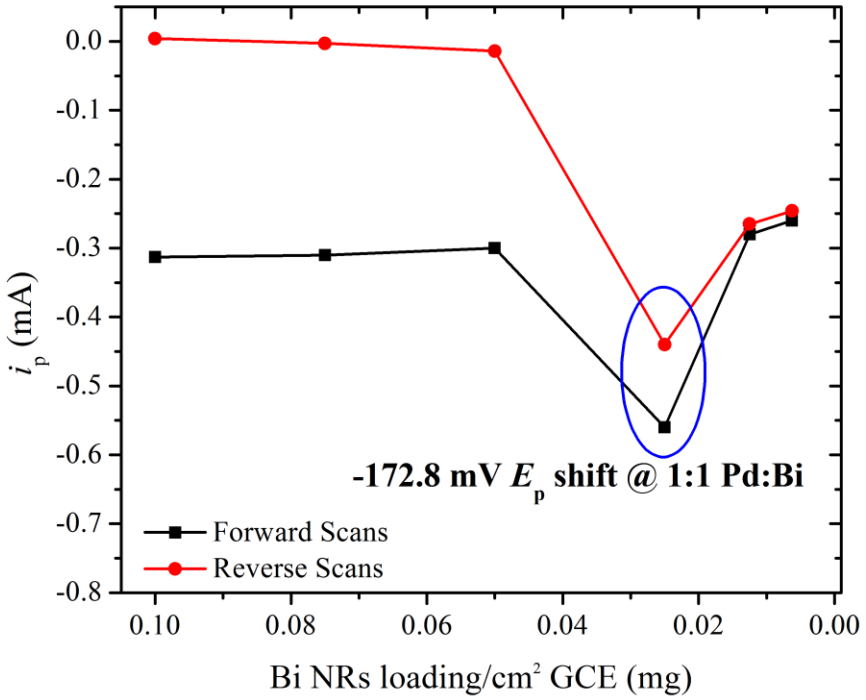

Figure 4.14 Peak current trends of the different loadings of Bi NRs to a fixed load of 20% Pd/C.

Note: Peak currents from the CVs of Figure 4.12 were plotted against the Bi NRs loads that shows the 1:1 mass ratio of Pd:Bi had the highest peak current with a peak potential shift of 172.8 mV towards the negative direction vs. the 20% Pd/C only.

The trend in peak currents from the direct FAO are plotted against the Bi NRs loading in Figure 4.14 to display the overall change. The combination of Pd/C and Bi NRs with a mass ratio of 1:1 or lower would be the preferred composite towards FAO. Although there is a slight decrease in peak currents at lower Bi loadings, the peak potential change shows the superior catalytic activity of 20 Pd/C when blended with the synthesized Bi NRs. The EDX mapping images also confirmed the uniform blending of Bi and Pd at 1:1 ratio (Figure 4.6).

4.3.2.2 Electrochemical Investigation of Pd NPs

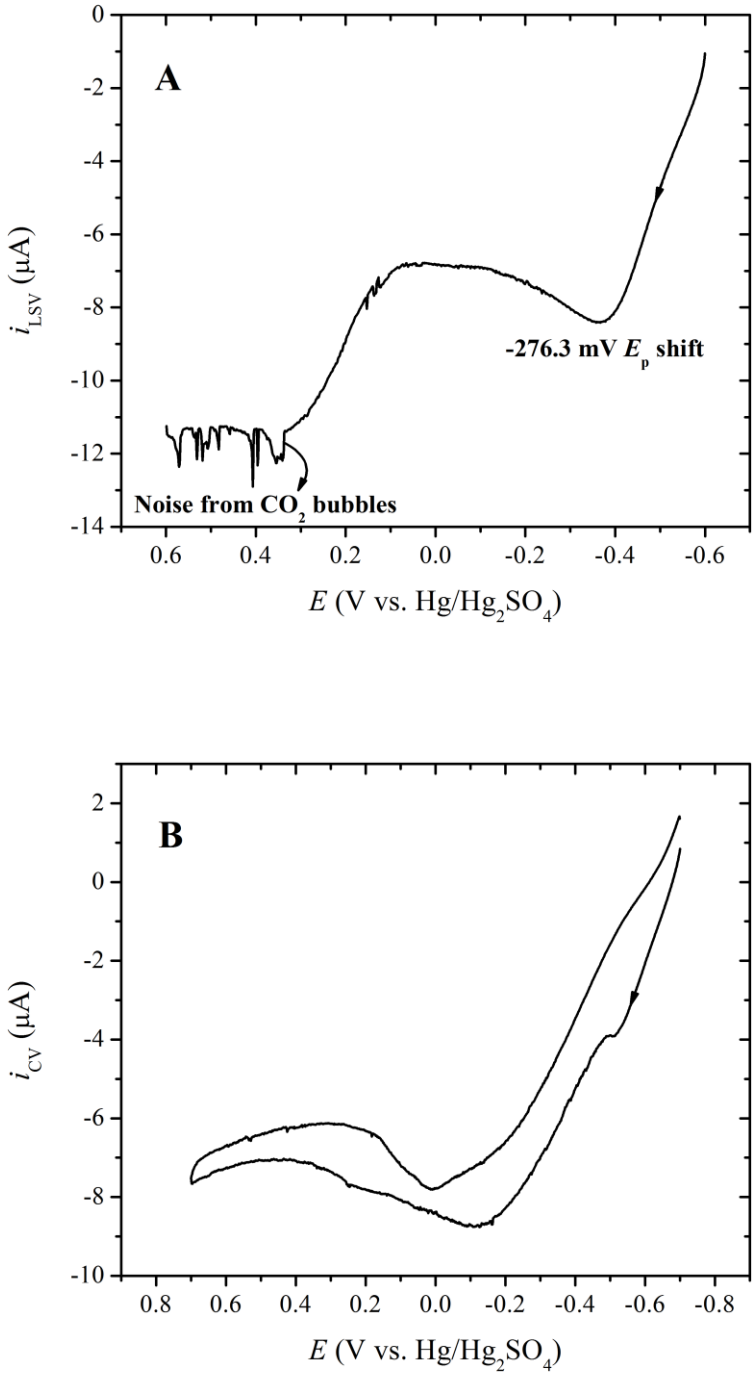

Figure 4.15 Voltammetry responses of FAO at Pd NPs modified GCE.

Note: (A) LSV response of 0.50 M HCOOH in 0.10 M H_2SO_4 using 0.025 mg Pd load of Pd NPs/cm^2 GCE and (B) CV signal with a higher load of 0.85 mg Pd collected at a scan rate of 20.0 mV/s. The noise in Figure (A) around 0.30 V vs. Hg/Hg_2SO_4 onwards was due to CO_2 bubble formation.

Linear sweep and cyclic voltammetry signals obtained from Pd NPs modified GCE for FAO are shown in Figure 4.15. At the low catalytic load of 0.025 mg Pd NPs/cm^2 (Figure 4.15A), the peak currents are in the μA ranges and the signals are noisy as a result of the CO_2 bubbles. However, a peak potential shift of 276.3 mV towards the negative direction relative to the commercial 20% Pd/C may illustrate the effect of smaller particle size. Furthermore, the CV signal with a higher load of 0.85 mg shows mainly the dehydrogenation pathway of FAO with no apparent surface oxide reduction but predominantly FAO on the reverse scan (Figure 4.15B).

Finally, multi-pulse CA response for ~4000 cycles (4.27 h) between 0.10 and 0.60 V vs. Hg/Hg_2SO_4 exhibits the overall change in FAO current over time (Figure 4.16). The % of current change of -36.67% was calculated using Equation 1.6. Compared to the commercial 20% Pd/C (Table 3.5), the synthesized Pd NPs are 2.5 times more durable. The close-up image also shows that the change in initial current is low. Thus, the Pd NPs prepared using OA-POSS template could be a better candidate for FAO in terms of long-term durability.

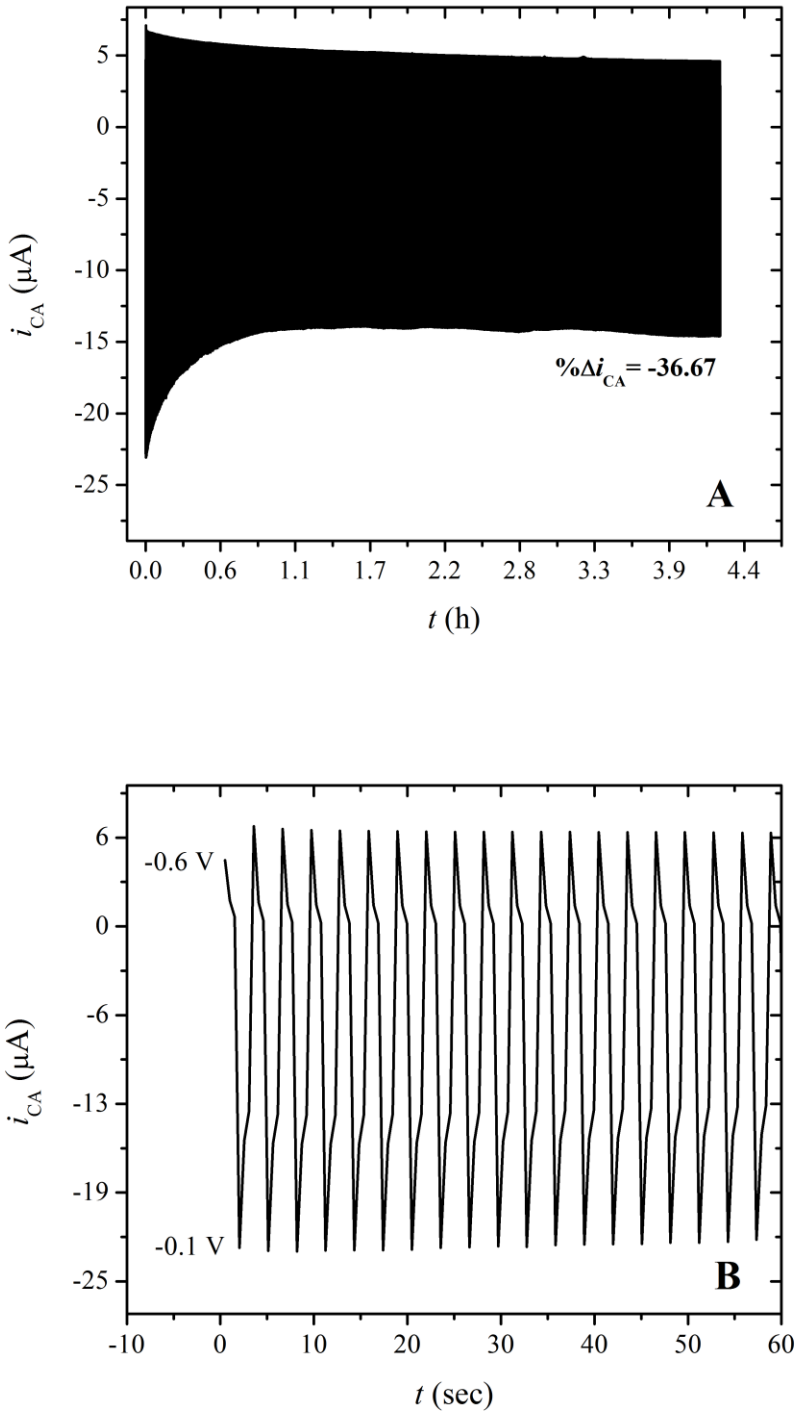

Figure 4.16 Multi-pulse chronoamperometry signals for stability test of Pd NPs.

Note: Pulse CA signals of (A) prepared Pd NPs for ~4000 cycles (4.27 h) between 0.10 and -0.60 V vs. Hg/Hg_2SO_4, (B) Close-up from 0 to 60 sec.

4.4 Conclusion

The unique Bi NRs and Pd NPs were prepared using OA-POSS template using a one pot synthesis process. The prepared nanomaterials were characterized using SEM, TEM, EDX spectra and mapping to acquire the morphology, size distribution, uniformity, and elemental compositions. These materials were also investigated towards FAO, where Bi NRs showed enhanced FAO activity by third-body effect when blended with the commercial 20% Pd/C catalyst. The Bi-loading dependent study revealed that very small amounts of Bi NRs can have positive impact on the catalytic activity of Pd/C, mainly due to the high surface of the nano-rods and thereby providing steric hindrance. Pd NPs also exhibited long-term durability as compared with the commercial catalyst.

CHAPTER V – SCREENING OF TRANSITION METAL COMPLEXES AND Pd/C BLENDS AS ANODIC FORMIC ACID ELECTROCATALYSTS

5.1 Introduction

To reduce expensive precious metal loading, non-noble metal catalysts have been studied over the last three decades for PEMFCs.[166-168] Among the new materials, transition metal complexes have attracted worldwide attention since the first report of cobalt phthalocyanine (Pc) as cathodic catalyst for oxygen reduction reaction (ORR) by Jasinski in 1964.[169] Specifically, Pc, porphyrin, and their derivatives have been investigated with non-noble transition metals such as V, Co, Ni, Mn, Cu, Zn, and Mo etc.[170-174] However, the syntheses steps and necessity of pyrolysis to make them stable are major concerns.[175-177]

Since the reaction precursors are commercially available as discussed in Chapter I, the syntheses of the proposed M-POSS complexes are generally straightforward. Furthermore, by dispersing with other nanomaterials, composite M-POSS complexes (e.g., M_1/M_2-POSS) may be formed. Alternatively, a homogeneous solution containing several different types of metal complexes could be readily obtained in a common miscible medium (e.g., M_1-POSS + M_2-POSS + …), which may yield another kind of composite M-POSS catalyst. Their catalytic efficiencies towards the electrooxidation of formic acid could be significantly increased as in the cases in which alloying catalysts are employed.[4,5,11,27,36-40,44,58-62]

Recently, a few approaches have been explored towards the catalytic enhancement of formic acid oxidation (FAO) utilizing transition metal complexes. Chenitz et al. reported a number of metal-Pc complex impregnated Pd/C and Pt/C

composites, where CoPc, MnPc, and FePc with Pt/C showed enhanced activity.[178] Additionally, the higher stability of Pt-Co and Pt-Ru composites were also stated. On the other hand, promoting effect of vanadium and palladium ions in electrolyte on Pd/C were also investigated.[17,88] Based on the synergistic effect of these ions to promote CO oxidation and facilitating FAO, Yu and Pickup reviewed and screened many bimetallic systems.[152] Metal-acetylacetonate (M-acac) complexes are typically used as catalyst or precursor of organic synthesis. Einaga et al. studied CO oxidation catalysts impregnated by M-acac complexes as precursor to dilute the noble metal and form nanoparticles on TiO_2 support.[179] However, to our best knowledge, neither M-acac nor M-POSS complexes were explored as FAO catalyst component. Consequently, this chapter presents some studies in this field, especially potential blends of transition metal complexes and Pd/C. First, the precursor and M-POSS complexes are synthesized according to the literature with modifications.[117,180,181] The FAO activity is then studied using both GCE and Pt electrodes. In addition, six M-acac complexes are combined individually with a fixed amount of Pd/C and their activities and stabilities are established. Finally, the third-body effect of Bi NRs on the V(III)-acac and Pd/C is tested and the possible combinations for future studies are proposed based on the above preliminary results.

5.2 Experimental Section

5.2.1 Chemicals

All of the metal-acac complexes were acquired from Sigma-Aldrich with less than 1% impurity. C_6H_6 and CH_2Cl_2 were procured from Fisher Scientific and purified prior

use. NBu_4Cl (98%) was purchased from Acros Organics. The rest of the materials used were listed in previous chapters.

5.2.2 Syntheses of M-POSS Complexes

Anhydrous $FeCl_3$ (81.1 mg, 0.50 mmol) was dissolved in 20.00 mL 6.0 M HCl. NBu_4Cl (139.0 mg, 0.50 mmol) dissolved in 0.50 mL distilled water was added to the clear yellow solution of $[FeCl_4]^-$. The solution turned to cloudy yellow suspension upon stirring. The yellow solid was filtered and washed with 4.0 M HCl to remove any excess reactants. It was then dried under vacuum and recrystallized from methanol to obtain bright yellow crystals of $[NBu_4][FeCl_4]$. As shown in Figure 5.1, crystals of $[NBu_4][FeCl_4]$ (404.9 mg, 0.92 mmol) and trisilanolisobutyl-POSS, $((CH_3)_2CHCH_2)_7Si_7O_{12}H_3$ (728.1 mg, 0.92 mmol, from Hybrid Plastics Inc.) were added in a mixture of 30.00 mL toluene (solvent) and 4.0 mL triethylamine (catalyst). Both toluene and triethylamine were dried overnight using molecular sieve (3 Å) before use. The light-yellow solution was stirred at room temperature for 12 h. Then the solution was filtered and hexane was added to the filtrate. It was left to cool and obtain the crystals of Fe(III)-POSS at -20 °C.

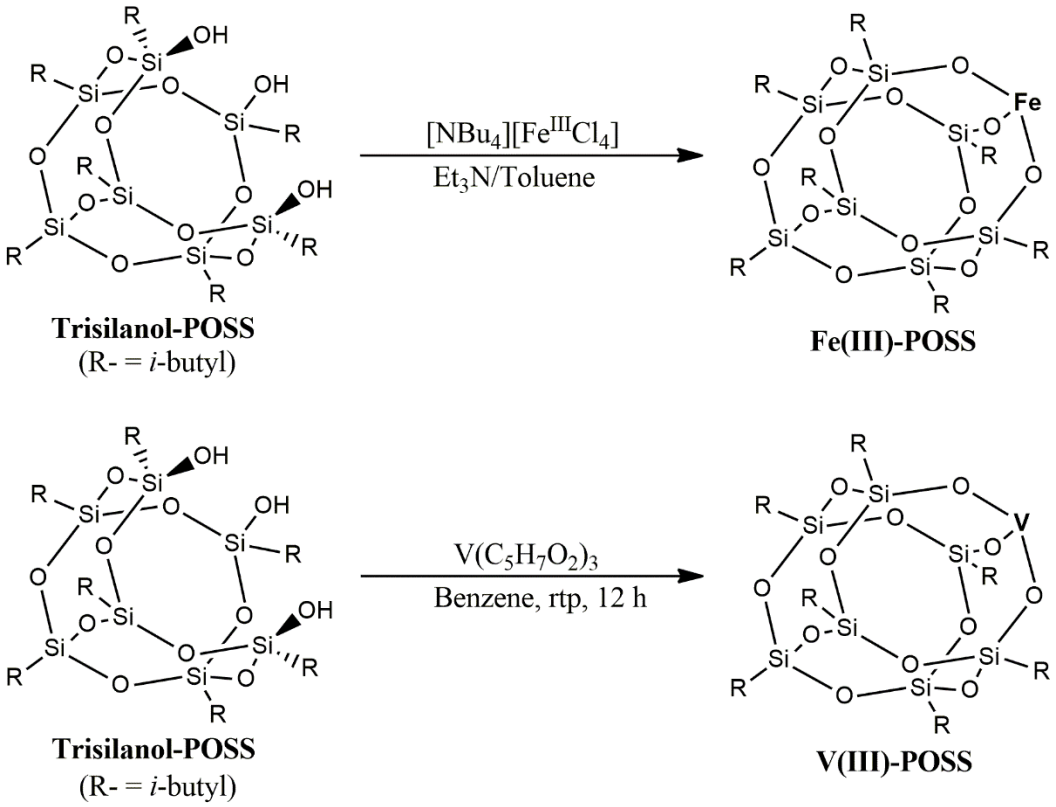

Figure 5.1 Synthesis schemes of Fe(III)-POSS and V(III)-POSS complexes.

Additionally, a 2.0 mL solution of $V(acac)_3$, $V(C_5H_7O_2)_3$ (184.6 mg, 0.53 mmol) was dissolved in benzene. Trisilanol-POSS (411.5 mg, 0.52 mmol) was separately mixed with 20.0 mL benzene. Upon vigorous stirring, the two solutions were mixed and stirred for another 12 h. Then the solvent was removed and the light green solid was recrystallized under CH_2Cl_2 to obtain V(III)-POSS. Both the Fe(III)-POSS and V(III)-POSS could be a mixture of mono- and dimeric complexes.[117,180,181] The products were subjected to electrochemical studies and were not characterized further.

5.2.3 Electrochemical Measurements

All voltammograms and chronoamperometry responses were collected using the same protocol as described in Chapters I and III. The catalyst ink was prepared by

ultrasonicating a fixed amount of 20% Pd/C and individual metal-complexes for 60 min prior to modifying GCE.

5.3 Results and Discussion

5.3.1 FAO Activity of M-POSS Complexes

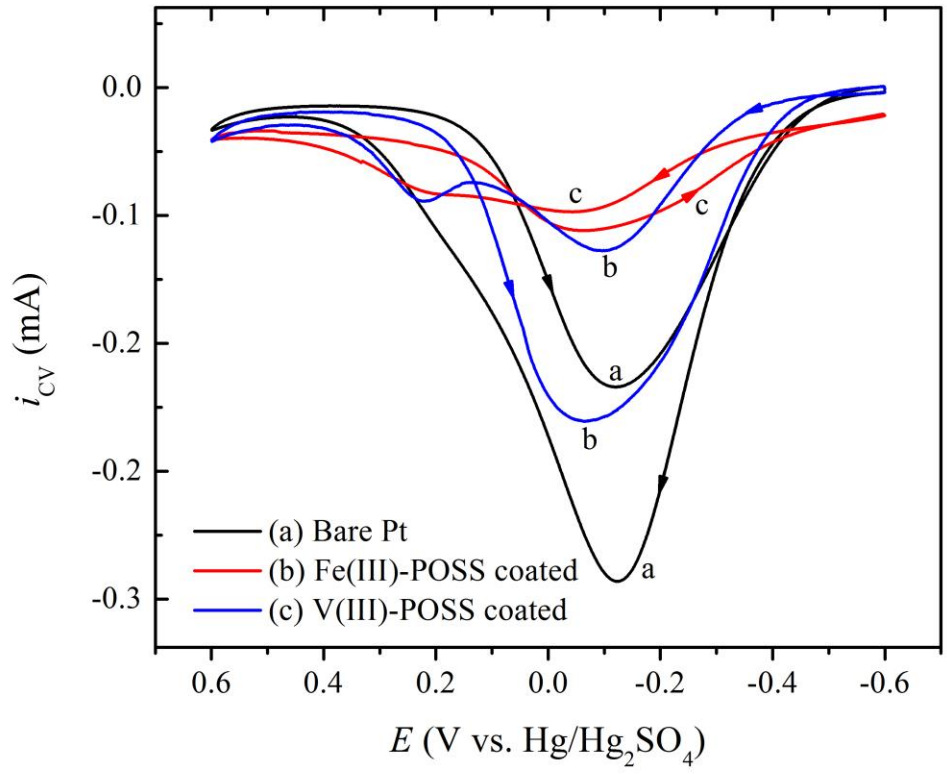

Figure 5.2 Effect of M-POSS coated surface on FAO vs. bare Pt electrode.

Note: CV signals of 0.50 M HCOOH with 0.10 M H_2SO_4 using (a) bare Pt, (b) Fe(III)-POSS coated Pt, and (c) V(III)-POSS coated Pt working electrode at a scan rate of 20.0 mV/s.

To verify the catalytic activity of the prepared Fe(III)-POSS and V(III)-POSS complexes, CV responses were obtained from bare Pt and catalyst coated electrodes as shown in Figure 5.2. Because Pt itself is catalytic towards FAO, the bare Pt shows a

higher FAO current than Fe(III)-POSS coated Pt electrode. However, on the reverse scan, V(III)-POSS coated electrode shows a slightly higher current than that of the forward scan at bare Pt. Note that, there is no catalytic activity from V(III)-POSS itself when a similar experiment is performed using GCE electrode (Figure 5.3). These experiments also provide the idea of utilizing V(III)-POSS as a second component of Pt or Pd catalyst.

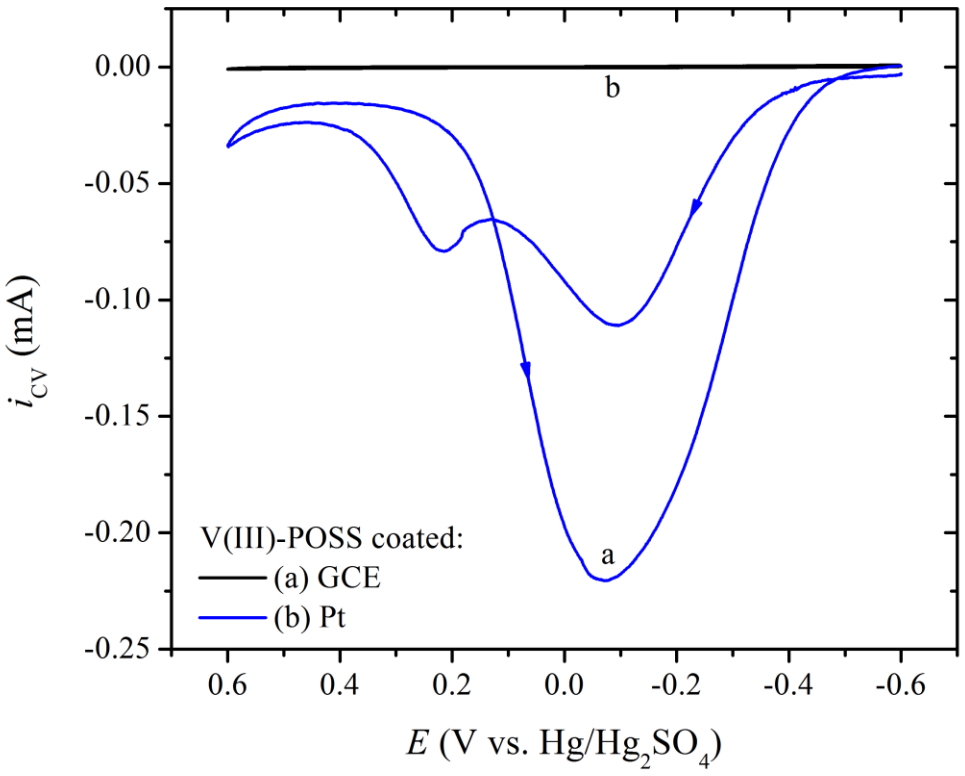

Figure 5.3 Effect of V(III)-POSS coated GCE vs. Pt working electrode on FAO.

Note: CV signals of 0.50 M HCOOH with 0.10 M H_2SO_4 using a constant load of 0.025 mg of V(III)-POSS/cm^2 of (a) GCE and (b) Pt at a scan rate of 20.0 mV/s.

The next attempt was to mix V(III)-POSS (0.028 mg/cm^2 load) with commercial 20% Pd/C (0.028 mg/cm^2 load), and the thin film of the blend on Pt electrode shows a

FAO peak current of 0.66 mA (Figure 5.4a) whereas a peak current of 0.19 mA is seen from the bare Pt (Figure 5.4c). This synergistic effect and 3.5 times higher oxidation current compared to bare Pt (0.19 mA) also shows that the ternary composite of Pt-Pd/C and V(III)-POSS could be a promising FAO catalyst (Figure 5.4).

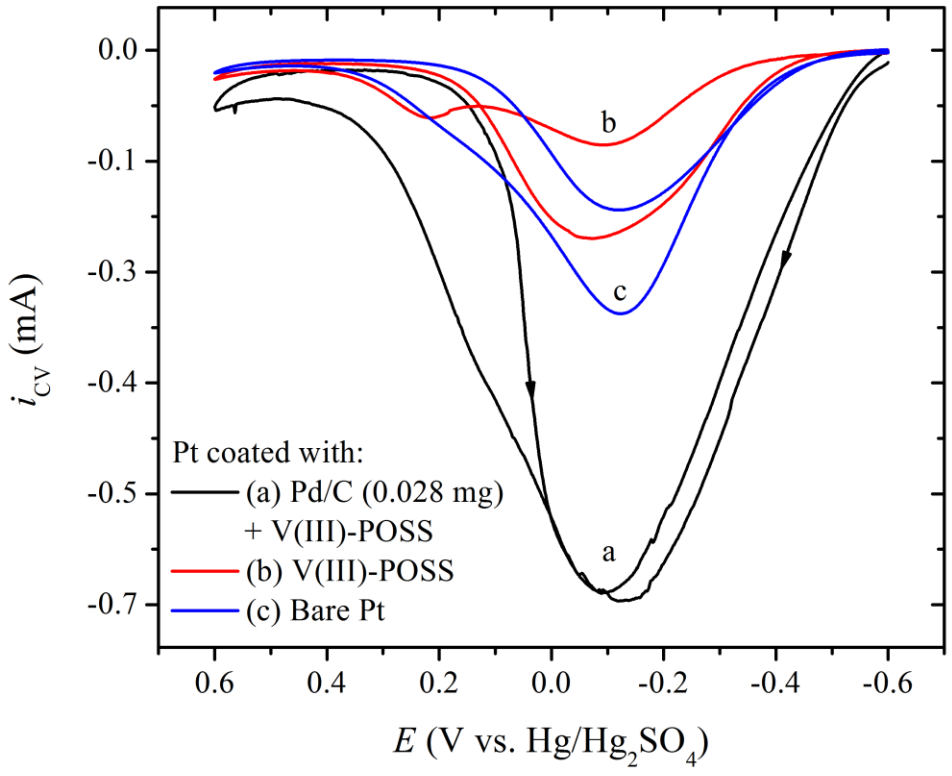

Figure 5.4 Effect of added V(III)-POSS into Pd/C at Pt WE on FAO.

Note: CV signals of 0.50 M HCOOH with 0.10 M H_2SO_4 using (a) a thin film of Pd/C mixed with V(III)-POSS on Pt, (b) V(III)-POSS coated Pt, and (c) bare Pt working electrode at a scan rate of 20.0 mV/s.

The effect of V(III)-POSS blended with Pd/C on FAO is further verified by utilizing different catalytic loads at GCE substrate as shown in Figure 5.5. With 0.0125 mg Pd loading the peak current is decreased to 0.22 mA (Figure 5.5c) as compared to

0.68 mA (Figure 5.5b) from the higher Pd load of 0.025 mg/cm^2 of GCE. Nevertheless, the peak current of 0.66 mA (Figure 5.5a) from the blend of V(III)-POSS and 0.0125 mg Pd load clearly proves the synergistic effect from the addition of the complex.

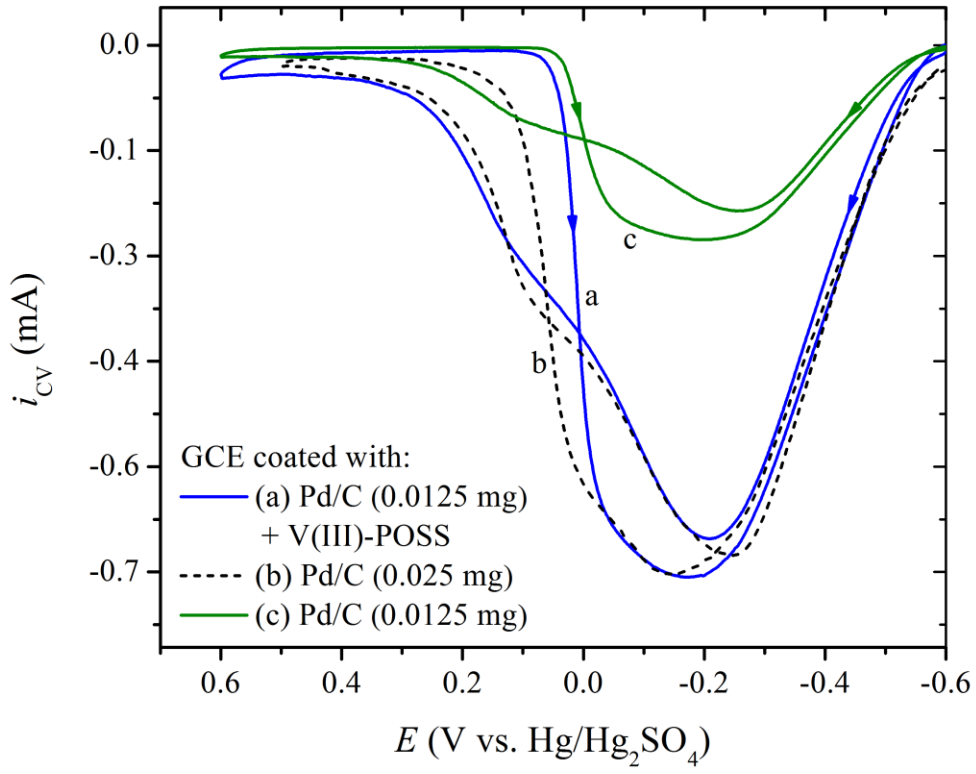

Figure 5.5 Effect of adding V(III)-POSS into Pd/C at GCE on FAO.

Note: CV signals of 0.50 M HCOOH with 0.10 M H_2SO_4 using GCE coated with (a) Pd/C (0.0125 mg Pd load) mixed with V(III)-POSS (0.0125 mg V(III)-POSS load), (b) Pd/C (0.025 mg Pd load), and (c) Pd/C (0.0125 mg Pd load) at a scan rate of 20.0 mV/s.

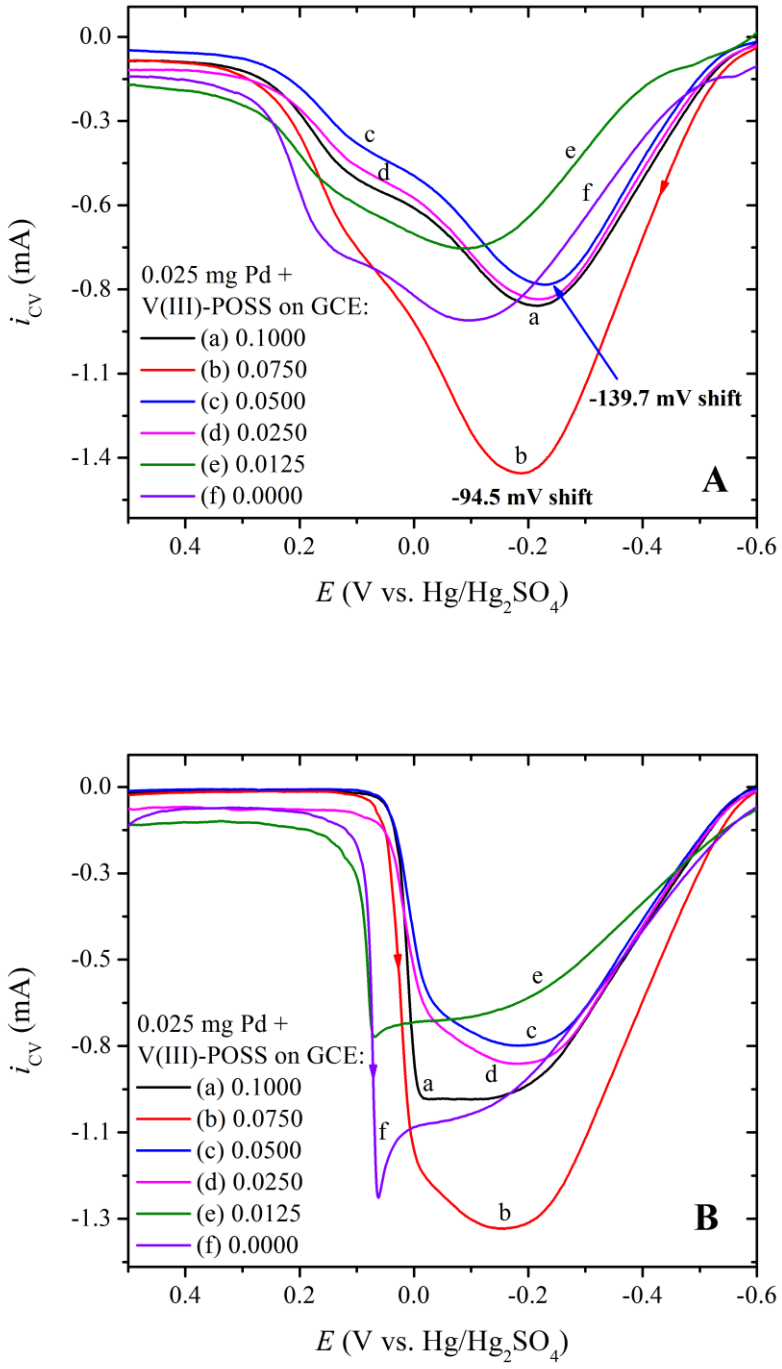

Figure 5.6 Effect of blending different loads of V(III)-POSS with a fixed amount of Pd/C at GCE substrate on FAO.

Note: (A) Forward and (B) reverse scans of the CV signals of 0.50 M HCOOH with 0.10 M H_2SO_4 using GCE coated with Pd/C (0.025 mg Pd load) blended with (a) 0.1000 mg to (f) 0.000 mg of V(III)-POSS at a scan rate of 20.0 mV/s.

The effect of blending different loads of V(III)-POSS with a fixed amount of Pd/C on FAO was also tested to optimize the use of the complex. As shown in Figure 5.6, two enhancement effects of addition of V(III)-POSS on FAO can be revealed. First, at a 3:1 V(III)-POSS vs. Pd mass ratio the peak current is the highest (1.5 mA) with a peak potential shift of -94.5 mV as compared with that at the Pd/C coated surface. Second, the use of a lower amount of V(III)-POSS lowers the peak current, but the peak potential is still shifted by -139.7 mV, suggesting a better catalytic activity (Figures 5.6c and d). Finally, the mass ratio of 0.5:1 V(III)-POSS to Pd exhibited a lower peak current than that of the 0:1 load. In this case, the peak position also shifted towards the positive direction.

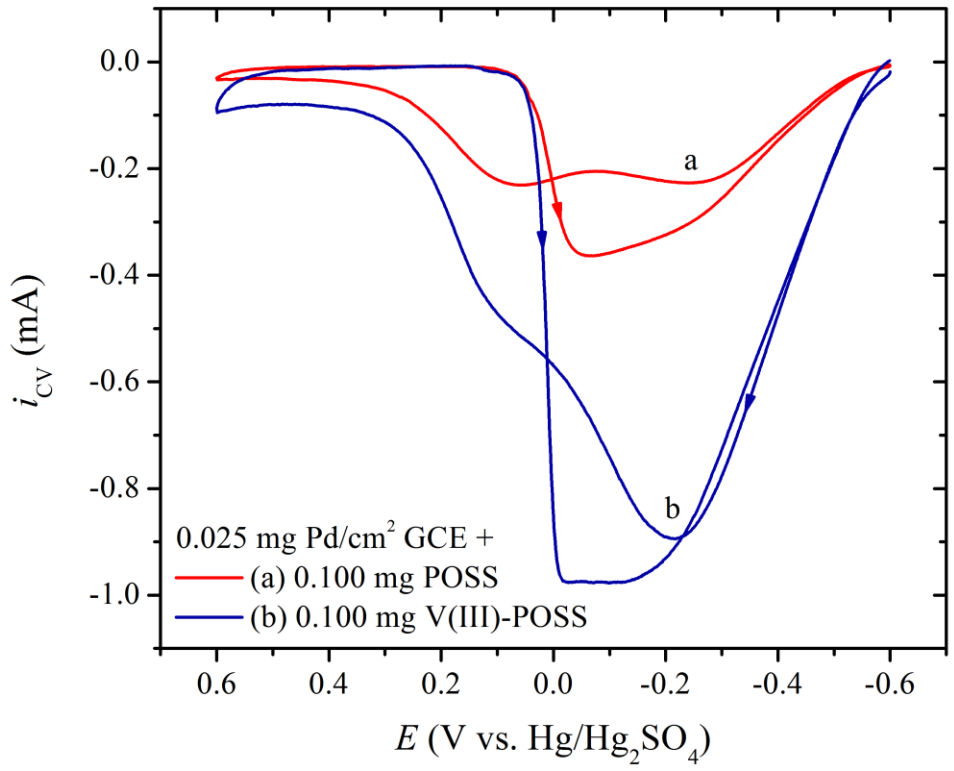

Figure 5.7 Impact of POSS vs. V(III)-POSS on Pd/C for FAO.

Note: CV signals of 0.50 M HCOOH with 0.10 M H_2SO_4 using GCE coated with Pd/C (0.025 mg Pd load) mixed with (a) 0.100 mg POSS vs. (b) 0.100 mg V(III)-POSS at a scan rate of 20.0 mV/s.

Additionally, the effect of POSS ligand on FAO is verified by using the same mass ratio of 4:1 POSS vs. Pd and V(III)-POSS vs. Pd (Figure 5.7). FAO current is found to be significantly decreased at the POSS-Pd/C (Figure 5.7a) with respect to that at the Pd/C (Figure 5.5 b) and V(III)-POSS mixed with Pd/C (Figure 5.7b). This observation could be attributed to the poor conductivity of POSS as well as possible blocking of the active catalyst surface of Pd/C by POSS.

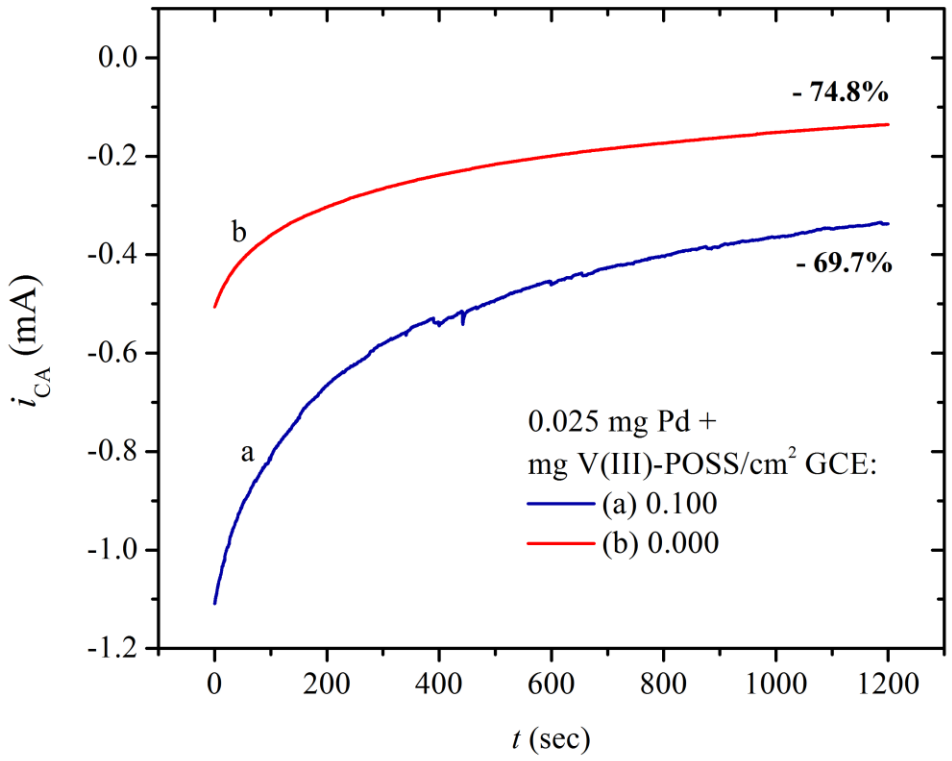

Figure 5.8 Chronoamperometry results of Pd/C vs. Pd/C and V(III)-POSS blend.

Note: CAs of (a) commercial 20 wt% Pd/C and V(III)-POSS mixture and (b) 20% Pd/C only at -0.2 V vs. MSE for 1200 sec.

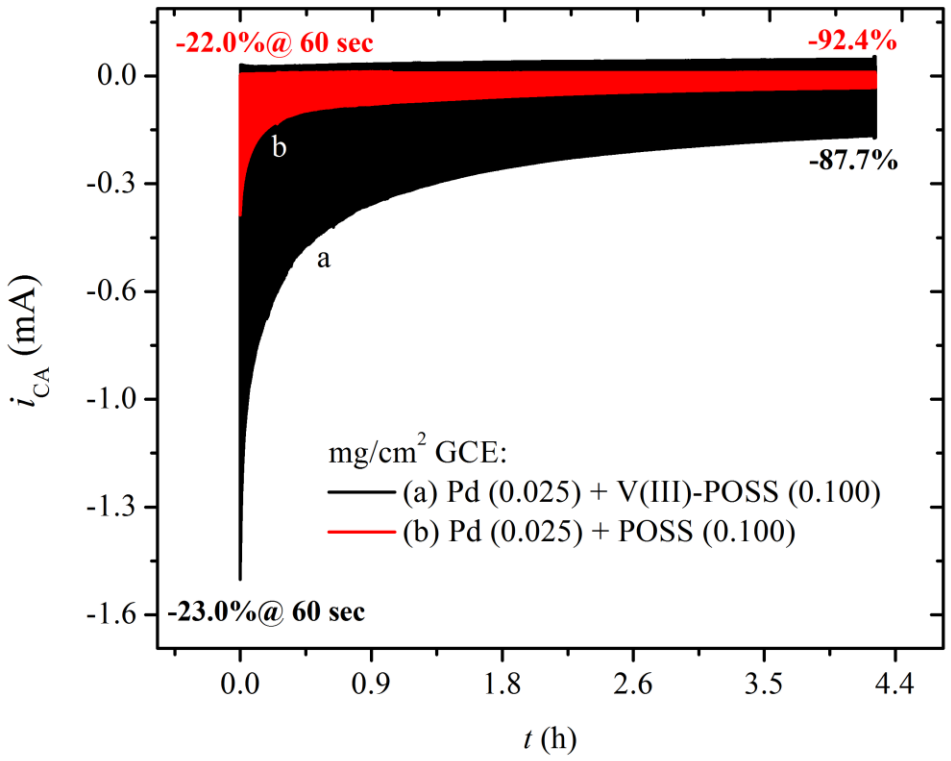

Figure 5.9 Multi-pulse CA responses.

Note: Pulse CAs of (a) commercial 20 wt% Pd/C and V(III)-POSS mixture and (b) 20% Pd/C and POSS mixture for ~4000 step cycles (4.27 h) between -0.10 to -0.60 V vs. Hg/Hg_2SO_4.

Table 5.1

Comparison of the % current decays using POSS and V(III)-POSS vs. Pd/C.

Catalysts	% current change (after 1200 sec) (CA)	% current change (after 4.27 h) (Pulse CA)
20% Pd/C	-74.8	-91.7
20% Pd/C + V(III)-POSS	-69.7	-87.7
20% Pd/C + POSS	-	-92.4

Note: From multi-potential CAs and CA results, % current changes were calculated using Equation 1.6.

Figures 5.8 and 5.9 display the stability test results of V(III)-POSS and Pd/C using CA and multi-pulse CA, respectively. Table 5.1 summarizes the overall data. The

initial current decays in Figure 5.8 exhibit the superior stability from the V(III)-POSS mixed with Pd/C. When the different blends are subjected to a long-term stability test using pulse-CA, V(III)-POSS mixed with Pd/C shows a high stability with a 87.7% current decay and a high amount of residual current (Figure 5.9a). On the other hand, addition of POSS to the Pd/C catalyst lowers the FAO current and decreases the stability of Pd/C catalyst (Figure 5.9b).

5.3.2 M-acac Complexes towards FAO

The initial trials led to additional experiments where the precursor to synthesize V(III)-POSS, namely vanadium acetylacetonate, $V(acac)_3$, was mixed with Pd/C followed by other M-acac complexes. In this section, a series of water insoluble M-acac complexes are studied towards FAO. The complexes were dispersed ultrasonically with Pd/C before immobilizing on GCE. The effect of $V(acac)_3$ with 20% Pd/C displays superior catalytic activity with a 136.0 mV peak potential shift towards the negative direction (Figure 5.10a). To verify further, the blend of V(III)-acac and Pd/C was compared with the same catalytic load of Pd/C only. Although the FAO peak current was slightly lower, which could be due to the diluted Pd on the surface. However, V(III)-acac coated GCE showed no FAO activity. On the reverse scan, the broader voltammogram from the combination also displayed direct FAO pathway.

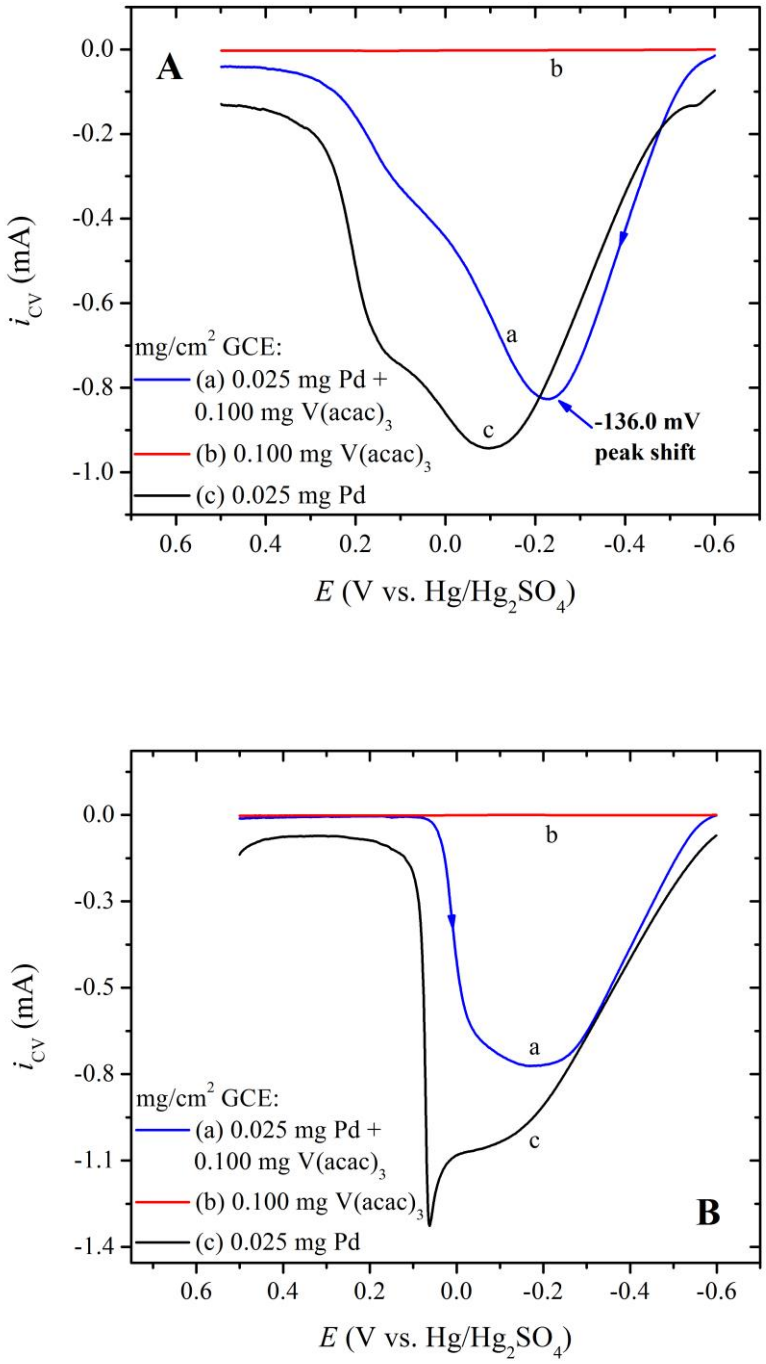

Figure 5.10 Effect of added $V(acac)_3$ into Pd/C on FAO at GCE.

Note: (A) Forward and (B) reverse scans of the CV signals of 0.50 M HCOOH with 0.10 M H_2SO_4 using GCE coated with (a) Pd/C (0.025 mg Pd load) mixed with V(III)-acac (0.100 mg), (b) V(III)-acac (0.100 mg), and (c) Pd/C (0.025 mg Pd load) at a scan rate of 20.0 mV/s.

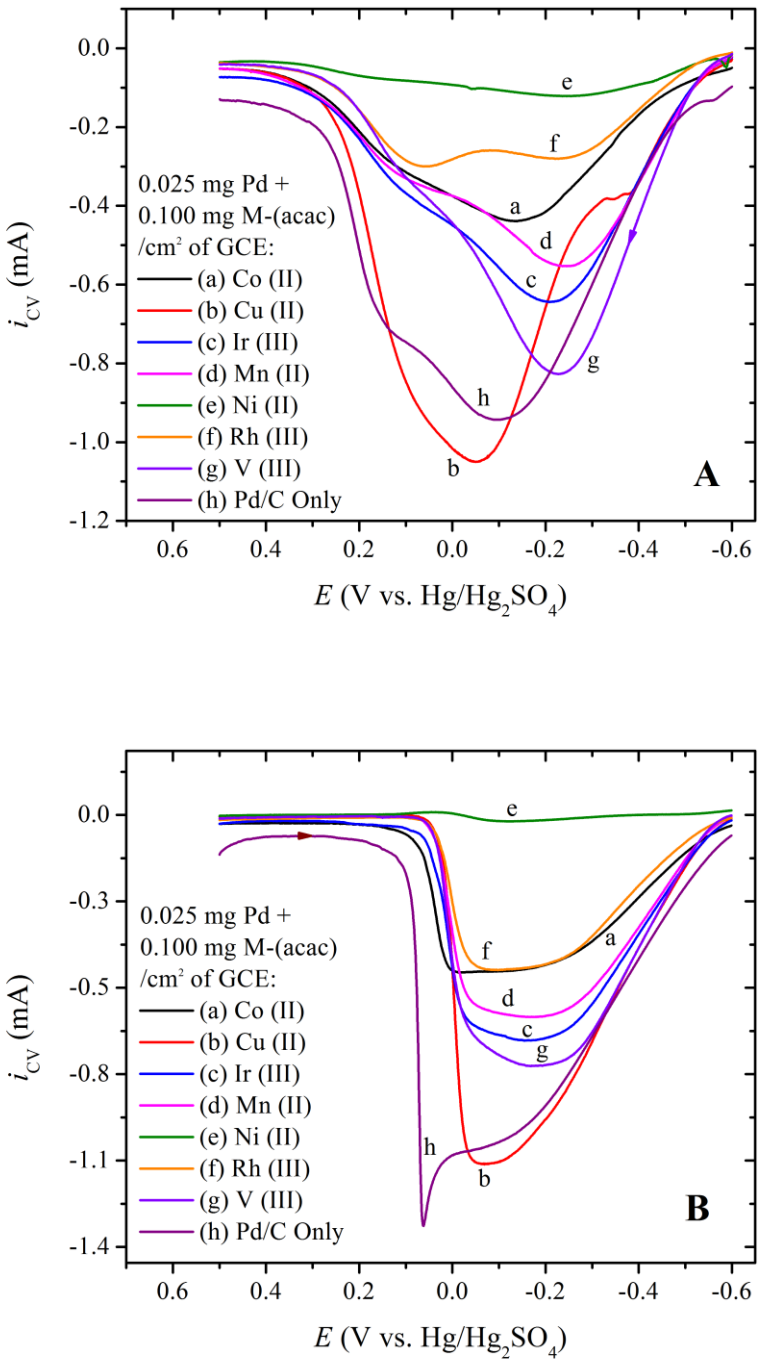

Figure 5.11 Blend of M-acac complexes with Pd/C towards FAO.

Note: (A) Forward and (B) reverse scans of the CV signals of 0.50 M HCOOH with 0.10 M H_2SO_4 using GCE coated with (a) – (g) Pd/C (0.025 mg Pd load) mixed with M-acac complexes (0.100 mg) individually, (h) Pd/C (0.025 mg Pd load) only at a scan rate of 20.0 mV/s.

As V(III)-acac showed promising synergistic effect when blended with Pd/C without the use of impregnation, or heating at high temperatures, other commercially available M-acac complexes were also studied (where, M = Co(II), Cu(II), Ir(III), Mn(II), Ni(II), Rh(III), V(III)). These metals were selected based on their availability and literature reports of enhanced FAO activity when mixed with Pt or Pd as described in Chapter I. Although these complexes are insoluble in aqueous media, they can form aqua-complexes in the presence of water. From the CV responses shown in Figure 5.11, it is evident that addition of the second component can enhance the FAO activity. Table 5.2 summarizes the peak currents and the peak potential shifts, and the latter is directly associated with the FAO pathways. It should also be mentioned that on the reverse scan (Figure 5.11B), all the M-acac blends showed a broader FAO current corresponding to the direct pathway. Additionally, like V(III)-acac (Figure 5.10b), other M-acac complexes themselves did not show any catalytic activity towards FAO.

From Tables 5.2 and 5.3, it can be depicted that the addition of Cu(II)-acac has a positive impact on FAO current (1.050 mA) with a high stability (86.8% current decay over 4.27 h) with respect to Pd/C alone (0.944 mA, 91.9% current decay). V(III)-, Mn(II)-complexes are the next best candidates followed by the Rh(III)- and Co(II)-mixtures. Surprisingly, Ni(II)-blend shows the lowest FAO current (0.122 mA) with the highest stability (75.8% current decay). This could be due to their different interactions with Pd and the synergistic effect.

Table 5.2

Summary of FAO activities of the M-acac and Pd/C blends vs. Pd/C.

Catalysts	Peak current, mA (Forward scan)	Peak potential, V vs. (Hg/Hg_2SO_4)	Potential shift vs. Pd/C, mV
20% Pd/C	-0.944	-0.0927	-
20% Pd/C + $Co(acac)_2$	-0.438	-0.1383	-45.6
20% Pd/C + $Cu(acac)_2$	-1.050	-0.0520	+40.7
20% Pd/C + $Ir(acac)_3$	-0.644	-0.2107	-118.0
20% Pd/C + $Mn(acac)_2$	-0.553	-0.2457	-153.0
20% Pd/C + $Ni(acac)_2$	-0.122	-0.2569	-164.2
20% Pd/C + $Rh(acac)_3$	-0.281	-0.2273	-134.6
20% Pd/C + $V(acac)_3$	-0.827	-0.2287	-136.0

Table 5.3

Durability of M-acac complex blends towards FAO vs. Pd/C.

Catalysts	% Current change (after 4.27 h)	Residual current, mA (after 1 h)
20% Pd/C	-91.9	0.084
20% Pd/C + $Co(acac)_2$	-89.9	0.141
20% Pd/C + $Cu(acac)_2$	-86.8	0.494
20% Pd/C + $Ir(acac)_3$	-84.6	0.256
20% Pd/C + $Mn(acac)_2$	-84.1	0.308
20% Pd/C + $Ni(acac)_2$	-75.8	0.192
20% Pd/C + $Rh(acac)_3$	-88.7	0.134
20% Pd/C + $V(acac)_3$	-90.9	0.207

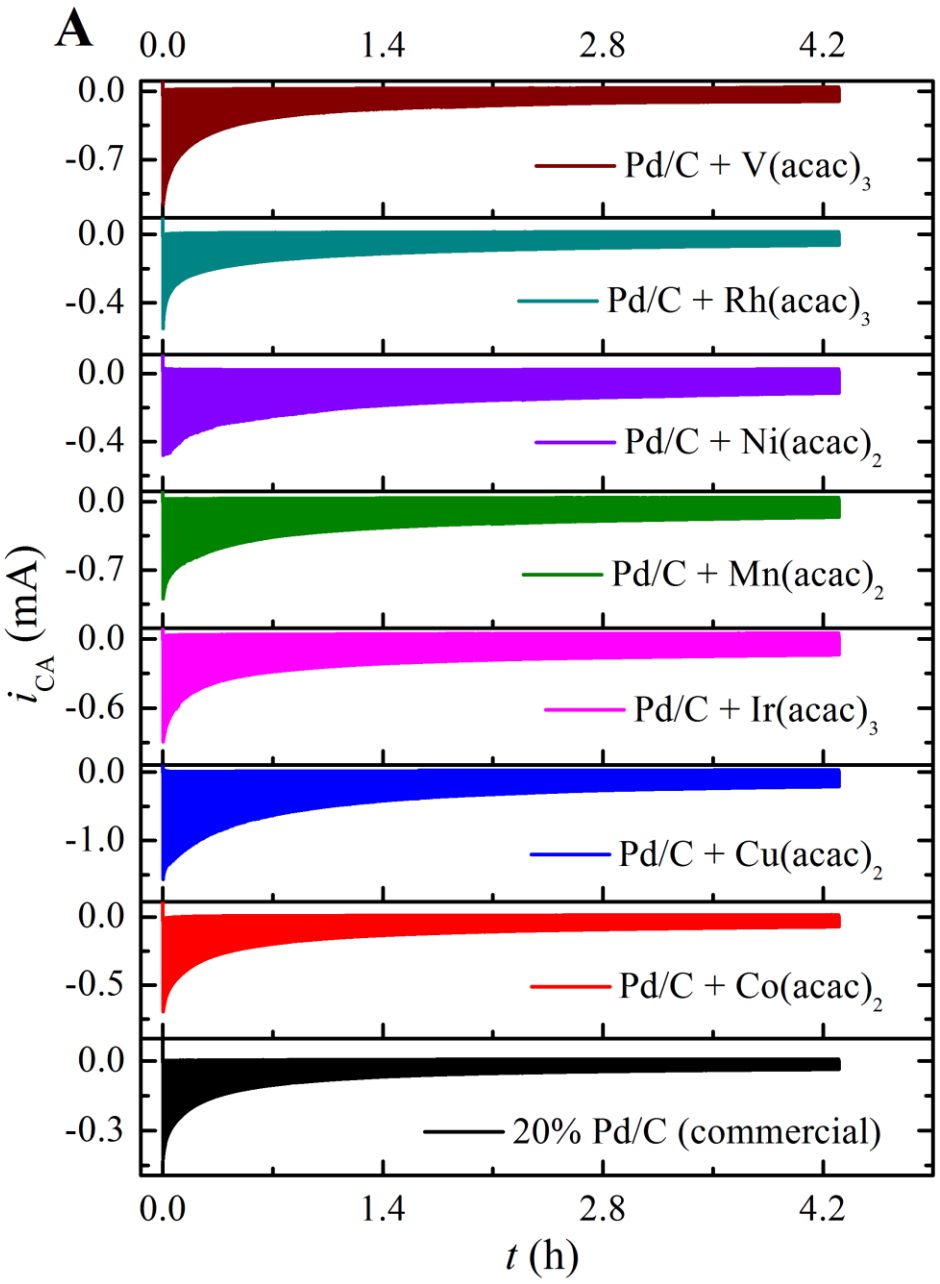
A
0.0
1.4
2.8
4.2
0.0
-0.7
Pd/C + V(acac)3
0.0
-0.4
Pd/C + Rh(acac)3
0.0
-0.4
Pd/C + Ni(acac)2
0.0
-0.7
Pd/C + Mn(acac)2
0.0
-0.6
Pd/C + Ir(acac)3
0.0
-1.0
Pd/C + Cu(acac)2
0.0
-0.5
Pd/C + Co(acac)2
0.0
-0.3
20% Pd/C (commercial)
0.0
1.4
2.8
4.2
t (h)
iCA (mA)

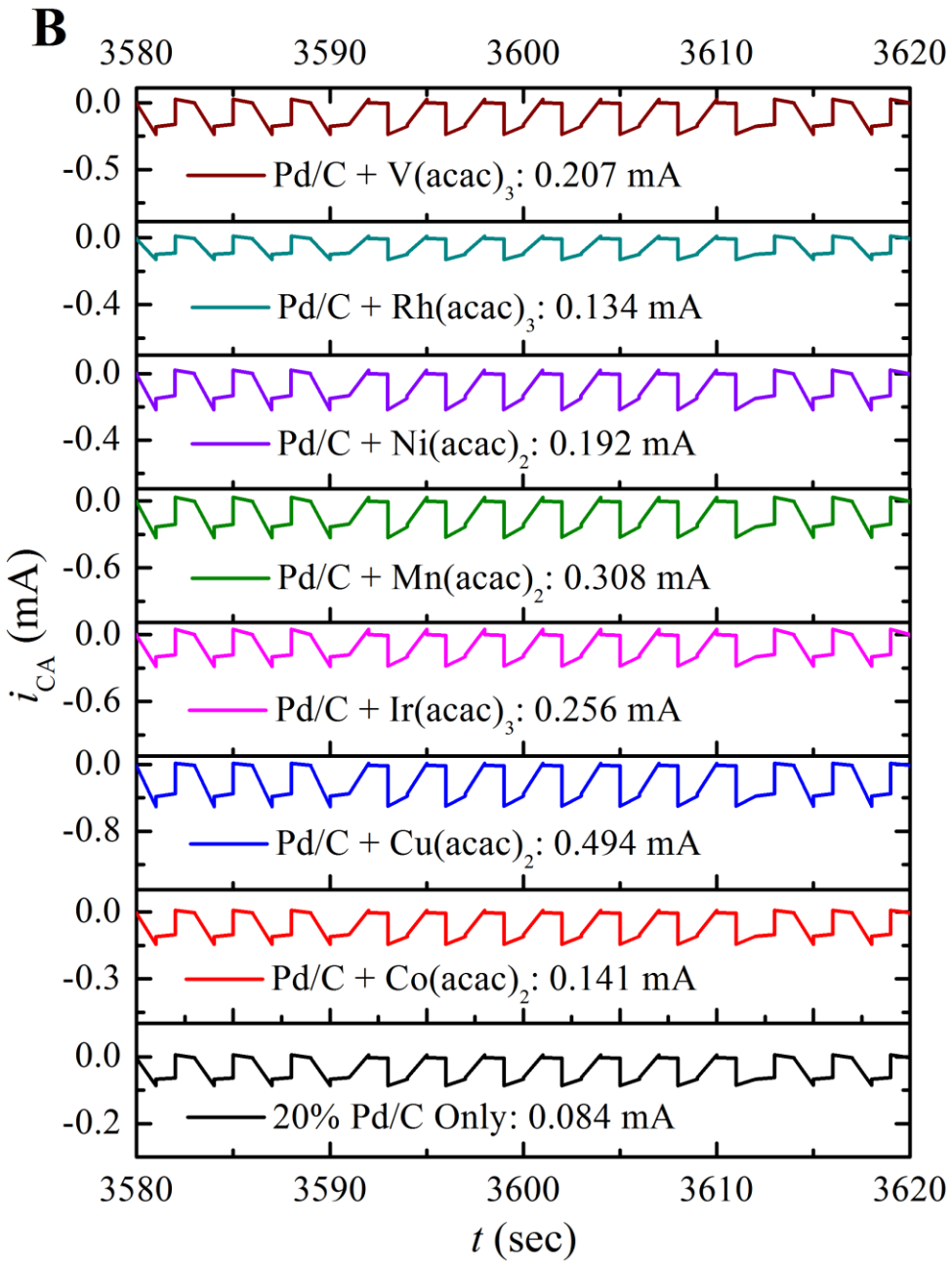

Figure 5.12 Multi-pulse chronoamperometry curves of 20% Pd/C and M-acac blends.

Note: Pulse CA signals of (A) fixed loads/cm^2 GCE of 20 wt% Pd/C (0.025 mg Pd) and M-acac complexes (0.100 mg) for ~4000 step cycles (4.27 h) between -0.10 and -0.60 V vs. MSE, (B) Close-up around 3600 sec.

5.3.3 Future Directions

5.3.3.1 Metal-complex Blends with Bi NRs

A few other blends and composite catalysts were tested towards FAO. As shown in Figures 5.13 and 5.14, when Bi NRs are added to the V(III)-acac and Pd/C blend, the FAO current is decreased with a peak shift of -70.3 mV relative to that of Pd/C is observed. Moreover, this ternary system is more stable with a 72.9% current decay after 4.27 h than both Pd/C (91.9%) and V(III)-acac with Pd/C (90.9%). The third-body effect of Bi NRs and the ensemble effect of V(III) could have played a role for the higher stability. However, the addition of two components to Pd/C lowers the effective Pd sites, hence lowers the FAO current. Different loadings of Bi NRs with the blends to prepare new composites could be beneficial to screen more effective FAO catalysts.

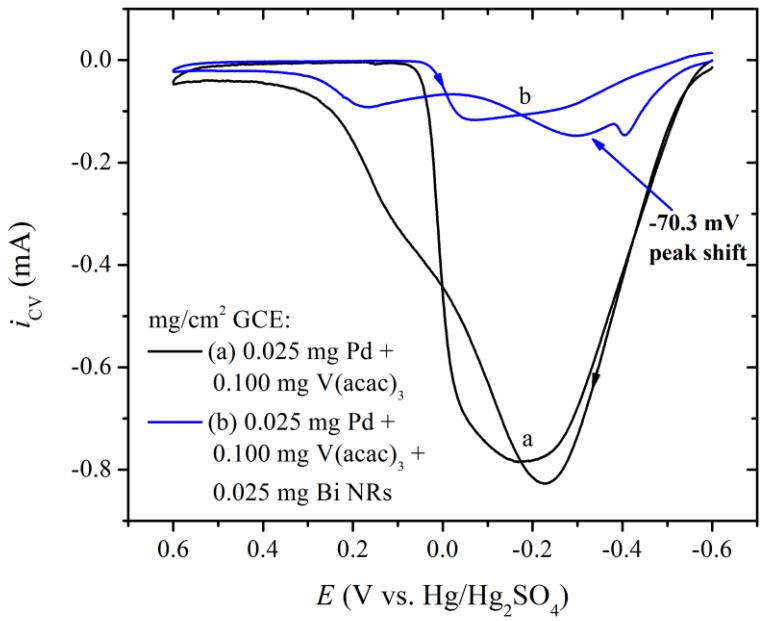

Figure 5.13 Effect of added Bi NRs to the V(acac)$_3$-Pd/C blend on FAO at GCE.

Note: CV signals of 0.50 M HCOOH with 0.10 M H_2SO_4 using GCE coated with (a) Pd/C (0.025 mg Pd load) mixed with V(III)-acac (0.100 mg), and (b) Pd/C (0.025 mg Pd load) and V(III)-acac (0.100 mg) mixed with 0.025 mg of Bi NRs at a scan rate of 20.0 mV/s.

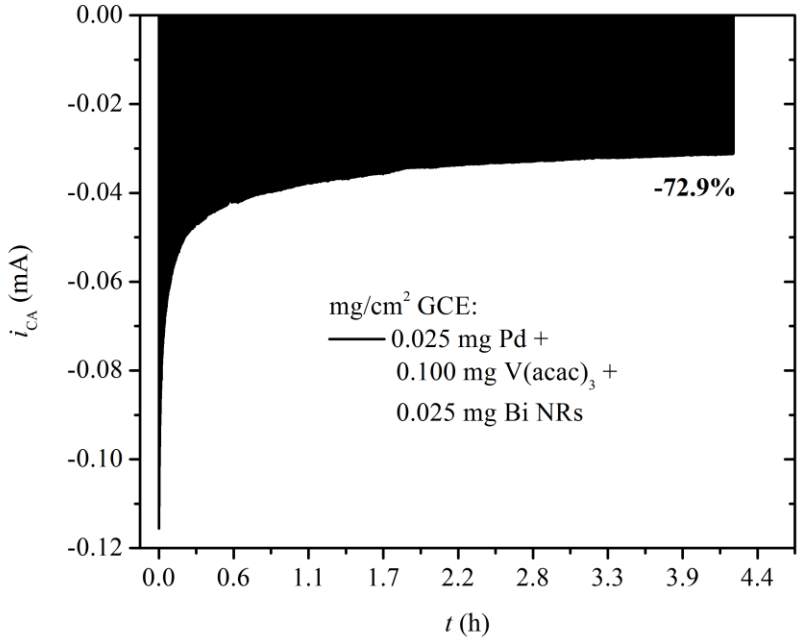

Figure 5.14 Multi-pulse CA response from the Bi NRs added blend.

Note: Pulse CA of Pd/C (0.025 mg Pd load) and V(III)-acac (0.100 mg) mixed with 0.025 mg of Bi NRs for ~4000 step cycles (4.27 h) between -0.10 and -0.60 V vs. Hg/Hg_2SO_4.

5.3.3.2 New Composites for FAO

Among few other ternary and binary composites, 10% PdSn/Vulcan XC-72 was characterized as displayed in Figures 5.15 – 5.17 and Table 5.4. The porous morphology, homogeneity, and small particle size (~10 nm) could be advantageous towards FAO. However, the material was not stable under the acidic condition, which could be due to the dissolution of the Sn particles. Mixing or adding other stable components could be approached to make this binary catalyst stable. Additionally, the CO tolerance of new blends could be studied.

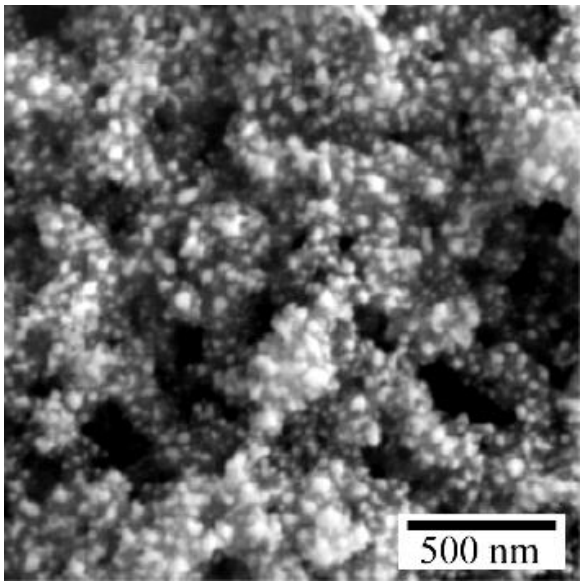

Figure 5.15 SEM image of 10% PdSn/Vulcan XC-72.

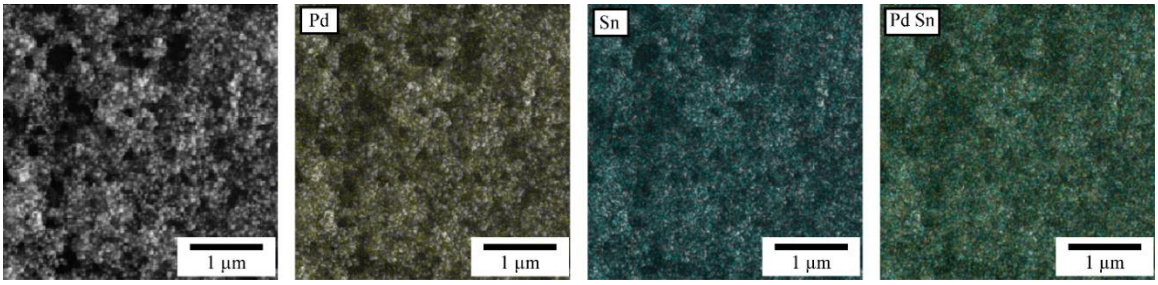

Figure 5.16 EDX mapping of 10% PdSn/Vulcan XC-72.

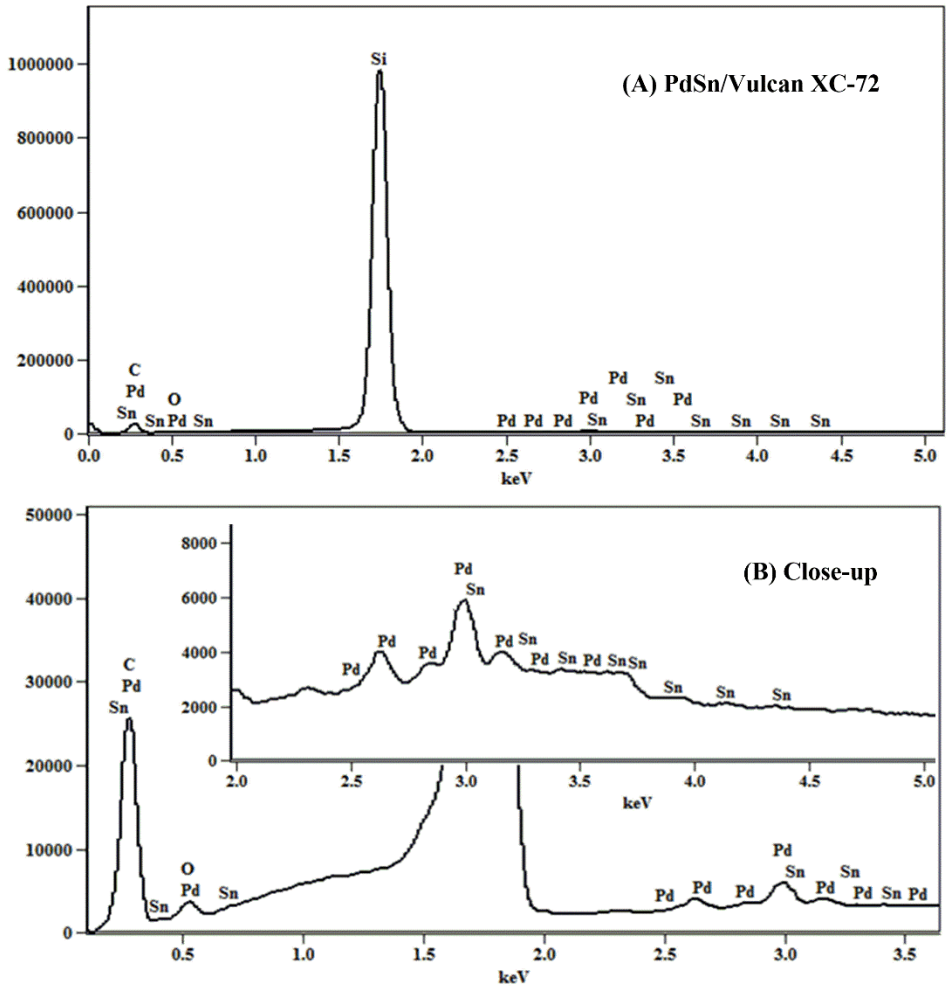

Figure 5.17 EDX spectra of 10% PdSn/Vulcan XC-72.

Table 5.4

Elemental composition of 10% PdSn/Vulcan XC-72.

Elements	Pd	Sn	C	Si	Ag	O
Weight%	0.29±0.03	7.09±0.05	17.07±0.13	73.03±0.23	1.42±0.02	1.10±0.03

5.4 Conclusion

In this chapter, several transition metal complexes were incorporated with the commercial 20% Pd/C catalyst and their activity and long-term durability towards FAO

were investigated. The synthesized Fe(III)-POSS alone had a very low catalytic activity when Pt electrode was used. Whereas, V(III)-POSS was a good candidate when mixed with Pd/C. Furthermore, the metal-acac complexes could be potential component to form hybrid catalysts. In terms of FAO current produced (from large to small), the blends can be ranked as: Cu(II) > Pd/C > V(III) > Ir(III) > Mn(II) > Co(II) > Rh(III) > Ni(II). Additionally, their FAO efficiencies in terms of the peak potential shift to the negative direction with respect to Pd/C are in the order of: Ni(II) > Mn(II) > V(III) > Rh(III) > Ir(III) > Co(II) > Cu(II). The catalytic stability of the hybrids after 4.27 h multi-pulse cycling can be ranked as: Ni(II) > Mn(II) ~ Ir(III) > Cu(II) > Rh(III) > Co(II) > V(III) > Pd/C. Consequently, the hybrid catalysts could be promising towards FAO. Finally, few more new approaches utilizing binary/ternary systems were suggested for future studies.

CHAPTER VI – SUMMARY AND PERSPECTIVES

To alleviate the ever-increasing energy crisis of 21st century, developing renewable fuels have become apparent. In this context, formic acid (HCOOH) has been considered a promising fuel to be used in direct formic acid fuel cells (DFAFCs) as a green fuel. Formic acid possesses several advantages over typical fuels (H_2, CH_3OH etc.) such as low toxicity, low crossover, good electrical conductivity, high output potential, and availability from biomass. However, the need for cost-effective, high performance, and durable anodic catalyst for the electrooxidation of HCOOH is still an unresolved issue. Considering the literature review and fundamentals of electroanalytical techniques discussed in Chapter I, this dissertation mainly focused on designing and analyzing a wide variety of new transition metal based nanocatalysts combining morphological and electrochemical characterization methods for formic acid oxidation (FAO).

Chapter II presented the investigation of the effect of leaked chloride ions on FAO at glassy carbon electrode (GCE) coated with 20 wt% Pd/C. Halide ions are known to be common contaminants that are believed to hinder the catalytic activity of polymer electrolyte membrane fuel cells (PEMFCs). The use of chloride ions containing reference electrodes such as Ag/AgCl (3.0 M KCl) and Hg/Hg_2Cl_2, is common in studies of HCOOH electrooxidation, but no systematic study has been reported about the effect of Cl^- ions on FAO catalysts. Thus, this study provides valuable insight about the impact of Cl^- ions on the inhibition of HCOOH electrooxidation behavior, which revealed that ~6.0 mM added chloride could deplete FAO current at GCE with 0.025 mg Pd load. It was also found that the immersion of Ag/AgCl electrode into the HCOOH electrolyte for ~6-8 min can result in complete loss of catalytic activity of Pd towards FAO. Based on the

study, non-chloride containing reference electrodes, e.g., mercury/mercury sulfate, Hg/Hg_2SO_4 (satd. K_2SO_4), and standard hydrogen electrode (SHE), are recommended to avoid the adverse effect of adsorbed chloride ions that poison the Pd/C catalyst even at a very low concentration.

Low metal loading, high surface area, good electrical conductivity, excellent stability in acidic and alkaline media, and easy availability make nanostructured carbon supports attractive for fuel cell applications. In Chapter III, the comparative studies of three different carbon-based support materials and their influence on catalytic activities towards FAO using mono (20 wt% Pd) and ternary (10 wt% PdNiCo) composite nano-catalysts with commercial 20 wt% Pd/C (activated carbon, ~500 m^2g^{-1}) were reported. The nano-catalysts were synthesized using Pd^{2+}, Ni^{2+} and Co^{2+} precursors using Vulcan-XC72 (250 m^2g^{-1}, <50 nm), Ketjen Black EC600 (1400 m^2g^{-1}), and graphite nano-particles (~10 nm) support materials with $NaBH_4$ as a reducing agent. The catalytic activity of all the catalysts for FAO was compared using cyclic voltammetry (CV). Multi-pulse chronoamperometry (CA) was utilized for stability tests, and carbon monoxide stripping-voltammetry (COSV) was employed to calculate the electrochemical active surface area (ECSA) and the anti-CO poisoning effects. The catalytic behavior of all the ternary nano-catalysts is believed to be ascribed to the direct FAO pathway as indicated by the oxidation peak potential of ~ -0.2 V vs. Hg/Hg_2SO_4 (satd. K_2SO_4). In contrast, the synthesized mono catalysts and commercial Pd/C showed both direct and indirect oxidation pathways. The use of NiCo combination with Pd showed synergistic effect as the FAO peak potential was shifted by ~-200 mV with respect to that of the commercial catalyst that contained double the amount of Pd. On the other hand, Vulcan-XC72

supported catalysts showed the highest FAO current and the rest were in close proximity to one another. Multi-pulse CA data showed that Ketjen Black supported catalysts were the most stable. Furthermore, COSV displayed the highest ESCA from the Vulcan XC-72 supported catalysts. Finally, morphology and elemental analyses employing electron microscopy techniques revealed that the different catalytic activity on various support materials were concordant with the electrochemical data as the nanocarbon substrates contributed to better metal dispersion and uniform size distribution.

Polyhedral oligomeric silsesquioxane (POSS) molecules are unique hybrid organic-inorganic ligands. Their high surface area, rigid cage structure, and low cost makes them potential candidates for developing new nano-hybrid catalysts for DFAFC. Chapter IV discussed the template assisted syntheses of Bi nanorods (Bi NRs) and Pd nanoparticles (Pd NPs) using OA-POSS and their catalytic activities for FAO. The synthesized Bi NRs showed third-body enhancement effect when dispersed with commercial 20 wt% Pd/C at a 1:1 mass ratio of Pd:Bi with a peak potential shift of ~-173 mV with respect to that of Pd/C. Due to small size of the Pd NPs, the catalytic activity for FAO and durability was high although the FAO peak current was low.

In Chapter V, a number of transition metal complexes (synthesized and commercial) were blended with the commercial 20 wt% Pd/C, and screened as electrocatlysts for FAO. First, trisilanol-POSS was used as a ligand to syntheses M-POSS complexes among which V(III)-POSS showed enhanced FAO activity due to synergistic effect on Pd/C. Additionally, several metal-acetylacetonate (M-acac) complexes were dispersed to screen new hybrid catalysts towards FAO. Based on CV and multi-pulse CA results, the blends were ranked. A few promising candidates would be Cu(II)-, V(III)-,

Ir(III)-, Mn(II)-acac complexes in terms of FAO current, activity, and long-term stability. Finally, new approaches using the metal-complexes and prepared composites could be utilized for future studies to develop new hybrids for FAO. In this regard, Bi NRs mixed with V(III)-acac and Pd/C was tested, which showed a low current decay of 72.9% over 4.27 h. Binary composite of 10 wt% PdSn/Vulcan XC-72 was also synthesized and characterized. Although this new catalyst was not stable towards FAO, efforts to make it stable could be studied as the material had uniform dispersion and small size distribution.

In summary, this dissertation provides valuable insights of the electro-catalytic characteristics of formic acid oxidation involving three broad classes of catalysts, namely, carbon supported Pd-based mono and ternary nanocatalysts, nanomaterials prepared utilizing POSS template, and metal-complexes blended with Pd/C. The electrooxidation activity of formic acid, which can be enhanced utilizing the abovementioned catalysts via bifunctional, third-body and electronic effects, was exploited. The fundamental question of the effect of chloride containing reference electrode on FAO, which could be crucial to scientific community involved in DFAFC research, was also answered. To conclude, these studies could lead to future studies to develop new compositions of nanomaterials, and their potential use towards DFAFCs.

REFERENCES

(1) Srinivasan, S. *Fuel Cells: From Fundamentals to Applications*; Springer Science+Business Media, LLC: New York, 2006.

(2) Costamagna, P.; Srinivasan, S. *J. Power Sources* **2001**, *102*, 242.

(3) US Department of Energy *(Washington, DC, U. S.)*, https://energy.gov.

(4) Yu, X.; Pickup, P. G. *J. Power Sources* **2008**, *182*, 124.

(5) Uhm, S.; Lee, H. J.; Lee, J. *Phys. Chem. Chem. Phys.* **2009**, *11*, 9326.

(6) Maiyalagan, T.; Nassr, A. B. A.; Alaje, T. O.; Bron, M.; Scott, K. *J. Power Sources* **2012**, *211*, 147.

(7) Baranova, E. A.; Miles, N.; Mercier, P. H. J.; Le Page, Y.; Patarachao, B. *Electrochim. Acta* **2010**, *55*, 8182.

(8) Weber, M.; Wang, J. T.; Wasmus, S.; Savinell, R. F. *J. Electrochem. Soc.* **1996**, *143*, L158.

(9) Rice, C.; Wieckowski, A. *Electrocatalysis in Fuel Cells*; Springer-Verlag: London, 2013.

(10) Bauskar, A. S.; Rice, C. A. *Electrochim. Acta* **2013**, *93*, 152.

(11) Yu, X.; Pickup, P. G. *Electrochim. Acta* **2011**, *56*, 4037.

(12) Yu, X.; Pickup, P. G. *Electrochem. Commun.* **2010**, *12*, 800.

(13) Parshall, G. W.; Ittel, S. D. *Homogeneous Catalysis: The Applications and Chemistry of Catalysis by Soluble Transition Metal Complexes*; Wiley: New York, 1992.

(14) Masters, C. *Homogeneous Transition-metal Catalysis: A Gentle Art*; Chapman and Hall, London: New York, 1981.

(15) Zeinalipour-Yazdi, C. D.; Cooksy, A. L.; Efstathiou, A. M. *Surf. Sci.* **2008**, *602*, 1858.

(16) Zhang, L.; Lu, T.; Bao, J.; Tang, Y.; Li, C. *Electrochem. Commun.* **2006**, *8*, 1625.

(17) Luo, Y.; Li, H.; Chen, T.; Ge, C.; Tang, Y.; Chen, Y.; Lu, T. *Electrochim. Acta* **2013**, *87*, 839.

(18) Huang, Y.; Zhou, X.; Liao, J.; Liu, C.; Lu, T.; Xing, W. *Electrochem. Commun.* **2008**, *10*, 621.

(19) Wang, Y.; Wu, B.; Gao, Y.; Tang, Y.; Lu, T.; Xing, W.; Liu, C. *J. Power Sources* **2009**, *192*, 372.

(20) Kwon, Y.; Baik, S. M.; Han, J.; Kim, J. *Bull. Korean Chem. Soc.* **2012**, *33*, 2539.

(21) Meng, H.; Xie, F. Y.; Chen, J.; Shen, P. K. *J. Mater. Chem.* **2011**, *21*, 11352.

(22) Zhou, Y.; Liu, J.; Ye, J.; Zou, Z.; Ye, J.; Gu, J.; Yu, T.; Yang, A. *Electrochim. Acta* **2010**, *55*, 5024.

(23) Bai, Z.; Yang, L.; Li, L.; Lv, J.; Wang, K.; Zhang, J. *J. Phys. Chem. C* **2009**, *113*, 10568.

(24) Wang, S.; Wang, X.; Jiang, S. P. *Nanotechnology* **2008**, *19*, 455602/1.

(25) Choi, J. H.; Noh, S. Y.; Han, S. D.; Yoon, S. K.; Lee, C. S.; Hwang, T. S.; Rhee, Y. W. *Korean J. Chem. Eng.* **2008**, *25*, 1026.

(26) Zhu, Y.; Khan, Z.; Masel, R. I. *J. Power Sources* **2005**, *139*, 15.

(27) Sáez, A.; Expósito, E.; Solla-Gullón, J.; Montiel, V.; Aldaz, A. *Electrochim. Acta* **2012**, *63*, 105.

(28) Kang, S.; Lee, J.; Lee, J. K.; Chung, S. Y.; Tak, Y. *J. Phys. Chem. B* **2006**, *110*, 7270.

(29) Kim, M. S.; Kim, D.; Lee, H. K.; Jeon, S. *J. Nanosci. Nanotechnol.* **2012**, *12*, 8861.

(30) Yu, X.; Pickup, P. G. *J. Power Sources* **2009**, *192*, 279.

(31) Kim, K. H.; Yu, J. K.; Lee, H. S.; Choi, J. H.; Noh, S. Y.; Yoon, S. K.; Lee, C. S.; Hwang, T. S.; Rhee, Y. W. *Korean J. Chem. Eng.* **2007**, *24*, 518.

(32) Blair, S.; Lycke, D.; Iordache, C. A. *ECS Trans.* **2006**, *3*, 1325.

(33) Rice, C. *J. Power Sources* **2003**, *115*, 229.

(34) Lu, G. Q.; Crown, A.; Wieckowski, A. *J. Phys. Chem. B* **1999**, *103*, 9700.

(35) Waszczuk, P.; Barnard, T. M.; Rice, C.; Masel, R. I.; Wieckowski, A. *Electrochem. Commun.* **2002**, *4*, 732.

(36) Kang, Y.; Qi, L.; Li, M.; Diaz, R. E.; Su, D.; Adzic, R. R.; Stach, E.; Li, J.; Murray, C. B. *ACS Nano* **2012**, *6*, 2818.

(37) Yu, X.; Pickup, P. G. *J. Power Sources* **2011**, *196*, 7951.

(38) Uhm, S.; Chung, S. T.; Lee, J. *Electrochem. Commun.* **2007**, *9*, 2027.

(39) Zhang, Z.; Wang, Y.; Wang, X. *Nanoscale* **2011**, *3*, 1663.

(40) Venkateswara Rao, C.; Cabrera, C. R.; Ishikawa, Y. *J. Phys. Chem. C* **2011**, *115*, 21963.

(41) Xu, J. B.; Zhao, T. S.; Liang, Z. X. *J. Power Sources* **2008**, *185*, 857.

(42) Yu, X.; Pickup, P. G. *J. Appl. Electrochem.* **2010**, *40*, 799.

(43) Jiang, J.; Kucernak, A. *J. Electroanal. Chem.* **2009**, *630*, 10.

(44) Shen, L.; Li, H.; Lu, L.; Luo, Y.; Tang, Y.; Chen, Y.; Lu, T. *Electrochim. Acta* **2013**, *89*, 497.

(45) Du, C.; Chen, M.; Wang, W.; Yin, G. *ACS Appl. Mater. Interfaces* **2011**, *3*, 105.

(46) Ohkubo, Y.; Shibata, M.; Kageyama, S.; Seino, S.; Nakagawa, T.; Kugai, J.; Nitani, H.; Yamamoto, T. A. *J. Mater. Sci.* **2012**, *48*, 2142.

(47) Malolepszy, A.; Mazurkiewicz, M.; Mikolajczuk, A.; Stobinski, L.; Borodzinski, A.; Mierzwa, B.; Lesiak, B.; Zemek, J.; Jiricek, P. *Phys. Status Solidi C* **2011**, *8*, 3195.

(48) Li, L.; E, Y.; Yuan, J.; Luo, X.; Yang, Y.; Fan, L. *Electrochim. Acta* **2011**, *56*, 6237.

(49) Lesiak, B.; Stobinski, L.; Kövér, L.; Tóth, J.; Kurzydłowski, K. J. *Phys. Status Solidi A* **2011**, *208*, 1791.

(50) Chiou, Y.-J.; Chen, K.-Y.; Lin, H.-M.; Liou, W.-J.; Liou, H.-W.; Wu, S.-H.; Mikolajczuk, A.; Mazurkiewicz, M.; Malolepszy, A.; Stobinski, L.; Borodzinski, A.; Kedzierzawski, P.; Kurzydlowski, K.; Chien, S.-H.; Chen, W.-C. *Phys. Status Solidi A* **2011**, *208*, 1778.

(51) Mikolajczuk, A.; Borodzinski, A.; Stobinski, L.; Kedzierzawski, P.; Lesiak, B.; Kövér, L.; Tóth, J.; Lin, H.-M. *Phys. Status Solidi B* **2010**, *247*, 2717.

(52) Hu, C.; Guo, Y.; Wang, J.; Yang, L.; Yang, Z.; Bai, Z.; Zhang, J.; Wang, K.; Jiang, K. *ACS Appl. Mater. Interfaces* **2012**.

(53) Zhu, F.; Ma, G.; Bai, Z.; Hang, R.; Tang, B.; Zhang, Z.; Wang, X. *J. Power Sources* **2013**, *242*, 610.

(54) Morales-Acosta, D.; Morales-Acosta, M. D.; Godinez, L. A.; Álvarez-Contreras, L.; Duron-Torres, S. M.; Ledesma-García, J.; Arriaga, L. G. *J. Power Sources* **2011**, *196*, 9270.

(55) Wang, R.; Liao, S.; Ji, S. *J. Power Sources* **2008**, *180*, 205.

(56) DandanTu; Wu, B.; Wang, B.; Deng, C.; Gao, Y. *Appl. Catal., B* **2011**, *103*, 163.

(57) Wang, X.; Tang, Y.; Gao, Y.; Lu, T. *J. Power Sources* **2008**, *175*, 784.

(58) Feng, L.; Yang, J.; Hu, Y.; Zhu, J.; Liu, C.; Xing, W. *Int. J. Hydrogen Energy* **2012**, *37*, 4812.

(59) Xu, C.; Liu, Y.; Wang, J.; Geng, H.; Qiu, H. *J. Power Sources* **2012**, *199*, 124.

(60) Qin, Y.-H.; Jiang, Y.; Niu, D.-F.; Zhang, X.-S.; Zhou, X.-G.; Niu, L.; Yuan, W.-K. *J. Power Sources* **2012**, *215*, 130.

(61) Obradović, M. D.; Rogan, J. R.; Babić, B. M.; Tripković, A. V.; Gautam, A. R. S.; Radmilović, V. R.; Gojković, S. L. *J. Power Sources* **2012**, *197*, 72.

(62) Hu, S.; Scudiero, L.; Ha, S. *Electrochim. Acta* **2012**, *83*, 354.

(63) Kitchin, J. R.; Norskov, J. K.; Barteau, M. A.; Chen, J. G. *J. Chem. Phys.* **2004**, *120*, 10240.

(64) Yang, G.; Chen, Y.; Zhou, Y.; Tang, Y.; Lu, T. *Electrochem. Commun.* **2010**, *12*, 492.

(65) Zhang, L.; Tang, Y.; Bao, J.; Lu, T.; Li, C. *J. Power Sources* **2006**, *162*, 177.

(66) Lu, L.; Li, H.; Hong, Y.; Luo, Y.; Tang, Y.; Lu, T. *J. Power Sources* **2012**, *210*, 154.

(67) Solla-Gullón, J.; Montiel, V.; Aldaz, A.; Clavilier, J. *Electrochem. Commun.* **2002**, *4*, 716.

(68) Hartley, F. R. *Chemistry of Platinum Group Metals: Recent Developments*; Elsevier, Amsterdam: New York, 1991.

(69) Mamuru, S. A.; Ozoemena, K. I.; Fukuda, T.; Kobayashi, N. *J. Mater. Chem.* **2010**, *20*, 10705.

(70) Bai, Z.; Guo, Y.; Yang, L.; Li, L.; Li, W.; Xu, P.; Hu, C.; Wang, K. *J. Power Sources* **2011**, *196*, 6232.

(71) An, H.; Cui, H.; Zhou, D.; Tao, D.; Li, B.; Zhai, J.; Li, Q. *Electrochim. Acta* **2013**, *92*, 176.

(72) Huang, H.; Wang, X. *Phys. Chem. Chem. Phys.* **2013**, *15*, 10367.

(73) Hunag, H.; Wang, X. *J. Mater. Chem.* **2012**, *22*, 22533.

(74) Huang, S. Y.; Ganesan, P.; Park, S.; Popov, B. N. *J. Am. Chem. Soc* **2009**, *131*, 13898.

(75) Wang, X.-M.; Wang, J.; Zou, Q.-Q.; Xia, Y.-Y. *Electrochim. Acta* **2011**, *56*, 1646.

(76) Wang, X.-M.; Xia, Y.-Y. *Electrochim. Acta* **2010**, *55*, 851.

(77) Lu, H.; Fan, Y.; Huang, P.; Xu, D. *J. Power Sources* **2012**, *215*, 48.

(78) Chu, Y.-Y.; Wang, Z.-B.; Jiang, Z.-Z.; Gu, D.-M.; Yin, G.-P. *Adv. Mater. (Weinheim, Ger.)* **2011**, *23*, 3100.

(79) Lim, J.; Malati, P.; Bonet, F.; Dunn, B. *J. Electrochem. Soc* **2007**, *154*, A140.

(80) Qu, W. L.; Wang, Z. B.; Sui, X. L.; Gu, D. M.; Yin, G. P. *Fuel Cells (Weinheim, Ger.)* **2013**, *13*, 149.

(81) Qu, W.-L.; Wang, Z.-B.; Jiang, Z.-Z.; Gu, D.-M.; Yin, G.-P. *RSC Adv* **2012**, *2*, 344.

(82) Zhang, Z.; Huang, Y.; Ge, J.; Liu, C.; Lu, T.; Xing, W. *Electrochem. Commun.* **2008**, *10*, 1113.

(83) Feng, L. G.; Yan, L.; Cui, Z. M.; Liu, C. P.; Xing, W. *J. Power Sources* **2011**, *196*, 2469.

(84) Song, C.; Khanfar, M.; Pickup, P. G. *J. Appl. Electrochem.* **2005**, *36*, 339.

(85) Köhler, C.; Kloke, A.; Drzyzga, A.; Zengerle, R.; Kerzenmacher, S. *J. Power Sources* **2013**, *242*, 255.

(86) Cheng, T. T.; Gyenge, E. L. *J. Appl. Electrochem.* **2009**, *39*, 1925.

(87) Cheng, T. T.; Gyenge, E. d. L. *J. Electrochem. Soc.* **2008**, *155*, B819.

(88) Ge, J.; Chen, X.; Liu, C.; Lu, T.; Liao, J.; Liang, L.; Xing, W. *Electrochim. Acta* **2010**, *55*, 9132.

(89) Hybrid Plastics Inc. *(Hattiesburg, MS, U.S.)* http://www.hybridplastics.com.

(90) Murugavel, R.; Voigt, A.; Walawalker, M. G.; Roesky, H. W. *Chem. Rev.* **1996**, *96*, 2205.

(91) Lorenz, V.; Fischer, A.; Giebmann, S.; Gilji, J. W.; Gun'ko, Y.; Jacob, K.; Edelmann, F. T. *Coord. Chem. Rev.* **2000**, *206-207*, 321.

(92) Marciniec, B.; Marciejewski, H. *Coord. Chem. Rev.* **2001**, *223*.

(93) Herrmann, W. A.; Anwander, R.; Dufaud, V.; Scherer, W. *Angew. Chem., Int. Ed. Engl.* **1994**, *33*, 1285.

(94) Feher, F. J.; Budzichowski, T. A. *Polyhedron* **1995**, *14*, 3239.

(95) Lichtenhan, J. D. *Inorg. Chem. Commun.* **1995**, *17*, 115.

(96) Edelmann, F. T.; Giebmann, S.; Fischer, A. *Inorg. Chem. Commun.* **2000**, *3*, 658.

(97) Hay, M. T.; Hainaut, B. J.; Geib, S. J. *Inorg. Chem. Commun.* **2003**, *6*, 431.

(98) Lorenz, V.; Fischer, A.; Edelmann, F. T. *Inorg. Chem. Commun.* **2000**, *3*, 292.

(99) Lorenz, V.; Fischer, A.; Jacob, K.; Edelmann, F. T. *Inorg. Chem. Commun.* **2003**, *6*, 795.

(100) Smet, P.; Riondato, J.; Pauwels, T.; Moens, L.; Verdonck, L. *Inorg. Chem. Commun.* **2000**, *3*, 557.

(101) Edelmann, F. T.; Giessmann, S.; Fischer, A. *J. Organomet. Chem.* **2001**, *620*, 80.

(102) Lorenz, V.; Fischer, A.; Edelmann, F. T. *J. Organomet. Chem.* **2002**, *647*, 245.

(103) Lorenz, V.; Spodia, M.; Fischer, A.; Edelmann, F. T. *J. Organomet. Chem.* **2001**, *625*, 1.

(104) Mintcheva, N.; Tanabe, M.; Osakada, K.; Georgieva, I.; Mihailov, T.; Trendafilova, N. *J. Organomet. Chem.* **2010**, *695*, 1738.

(105) Tanabe, M.; Mutou, K.; Mintcheva, N.; Osakada, K. *J. Organomet. Chem.* **2011**, *696*, 1211.

(106) Muller, E.; Edelmann, F. T. *Main Group Met. Chem.* **1999**, *22*.

(107) Gun'ko, Y. K.; Nagy, L.; Brueser, W.; Lorenz, V.; Fischer, A.; Giessmann, S.; Edelmann, F. T.; Jacob, K.; Vertes, A. *Monatsh. Chem.* **1999**, *130*, 45.

(108) Mintcheva, N.; Tanabe, M.; Osakada, K. *Organometallics* **2006**, *25*, 3776.

(109) Moran, M.; Casado, C. M.; Cuadrado, I.; Losada, J. *Organometallics* **1993**, *12*, 4327.

(110) Tanabe, M.; Mutou, K.; Mintcheva, N.; Osakada, K. *Organometallics* **2008**, *27*, 519.

(111) Fei, Z.; Fischer, A.; Edelmann, F. T. *Silicon Chem.* **2003**, *2*, 73.

(112) Fei, Z.; Ibrom, K.; Edelmann, F. T. *Z. Anorg. Allg. Chem.* **2002**, *628*, 2109.

(113) Lorenz, V.; Fischer, A.; Edelmann, F. T. *Z. Anorg. Allg. Chem.* **2000**, *626*, 124.

(114) Nooney, R. I.; Thirunavukkarasu, D.; Chen, Y.; Josephs, R.; Ostafin, A. E. *Chem. Mater.* **2002**, *14*, 4721.

(115) Wang, X.; Li, W.; Chen, Z.; Waje, M.; Yan, Y. *J. Power Sources* **2006**, *158*, 154.

(116) DeArmit, C., Phantom Plastics™ , *(Cincinnati, OH, U.S.)*, http://www.phantomplastics.com.

(117) Feher, F. J.; Budzichowski, T. A. *J. Organomet. Chem.* **1989**, *379*, 33.

(118) Choi, J.; Lee, K. M.; Wycisk, R.; Pintauro, P. N.; Mather, P. T. *J. Electrochem. Soc.* **2010**, *157*, B914.

(119) Decker, B.; Hartmann-Thompson, C.; Carver, P. I.; Keinath, S. E.; Santurri, P. R. *Chem. Mater.* **2010**, *22*, 942.

(120) Armaroli, N.; Balzani, V. *Angew. Chem., Int. Ed.* **2007**, *46*, 52.

(121) Lewis, N. S.; Nocera, D. G. *Proc. Natl. Acad. Sci. U. S. A.* **2006**, *103*, 15729.

(122) Vesborg, P. C. K.; Jaramillo, T. F. *RSC Adv* **2012**, *2*, 7933.

(123) Bard, A. J.; Faulkner, L. R. *Electrochemical Methods: Fundamentals and Applications*; Second ed.; John Wiley & Sons, Inc., 2001.

(124) Bard, A. J.; Stratmann, M. *Encyclopedia of Electrochemistry: Instrumentation and Electroanalytical Chemistry*; WILEY-VCH Verlag GmbH & Co. KGaA: Weinheim, 2003; Vol. 3.

(125) Zoski, C. G. *Handbook of Electrochemistry*; Elsevier: Oxford, 2007.

(126) Li, R.; Wei, Z.; Huang, T.; Yu, A. *Electrochim. Acta* **2011**, *56*, 6860.

(127) Chatenet, M.; Soldo-Olivier, Y.; Chaînet, E.; Faure, R. *Electrochim. Acta* **2007**, *53*, 369.

(128) Binninger, T.; Fabbri, E.; Kotz, R.; Schmidt, T. J. *J. Electrochem. Soc.* **2013**, *161*, H121.

(129) Papageorgopoulos, D. C.; de Bruijn, F. A. *J. Electrochem. Soc.* **2002**, *149*, A140.

(130) Dinh, H. N.; Ren, X.; Garzon, F. H.; Piotr, Z.; Gottesfeld, S. *J. Electroanal. Chem.* **2000**, *491*, 222.

(131) Spendelow, J. S.; Lu, G. Q.; Kenis, P. J. A.; Wieckowski, A. *J. Electroanal. Chem.* **2004**, *568*, 215.

(132) Lee, M. J.; Kang, J. S.; Kang, Y. S.; Chung, D. Y.; Shin, H.; Ahn, C.-Y.; Park, S.; Kim, M.-J.; Kim, S.; Lee, K.-S.; Sung, Y.-E. *ACS Catal.* **2016**, *6*, 2398.

(133) Cuesta, A.; Couto, A.; Rincón, A.; Pérez, M. C.; López-Cudero, A.; Gutiérrez, C. *J. Electroanal. Chem.* **2006**, *586*, 184.

(134) Vidaković, T.; Christov, M.; Sundmacher, K. *Electrochim. Acta* **2007**, *52*, 5606.

(135) Shao, M.; Odell, J. H.; Choi, S.-I.; Xia, Y. *Electrochem. Commun.* **2013**, *31*, 46.

(136) Vidaković, T.; Christov, M.; Sundmacher, K. *J. Appl. Electrochem.* **2008**, *39*, 213.

(137) Ochal, P.; Gomez de la Fuente, J. L.; Tsypkin, M.; Seland, F.; Sunde, S.; Muthuswamy, N.; Rønning, M.; Chen, D.; Garcia, S.; Alayoglu, S.; Eichhorn, B. *J. Electroanal. Chem.* **2011**, *655*, 140.

(138) Zheng, J.; Cullen, D. A.; Forest, R. V.; Wittkopf, J. A.; Zhuang, Z.; Sheng, W.; Chen, J. G.; Yan, Y. *ACS Catal.* **2015**, *5*, 1468.

(139) Mayrhofer, K. J. J.; Arenz, M.; Blizanac, B. B.; Stamenkovic, V.; Ross, P. N.; Markovic, N. M. *Electrochim. Acta* **2005**, *50*, 5144.

(140) Ali, S. T.; Li, Q.; Pan, C.; Jensen, J. O.; Nielsen, L. P.; Møller, P. *Int. J. Hydrogen Energy* **2011**, *36*, 1628.

(141) Jia, R.; Dong, S.; Hasegawa, T.; Ye, J.; Dauskardt, R. H. *Int. J. Hydrogen Energy* **2012**, *37*, 6790.

(142) Lam, A.; Li, H.; Zhang, S.; Wang, H.; Wilkinson, D. P.; Wessel, S.; Cheng, T. T. H. *J. Power Sources* **2012**, *205*, 235.

(143) Li, H.; Wang, H.; Qian, W.; Zhang, S.; Wessel, S.; Cheng, T. T. H.; Shen, J.; Wu, S. *J. Power Sources* **2011**, *196*, 6249.

(144) Li, H.; Zhang, S.; Qian, W.; Yu, Y.; Yuan, X.-Z.; Wang, H.; Jiang, M.; Wessel, S.; Cheng, T. T. H. *J. Power Sources* **2012**, *218*, 375.

(145) Pavlisic, A.; Jovanovic, P.; Selih, V. S.; Sala, M.; Hodnik, N.; Hocevar, S.; Gaberscek, M. *Chem Commun* **2014**, *50*, 3732.

(146) Seo, M.; Yun, Y.; Lee, J.; Tak, Y. *J. Power Sources* **2006**, *159*, 59.

(147) Strmcnik, D.; Gaberscek, M.; Hocevar, S.; Jamnik, J. *Solid State Ionics* **2005**, *176*, 1759.

(148) Yadav, A. P.; Nishikata, A.; Tsuru, T. *Electrochim. Acta* **2007**, *52*, 7444.

(149) Suo, Y.; Hsing, I. M. *Electrochim. Acta* **2009**, *55*, 210.

(150) Ali, H.; Kanodarwala, F. K.; Majeed, I.; Stride, J. A.; Nadeem, M. A. *ACS Appl. Mater. Interfaces* **2016**, *8*, 32581.

(151) Zhao, X.; Zhu, J.; Liang, L.; Liu, C.; Liao, J.; Xing, W. *J. Power Sources* **2012**, *210*, 392.

(152) Yu, X.; Pickup, P. G. *J. Appl. Electrochem.* **2011**, *41*, 589.

(153) Sharma, S.; Pollet, B. G. *J. Power Sources* **2012**, *208*, 96.

(154) Gao, W.; Keith, J. A.; Anton, J.; Jacob, T. *J. Am. Chem. Soc* **2010**, *132*, 18377.

(155) Leiva, E.; Iwasita, T.; Herrero, E.; Feliu, J. M. *Langmuir* **1997**, *13*, 6287.

(156) Peng, B.; Wang, H.-F.; Liu, Z.-P.; Cai, W.-B. *J. Phys. Chem. C* **2010**, *114*, 3102.

(157) Popovic, K.; Lovic, J. *J. Serb. Chem. Soc.* **2015**, *80*, 1217.

(158) Zhou, W.; Lee, J. Y. *J. Phys. Chem. C* **2008**, *112*, 3789.

(159) Qian, K.; Hao, F.; Wei, S.; Wang, Y.; Ge, C.; Chen, P.; Zhang, Y. *J. Solid State Electrochem.* **2016**, *21*, 297.

(160) Wang, X.; Naka, K.; Zhu, M.; Kuroda, H.; Itoh, H.; Chujo, Y. *J. Inorg. Organomet. Polym. Mater.* **2007**, *17*, 447.

(161) Yang, B.; Li, C.; Hu, H.; Yang, X.; Li, Q.; Qian, Y. *Eur. J. Inorg. Chem.* **2003**, *2003*, 3699.

(162) Li, Y.; Wang, J.; Deng, Z.; Wu, Y.; Sun, X.; Yu, D.; Yang, P. *J. Am. Chem. Soc* **2001**, *123*, 9904.

(163) Lu, X.; McKiernan, M.; Peng, Z.; Lee, E. P.; Yang, H.; Xia, Y. *Sci. Adv. Mater.* **2010**, *2*.

(164) Kijima, T. *Top Appl Phys* **2010**, *117*, 215.

(165) Alia, S. M.; Jensen, K. O.; Pivovar, B. S.; Yan, Y. *ACS Catal.* **2012**, *2*, 858.

(166) Liu, Y.; Yue, X.; Li, K.; Qiao, J.; Wilkinson, D. P.; Zhang, J. *Coord. Chem. Rev.* **2016**, *315*, 153.

(167) Gasteiger, H. A.; Kocha, S. S.; Sompalli, B.; Wagner, F. T. *Appl. Catal., B* **2005**, *56*, 9.

(168) Brouzgou, A.; Song, S. Q.; Tsiakaras, P. *Appl. Catal., B* **2012**, *127*, 371.

(169) Jasinski, R. *Nature* **1964**, *201*, 1212.

(170) Chu, D.; Jiang, R. *Solid State Ionics* **2002**, *148*, 591.

(171) Zeng, J.-Q.; Sun, S.-N.; Zhong, J.-P.; Li, X.-F.; Wang, R.-X.; Wu, L.-N.; Wang, L.; Fan, Y.-J. *Int. J. Hydrogen Energy* **2014**, *39*, 15928.

(172) Tosonian, S.; Ruiz, C. J.; Rios, A.; Frias, E.; Eichler, J. F. *J. Inorg. Chem.* **2013**, *3*, 7.

(173) Domínguez, C.; Pérez-Alonso, F. J.; Abdel Salam, M.; Gómez de la Fuente, J. L.; Al-Thabaiti, S. A.; Basahel, S. N.; Peña, M. A.; Fierro, J. L. G.; Rojas, S. *Int. J. Hydrogen Energy* **2014**, *39*, 5309.

(174) Xia, D.; Liu, S.; Wang, Z.; Chen, G.; Zhang, L.; Zhang, L.; Hui, S.; Zhang, J. *J. Power Sources* **2008**, *177*, 296.

(175) Wiesener, K.; Ohms, D.; Neumann, V.; Franke, R. *Mater. Chem. Phys.* **1989**, *22*, 457.

(176) Zagal, J.; Paez, M.; Tanaka, A. A.; Santos, J. R.; Linkous, C. A. *J. Electroanal. Chem.* **1992**, *339*, 13.

(177) Zhang, L.; Zhang, J.; Wilkinson, D. P.; Wang, H. *J. Power Sources* **2006**, *156*, 171.

(178) Chenitz, R. g.; Dodelet, J.-P. *J. Electrochem. Soc.* **2010**, *157*, B1658.

(179) Einaga, H.; Urahama, N.; Tou, A.; Teraoka, Y. *Catal. Lett.* **2014**, *144*, 1653.

(180) Liu, F.; John, K. D.; Scott, B. L.; Baker, R. T.; Ott, K. C.; Tumas, W. *Angew. Chem., Int. Ed.* **2000**, *39*, 3127.

(181) Feher, F. J.; Walzer, J. F. *Inorg. Chem.* **1991**, *30*, 1689.